

DISSERTATION

submitted to the
Combined Faculties for the Natural Sciences and for Mathematics
of the
Ruperto-Carola University of Heidelberg, Germany
for the degree of
Doctor of Natural Sciences

Put forward by
Dipl.-Phys. Bastian Höltkemeier
born in Bielefeld, Germany

Date of oral examination: October 27th, 2016

SYMPATHETIC COOLING OF IONS
IN A HYBRID ATOM ION TRAP

BASTIAN HÖLTKEMEIER

Referees: Prof. Dr. Matthias Weidemüller
Prof. Dr. Klaus Blaum

Abstract. In this thesis the dynamics of a trapped ion immersed in a spatially localized buffer gas is investigated. For a homogeneous buffer gas, the ion's energy distribution reaches a stable equilibrium only if the mass of the buffer gas atoms is below a critical value. This limitation can be overcome by using multipole traps in combination and/or a spatially confined buffer gas. Using a generalized model for elastic collisions of the ion with the buffer gas atoms, the ion's energy distribution is numerically determined for arbitrary buffer gas distributions and trap parameters. Three regimes characterized by the respective analytic form of the ion's equilibrium energy distribution are found. One of these is a novel regime at large atom-to-ion mass ratios where the final ion temperature can be tuned by adiabatically decreasing the spatial extension of the buffer gas and the effective ion trap depth (forced sympathetic cooling). The second part of the thesis presents a hybrid atom ion trap designed for sympathetic cooling of hydroxide anions. In this hybrid trap the anions are immersed in a cloud of laser cooled rubidium atoms. The translational and rovibrational temperatures of the anions are probed by photodetachment tomography and spectroscopy which shows the first ever indication of sympathetic cooling of anions by laser cooled atoms.

Zusammenfassung. In dieser Arbeit wird die Dynamik eines gefangenen Ions untersucht welches mit einem örtlich lokalisierten Puffergas interagiert. Für eine homogene Puffergasverteilung erreicht das Ion nur dann ein Equilibrium, wenn die Masse der Puffergasteilchen unter einem gewissen kritischen Wert liegt. Diese Limitation kann durch die Verwendung einer hochpoligen Falle und/oder einem örtlich lokalisierten Puffergas überwunden werden. Mit Hilfe eines generalisierten Modells für die Beschreibung elastischer Kollisionen zwischen den Ionen und dem Puffergas wurde die Energieverteilung der Ionen in Abhängigkeit von der Puffergasverteilung und den Fallenparametern numerisch berechnet. Drei Regime die durch unterschiedliche analytische Formen der Gleichgewichts-Energieverteilung der Ionen charakterisiert sind wurden gefunden. Eines dieser Regime ist ein neuartiges Regime bei großen Atom-Ionen Massenverhältnissen in dem die finale Temperatur der Ionen durch adiabatische Veränderung der Puffergasverteilung oder der Fallenparameter gesteuert werden kann (die sympathischste aller Kühlungen). Im zweiten Teil dieser Arbeit wird eine Hybrid-Atom-Ionen Falle vorgestellt, welche für die sympathische Kühlung von Hydroxid-Anionen konzipiert wurde. In dieser Falle wechselwirken die Anionen mit einer lasergekühlten Wolke aus Rubidium Atomen. Die Translations- als auch die Rotations-Vibrations-Temperatur der Anionen wird mittels Photolösungs-Tomographie und -Spektroskopie ermittelt, wodurch der erste Hinweis auf sympathische Kühlung von Anionen mittels lasergekühlter Atome erbracht werden konnte.

CONTENTS

1	INTRODUCTION	1
2	SYMPATHETIC COOLING INSIDE RADIO FREQUENCY TRAPS	7
2.1	An ion inside a linear radio frequency trap	8
2.1.1	Radial confinement	9
2.1.2	Mathieu equations	12
2.1.3	Adiabatic approximation	13
2.1.4	Constants of the ion motion	16
2.2	Ion-neutral collisions inside an rf trap	19
2.2.1	Collisional heating	20
2.2.2	Elastic collision inside an rf trap	22
2.2.3	The effective buffer gas picture	23
2.2.4	Collisional energy transfer	24
2.3	Ion's energy distribution	27
2.3.1	Numerical model	29
2.3.2	Equilibrium regimes	30
2.3.3	Boltzmann regime	32
2.3.4	Power-law regime	33
2.3.5	Localization regime	36
2.3.6	Forced sympathetic cooling	39
3	HYBRID ATOM ION TRAP	41
3.1	Trapping of anions	43
3.1.1	Ion source	43
3.1.2	Electrostatic lenses and benders	48
3.1.3	Time of flight separation	50
3.1.4	Radio-frequency trap	53
3.1.5	Ion detection	57
3.1.6	Optimization of the trapping efficiency	58
3.2	The atom trap	65
3.2.1	Principle of a magneto-optical trap	65
3.2.2	Laser system	66
3.2.3	Two-dimensional magneto-optical trap	68
3.2.4	Dark spontaneous force optical trap setup	72
3.2.5	Saturated absorption imaging	75
3.2.6	Optimization of the atom density	84
4	PHOTODETACHMENT OF OH ⁻	87
4.1	Molecular states	88
4.1.1	Hund's coupling cases	88
4.1.2	Nomenclature of electronic states	90
4.1.3	Ro-vibrational levels	90

4.1.4	Ro-vibrational spectrum of OH^- and OH	92
4.2	Photodetachment of OH^-	94
4.2.1	Possible transitions	94
4.2.2	Transition intensities	97
4.2.3	Threshold behavior	99
4.3	Photodetachment spectroscopy	101
4.3.1	Comparison with previous experimental data	103
4.3.2	Determination of the translational energy	105
4.4	Photodetachment in the HAITrap	106
4.4.1	Detachment laser	106
4.4.2	Photodetachment cross section	107
4.4.3	Photodetachment spectroscopy	108
4.4.4	Photodetachment tomography	109
4.5	Rubidium - OH^- collisions	111
4.5.1	Associative detachment of OH^-	111
4.5.2	Sympathetic cooling of OH^-	115
5	CONCLUSION	119
5.0.3	Outlook	121
	BIBLIOGRAPHY	123

INTRODUCTION

Cooling of atoms, ions and molecules close to absolute zero temperatures is a fascinating field of research. The possibility of studying different kinds of matter when all motional and internal degrees of freedom are completely frozen has triggered a large number of experiments ranging over many fields of research some as different as solid state physics and fluid dynamics. At room temperature ($T = 300\text{K}$) particles move at speeds of many hundreds or even thousands of meters per second and in molecules a large number of ro-vibrational states is populated.

For many applications this limits the accuracy as the particle motion leads to Doppler-broadening and thermal noise. Many experiments therefore require specially cooled samples, e.g. by using a cryostat. For a long time the coldest samples were realized by cooling with liquid nitrogen ($T \approx 70\text{K}$) or liquid helium ($T \approx 4\text{K}$). With special cryostats build from a mixture of ^3He and superfluid ^4He it is even possible to reach temperatures on the order of 100mK [1]. A rubidium atom cooled to this temperature has a thermal velocity of only $v \approx 4.5\text{m/s}$ compared to $v \approx 250\text{m/s}$ at room temperature which is already a large improvement.

For a long time this was the absolute temperature limit for thermal gases. Only with the invention of magneto-optical traps [2] could this cooling limit be overcome and temperatures many orders of magnitude below one kelvin could be realized. In a typical magneto-optical trap, rubidium can easily be cooled to $100\mu\text{K}$ which corresponds to a thermal velocity of $v \approx 0.1\text{m/s}$. Using sub-doppler cooling techniques [3] or by evaporatively cooling the atoms in a dipole trap [4], the atoms can be cooled even further. The coldest temperatures achieved in modern laser-cooling experiments are on the order of a few tens of nano-Kelvin. At this temperature the thermal velocity of rubidium $v \approx 3\text{mm/s}$ is even one order of magnitude smaller than a very slowly moving ant [5] ($v \approx 3\text{cm/s}$).

At these ultra-cold temperatures the properties of the particles exhibit a dramatic change as their wave-nature characterized by the de Broglie wavelength $\lambda = h/p$ prevails. For room temperature rubidium the de Broglie wavelength $\lambda = 2 \times 10^{-11}$ is only a fraction of the size of the atom whereby the atom is best seen as a particle. At ultra-cold temperatures however, the de Broglie wavelength can become as large as a few micrometers and the atom is best described as a matter wave.

Reaching this ultra-cold quantum regime has revolutionized many existing fields of physics and has created completely new fields of research. Atomic clocks built from laser cooled atoms have improved the time resolution to levels where even relativistic effects such as changes in gravitation or the relative velocity of the clock itself can be directly observed as changes in the clock frequency [6]. Laser cooled atoms [7] and ions [8, 9] have also been used for performing quantum simulations which might exceed the computational possibilities of classical computers in the future. This field of research has virtually exploded since Shor published his by now famous algorithm to factorize any non-prime number using a quantum computer [10]. If such a quantum computer would ever be built, most of the current encryption methods could be broken.

Reaching the ultra-cold regime has revolutionized quantum physics as concepts and ideas which were for a long time only Gedenkenexperiments can now be realized and measured in labs all over the world. The quantum-gas phase diagram could be extended by a few more (previously predicted) entries. As soon as the de Broglie wavelength reaches the same order of magnitude as the inter-particle spacing the particles exhibit strange new behaviors. In this regime bosonic particles all condense into the lowest quantum state where they form a Bose-Einstein condensate [11] whereas fermions can become superfluid [12]. These states of matter could even shine some light on the working principle of superconductors, as superfluid fermions can be described approximately as a Bardeen, Cooper and Schreifer (BCS) superconductor [13].

All these experiments on ultra-cold atoms, ions and molecules are pushing our understanding in many fields of physics to ever new limits. So far with every new kind of matter that has been cooled down to the ultra-cold regime a whole new class of novel experiments and applications could be realized. In order to move the field forward, the control over existing ultra-cold systems is steadily improved and there is a never ending search for new techniques that enable the realization of novel ultra-cold systems.

In this search, laser cooling is by far the most prominent tool for the preparation of ultra-cold samples. Up to date, a wide variety of different species have been laser cooled. The simplest candidates for laser cooling are alkali metals which, due to their simple electronic structure offer easily accessible closed cooling transitions and where therefore the first group of atoms to be used in laser-cooling experiments. But over the years a large number of more complicated laser cooling schemes has been developed which allow to also cool other groups of elements including alkaline earth metals such as Sr [14] or Ca [15], different lanthanides including Yb [16], Er [17], Tm [18], Dy [19] and Ho [20] and other species such as Cr [21]. Laser cooling has also been applied to ions stored in Penning traps [22] as well

as Paul traps [23] where the ions arrange in Coulomb crystals when sufficiently cooled.

Also cold molecules have triggered large interest. In 2009 a review article [24] already phrased the question "Why are Cold Molecules so Hot?", listing a large number of possible applications for ultra-cold molecules. Possible laser-cooling schemes for different molecules were first proposed about ten years ago [25, 26] and have now also been realized in different experiments using HD^+ [27], SrF [28, 29], YO [30] and CaF [31]. Since then, this new field is growing rapidly and it is to be expected that many more types of molecules will be cooled in the years to come.

However, direct laser cooling of molecules requires advanced cooling schemes, accounting for the complicated internal structure of the molecule. Due to the large number of electronic and ro-vibrational states, the cooling schemes typically involve a large number of different lasers, covering all the intermediate and meta-stable states. Every molecule therefore requires a unique optical pumping scheme [25].

Appropriate cooling schemes are not available for most atoms, ions and molecules which is why a large fraction of all particles cannot be directly laser-cooled. For this large group of particles indirect cooling schemes are required. One of these approaches is the creation of molecules from laser cooled atoms using photo-association [32, 33] or magnetic feshbach resonances [34, 35]. With these techniques the creation of molecules in the absolute ro-vibrational ground state has been realized.

Another widely used approach is to cool the particles sympathetically. For ions this has been realized by loading two different species into the same trap one of which is laser cooled [36]. This way, the motional degrees of freedom of the second species can be efficiently cooled. Unfortunately, if the second species is a molecule, the long range nature of the Coulomb interaction prohibits the cooling of the ro-vibrational degrees of freedom. Consequently, molecules cooled in this manner exhibit very low thermal temperatures while internally remaining hot. This problem was recently addressed by additionally loading laser cooled atoms into the same trap [37, 38]. Collisions with these neutral particles allow to efficiently cool all motional and internal degrees of freedom. As a result, using hybrid atom-ion traps (HAITrap) ground state molecular ions could be created [39, 40].

With all these currently available techniques, a large number of neutral atoms and molecules as well as atomic and molecular cations have been cooled to ultra-cold temperatures but there is still one massive blank spot on the map of ultra-cold particles, namely negatively charged ions. Up to date not a single anion has been cooled down to the ultra-cold regime even though they offer a very interesting field of research [41]. Anions play a curtail role in plasma physics [42] and they offer promising prospects for material science [43]. They also play

an important role in astro-physics as a large number of anions was found in the interstellar medium [44]. It would be therefore crucial to obtain high resolution spectroscopic data for these particles. A more peculiar but not less important application of ultra-cold anions is the sympathetic cooling of anti-protons. This would be a large milestone for the creation of stable anti-hydrogen [45] which is a fascinating system to study CPT violations [46, 47].

Nevertheless, anions have so far resisted all attempts to cool them into the ultra-cold regime. Direct laser cooling fails for most anions due to their lack of bound electronic transitions. There are however some proposals to cool negative osmium [48, 49] as well as lanthanum [50, 51] but direct laser cooling is limited to the few existing anions which do have bound electronic transitions. It is therefore desirable to develop new tools or extend the existing ones for the preparation of ultra-cold anion samples.

In this thesis we report on the prospects and first successful realization of a HAITrap which is designed for the sympathetic cooling of anions by laser cooled rubidium atoms. Such combined ion-neutral traps were first proposed a little more than ten years ago [52, 53] and have since been realized for a large number of different ion-atom combinations [54, 55, 56, 38, 57, 58, 59, 60, 61].

The prospects of sympathetically cooling the ions to the same temperature as the laser cooled atoms is hindered by an effect called collisional heating. All existing HAITraps consist of radio frequency traps where the ion is spatially confined by a rapidly oscillating electric field. If collisions with a cold buffer gas occur in this periodically driven system, an ion can gain a large amount of energy even if its collision partner is at rest. It was realized early on [62] that this collisional heating limits experiments to system where the mass of the neutral is smaller than the mass of the ion.

This limitation however is not strict and can be overcome by using radio frequency traps with a high multipole electric field or else by confining the buffer gas to the center of the trap. These approaches have been discussed in the literature for a long time but a satisfying theory on how these changes modify the mass ratio restriction was never developed.

The first part of this thesis presents a novel theoretical framework which has been developed to describe elastic ion-neutral collisions in our trap and which allows us to calculate the equilibrium energy distribution of the ions. Using this theory we can for the first time precisely predict how the traps multipole order influences the mass restrictions of the buffer gas. For a localized atom cloud we also found an exciting new regime which enables precise tuning of the final ion energy.

The second chapter presents the experimental setup of the HAITrap. This chapter is split into two main parts, the first one covering ev-

everything from the creation, to the trapping, to the detection of the negative ions. The second part focuses on the magneto optical trap for rubidium including an advanced imaging scheme which allows to precisely characterize the atom cloud even if the sample becomes optically thick.

The last chapter deals with the possibility of characterizing the negative ions inside the trap. Observation of sympathetic cooling requires precise measurements of the translational as well as ro-vibrational temperatures of the ion cloud. Unfortunately, all optical methods which are commonly used to characterize ultra-cold samples cannot be applied to anions, again due to their lack of bound electronic transitions. Therefore, the only way to obtain information about the anions is by photodetaching the electron which leads to a loss of the ion from the trap. This is a very powerful technique for two reasons: it allows to measure the ion density distribution by measuring the ion loss rate as a function of the detachment laser position (photodetachment topography), as well as measuring the ro-vibrational temperature by recording the loss rate as a function of the detachment laser wavelength (photodetachment spectroscopy).

Both of these techniques have been applied to a cloud of OH^- ions which is our first anion of interest. By overlapping the ion cloud with the laser cooled rubidium atoms we could observe changes in the ions density distribution which is the first ever indication of sympathetic cooling of anions inside a HAITrap.

SYMPATHETIC COOLING INSIDE RADIO FREQUENCY TRAPS

This chapter summarizes the work of three publications, one of which has been published [63], one is now available on the Arxiv [64] and the last being presently finished for submission. Additionally the topic has also been subject of a master thesis which was carried out in our group [65] and a proceedings article [66].

The ion motion inside a radio frequency (rf) trap is characterized by the interplay between a fast oscillation driven by the rf-field (micro-motion) and a much slower oscillation in the confining ponderomotive potential (macromotion) [67], thus representing a prototypical example of a dynamically driven nonlinear system [68]. Through elastic collisions with a cold buffer gas, either consisting of a cryogenic noble gas [69, 70, 71] or laser cooled atoms [54, 55, 56, 38, 57, 58, 59, 60, 61], the ion's motion can be efficiently reduced, thus opening a wide range of applications ranging from precision spectroscopy [72] and spectrometry [73, 74] over quantum computation [75] to cold chemical reactions dynamics [76] and astro-chemistry [77, 78]. However, elastic collisions influence the permanent exchange of energy between micro-motion and macromotion resulting in a net energy transfer from the micromotion to the macromotion [79, 80, 81, 82, 83]. As a consequence of this coupling, the ion's final mean energy generally exceeds the buffer gas temperature [84, 56, 85, 86] and the ion's energy distribution is predicted to deviate from a thermal distribution [80, 81, 83]. Due to the stability constraints of a rf trap, efficient cooling through collisions with buffer gas atoms can only be achieved for sufficiently low atom-to-ion mass ratios $\zeta = m_a/m_i$. For larger mass ratios, the ion experiences an effective energy gain through elastic collisions, even if the buffer gas is at zero temperature, finally resulting in loss from the trap. These two regimes are separated by the critical mass ratio ζ_{crit} , as first introduced by Major and Dehmelt [62]. In recent years, several groups have determined the critical mass ratio numerically [80, 81] as well as analytically [83] and found values slightly larger than Major and Dehmelt's first prediction $\zeta_{\text{crit}} = 1$.

In order to extend the regime of efficient cooling to lower final temperatures and larger mass ratios, two different approaches have been explored. Spatial confinement of the buffer gas, e.g. atoms stored in optical traps [55, 56, 38, 57, 58, 59, 60, 61], restricts collisions to the trap center where the micromotion is smallest, thus reducing

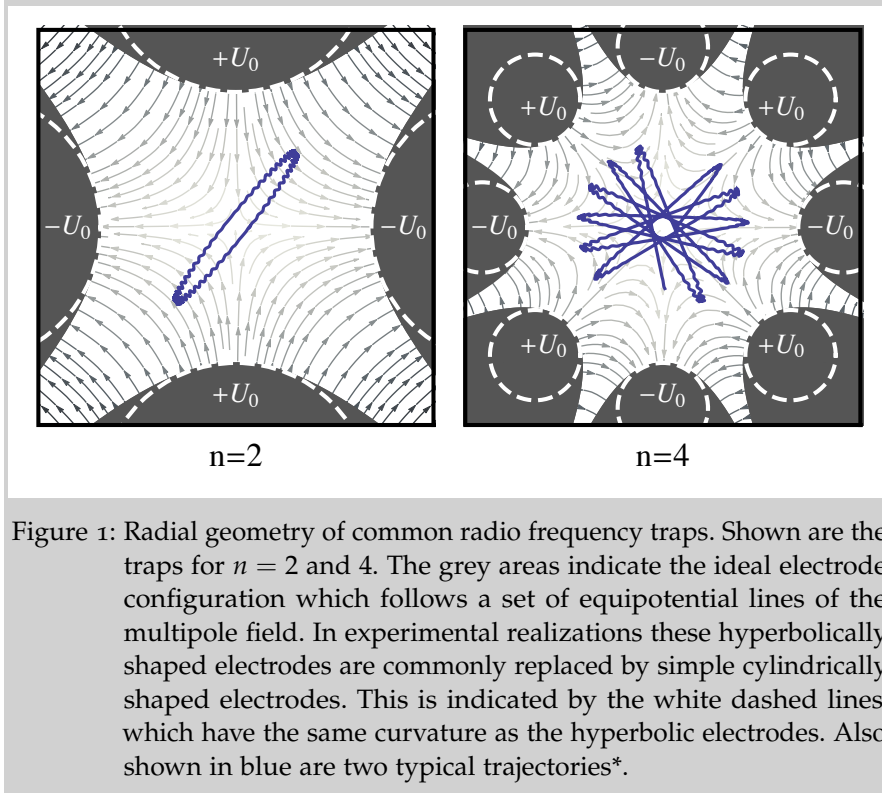
the collision induced energy transfer to the macromotion [87, 81, 38]. Alternatively, in RF traps with higher pole orders the micromotion is reduced over a larger volume thus allowing for efficient cooling with buffer gas [87, 88]. Despite a growing number of experiments using these approaches a general theoretical framework describing the influence of both a spatially confined buffer gas and high order RF traps is still lacking.

In this chapter a comprehensive model for the dynamics of a single ion interacting with a spatially confined buffer gas inside an rf trap of arbitrary pole order is presented. The collisional kinematics can be favorably described in a reference frame assigning the micromotion to the buffer gas rather than the ion. Depending on the mass ratio ζ , the ion's final energy is either determined by the buffer gas temperature ($\zeta \ll \zeta_{\text{crit}}$) or by the effective energy of the ion's micromotion ($\zeta \gg \zeta_{\text{crit}}$). For a homogeneous buffer gas, the micromotion restricts cooling to $\zeta < \zeta_{\text{crit}}$ in agreement with previous work. However, for a spatially confined cooling agent the emergence of an additional stable regime is found, thus enabling efficient cooling of the ion motion beyond ζ_{crit} . In this regime the ion's energy distribution is determined by the energy of the trap's ponderomotive potential V_{eff} averaged over the buffer gas distribution. We provide semi-analytic expressions for the ion's energy distribution for arbitrary mass ratios and trap multipole orders. As the averaged ponderomotive potential can be controlled, e.g. through adjustment of the trap parameters or the atom cloud size, the ion's final temperature can actively be changed offering perspectives for enhanced cooling (*forced sympathetic cooling*).

2.1 AN ION INSIDE A LINEAR RADIO FREQUENCY TRAP

Electric and magnetic fields provide an effective way to trap charged particles. Unfortunately, neither a constant electric, nor a constant magnetic field can create a three dimensional potential minimum in free space (Earnshaw's theorem). Instead a combination of both (e.g. Penning traps) or a time varying electric field (e.g. radio frequency traps) has to be used. In a penning trap the ions are radially confined by a strong magnetic field (usually several Tesla) and the axial confinement is achieved by an additional constant (dc) electric field. Due to the strong magnetic field and the poor optical access, Penning traps disqualify for any hybrid atom ion experiments where the atoms are prepared in a magneto optical trap. We will therefore focus on the second kind of traps, namely linear rf traps.

In linear rf traps, the radial confinement is achieved by an oscillating electric field, whereas axial confinement is achieved by an additional DC electric field. Linear rf traps exist with different pole orders n which describes the multipole order of the oscillating electric field, i.e. how many electrodes are used to create this field. The special case of a



quadrupole rf-trap ($n = 2$) is also known as linear Paul trap. In order to avoid confusion, it should be mentioned that there is a second kind of Paul trap, namely the three dimensional Paul trap. This trap differs from the linear trap (four radial and two endcap electrodes), as it only requires three electrodes (two endcaps and a ring electrode). In the following we will only cover linear rf-traps.

2.1.1 Radial confinement

In radial direction, an ideal multipole trap of order n creates a two dimensional electric field with only the n 'th term of the multipole expansion being non-zero [87]:

$$\begin{pmatrix} E_x \\ E_y \\ E_z \end{pmatrix} = E_0 n r^{n-1} \underbrace{\begin{pmatrix} -\cos[(n-1)\phi] \\ \sin[(n-1)\phi] \\ 0 \end{pmatrix}}_{\vec{e}_{mp}}, \quad (1)$$

with $r, \phi \rightarrow$ cylindrical coordinates
 $(r = \sqrt{x^2 + y^2}, \phi = \arcsin x/y),$
 $E_0 \rightarrow$ electric field strength,
 $n \rightarrow$ multipole order,
 $\vec{e}_{mp} \rightarrow$ unit vector of multipole field.

This is achieved by applying a voltage of $\pm U_0$ to $2n$ hyperbolically

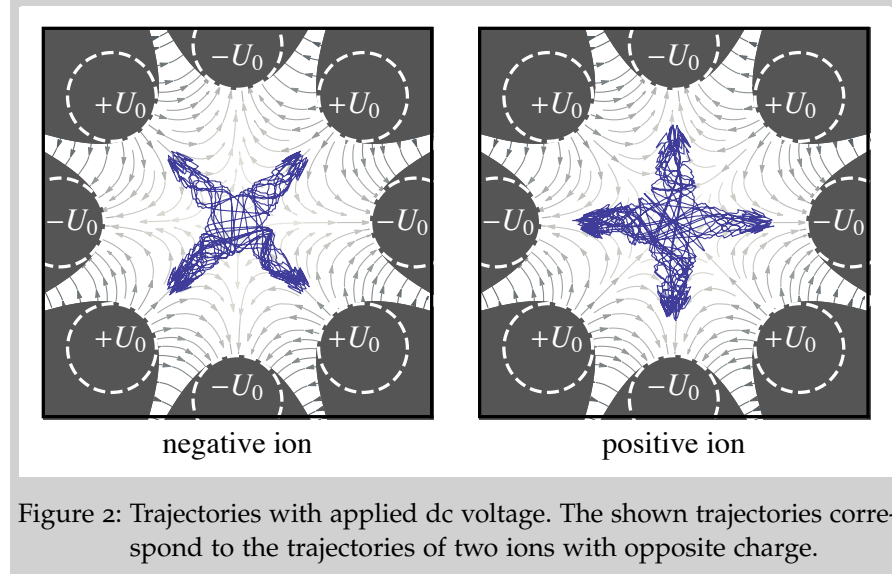


Figure 2: Trajectories with applied dc voltage. The shown trajectories correspond to the trajectories of two ions with opposite charge.

**Using cylindrical rods instead of hyperbolic electrodes, the ideal diameter of the rods is given by $d \approx 2R_0/(n-1)$. This is also why 22-pole traps are very common as for a trap with $n = 11$ and 1cm inner diameter, the ideal rods are exactly 1mm thick.*

shaped electrodes. Fig. 1 shows the resulting electrode configuration for $n = 2$ and 4 and a typical trajectory for both cases*. The surface of the electrodes follows a set of equipotential lines of the multipole field [89]. Choosing the distance of two adjacent electrodes to be $2R_0$, the electric field strength in Eq. (1) is given by $E_0 = U_0/R_0^n$. Placing an ion of charge Q_i and mass m_i in this field and applying a voltage of $U_0 = U_{DC} + U_{RF} \cos(\omega t)$ results to a force of

$$m_i \begin{pmatrix} \ddot{x} \\ \ddot{y} \\ \ddot{z} \end{pmatrix} = \frac{Q_i n}{R_0^n} (U_{DC} + U_{RF} \cos(\omega t)) r^{n-1} \vec{e}_{mp}, \quad (2)$$

acting on the ion,

with	U_{DC}	\rightarrow	trap's DC voltage,
	U_{AC}	\rightarrow	trap's RF voltage,
	ω	\rightarrow	RF frequency.

The two components of the applied voltage, i.e. the rf and dc part, have different effects on the ion's trajectory. The dc voltage creates a constant force pushing the ion away from the n electrodes which have the same polarity, attracting it towards the n electrodes with opposite polarity. This is illustrated in Fig. 2 which shows the ion trajectories inside an octupole trap ($n=4$) with a small dc voltage applied. Effectively, the dc voltage deforms the trajectories leading to a larger ion density close to the electrodes of opposite polarity. The actual trapping force is only created by the rf voltage. At first glance one could expect that the oscillating part of the force averages out. In order to understand how the oscillating part creates a net force to the center of the trap, thus creating stable trapping conditions, we will compare two different scenarios.

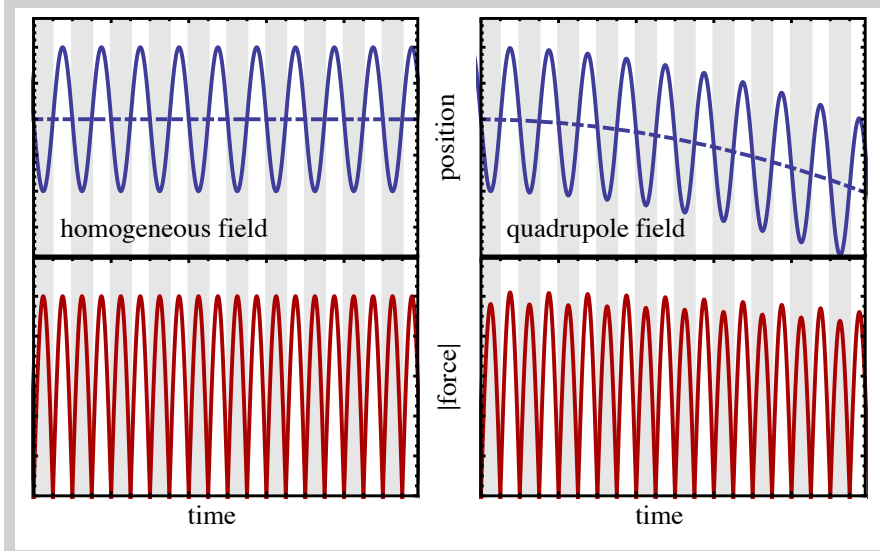


Figure 3: Field gradient force. The two upper graphs show the ion's position as a function of time. The ion is initially at rest. The two lower graphs show the absolute force acting on the ion. The sign of the force is indicated by the background color.

Fig. 3 shows the ion trajectories inside a homogeneous and a quadrupole electric field, the quadrupole field corresponds to a Paul trap, the homogenous case corresponds to an ion placed in a simple plate capacitor with an rf voltage applied. Assuming the ion is initially at rest, it simply oscillates around its initial rest position in the homogenous field. This situation significantly changes in case of the quadrupole field which corresponds to an rf trap with $n = 2$. In such a field the ion experiences a net force to the trap center. This can be understood by looking at the amplitude of the forces shown in the bottom part of Fig. 3. Only the absolute value of the force is shown, the sign of the force is indicated by the background color. In areas with grey/white background the force is pointing upwards/downwards. Whereas in the homogeneous case, there is a perfect balance between the upwards and downwards pointing force, these forces become imbalanced in the inhomogeneous case. The asymmetry is caused by the radial dependence of the oscillating force which is zero at the trap center and grows with increasing radius as $F \propto r^{n-1}$ (see Eq. (2)). This results in a net force towards the center of the trap, which on longer time scales leads to a second oscillation around the center of the trap, as seen in Fig. 1. The fast oscillation in the RF field is called micromotion, the slower drift motion around the center of the trap is called macromotion.

The ion's equation of motion inside the trap (Eq. (2)) is a nonlinear second order differential equation. For the special case $n = 2$ (Paul trap) the equations (x, y and z component) decouple and are equivalent to the Mathieu differential equations which can be solved

analytically. For all higher multipole orders ($n > 2$), the Mathieu formalism does not work and the equation of motion cannot be solved analytically. However, if the characteristic time scale of micro- and macromotion can be separated, a different formalism, known as the adiabatic approximation, can be applied.

2.1.2 Mathieu equations

Inside a linear Paul trap, the spatial degrees of freedom, i.e. the x - and y -motion, are no longer coupled, as

$$r^{n-1} \begin{pmatrix} -\cos[(n-1)\phi] \\ \sin[(n-1)\phi] \\ 0 \end{pmatrix} \stackrel{n=2}{=} \begin{pmatrix} -x \\ y \\ 0 \end{pmatrix}. \quad (3)$$

Plugging this into Eq. (2) and substituting $2\tau = \omega t$, the equations of motion are equivalent to the Mathieu differential equations

$$\begin{aligned} \frac{d^2x}{d\tau^2} + (a + 2q \cos(2\tau))x &= 0 \\ \frac{d^2y}{d\tau^2} - (a + 2q \cos(2\tau))y &= 0 \end{aligned} \quad (4)$$

with	$a = \frac{8Q_i U_{DC}}{m_i R_0^2 \Omega^2}$	\rightarrow	DC stability parameter,
	$q = \frac{4Q_i U_{AC}}{m_i R_0^2 \Omega^2}$	\rightarrow	AC stability parameter,
	$\tau = \frac{\omega t}{2}$	\rightarrow	normalized time.

These equations can be solved by a Fourier series known as the Mathieu sines and cosines which are well discussed in the literature [90, 91]. There exists a well defined set of parameters u and q leading to stable trajectories. Fig. 4 shows the resulting stability diagram for a Paul trap. The difference in x - and y -stability arises from the dc-voltage, as it breaks the symmetry of the oscillating field. In the regions where the x - and y -stabilities overlap, the ion trajectory becomes globally stable. There is an unlimited number of stable regions on the u, q -plane, three of which are shown in Fig. 4, marked as A, B and C. In most experimental realizations, rf traps are operated in region A. Moreover, in most traps no dc voltage is being applied. These operating conditions correspond to points on the q -axis of the stability diagram with $q < q_{\text{crit}} \approx 0.908$. Beyond q_{crit} the trajectories become unstable and the amplitude of the ion's oscillation around the trap center grows exponentially. This can be seen in Fig. 5, which shows ion trajectories for different η values, which in case of a Paul trap is equivalent to the q parameter. In the literature the parameter q is mostly used in the context of a Paul trap, whereas η is used for all other trap orders $n > 2$. A proper definition of the stability parameter η will be derived in the following.

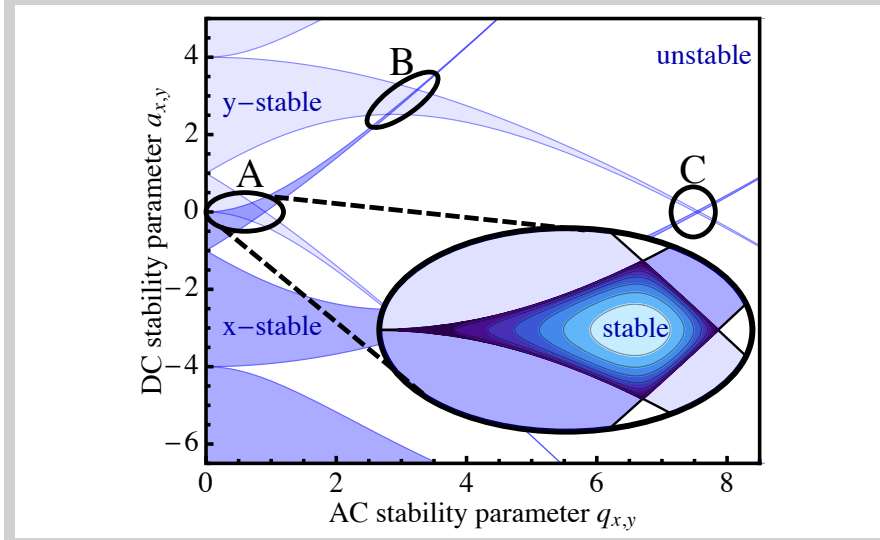


Figure 4: Stability diagram of a Paul trap*. The stability of the ion trajectory in x - and y -direction on the u, q -plane is shown. The areas with global stability are marked by A, B and C. The inset shows a zoom into the first stable region (A).

2.1.3 Adiabatic approximation

For traps with $n > 2$, the Mathieu formalism does not work, as the equations of motion cannot be decoupled. In this case the adiabatic approximation can be applied. Instead of separating the x - and y -component of the ion's motion, the ion motion is separated into two distinct time scales [87, 88]. The fast time scale is set by the ion's oscillation in the rf field (micromotion) and the slow time scale is given by the drift motion around the trap center (macromotion). Mathematically the separation into two time scales is expressed by splitting the trajectory $\vec{R}(t)$ into two components

$$\vec{R}(t) = \vec{R}_d(t) + \vec{R}_{rf}(t). \quad (5)$$

$\vec{R}_d(t)$ denotes the slow drift motion around the trap center (macromotion) and $\vec{R}_{rf}(t)$ is the fast oscillation which follows the rf-field (micromotion). Plugging this into Eq. (2) and expanding the force $\vec{F}(\vec{R}(t)) = m_i(\ddot{x}, \ddot{y}, \ddot{z})$ in a Taylor series around the point $\vec{R}_d(t)$ leads to

$$\underbrace{m_i \frac{d^2}{dt^2} \vec{R}_d}_{1st} + \underbrace{m_i \frac{d^2}{dt^2} \vec{R}_{rf}}_{2nd} = \underbrace{\vec{F}(\vec{R}_d)}_{3rd} + \underbrace{(\vec{R}_{rf} \vec{\nabla}) \vec{F}(\vec{R}_d)}_{4th} + \dots, \quad (6)$$

with the series being truncated after the term linear in \vec{R}_{rf} . This is only justified if the amplitude of the micromotion is small compared to the amplitude of the macromotion ($\vec{R}_d(t) \ll \vec{R}_{rf}(t)$). The stability parame-

*The stability diagram looks different for the three dimensional Paul trap, consisting of a ring and two endcap electrodes. In this case it is distinguished between r - and z -stability with the r -stability region being stretched by a factor of two in both directions. This leads to asymmetric stability regions.

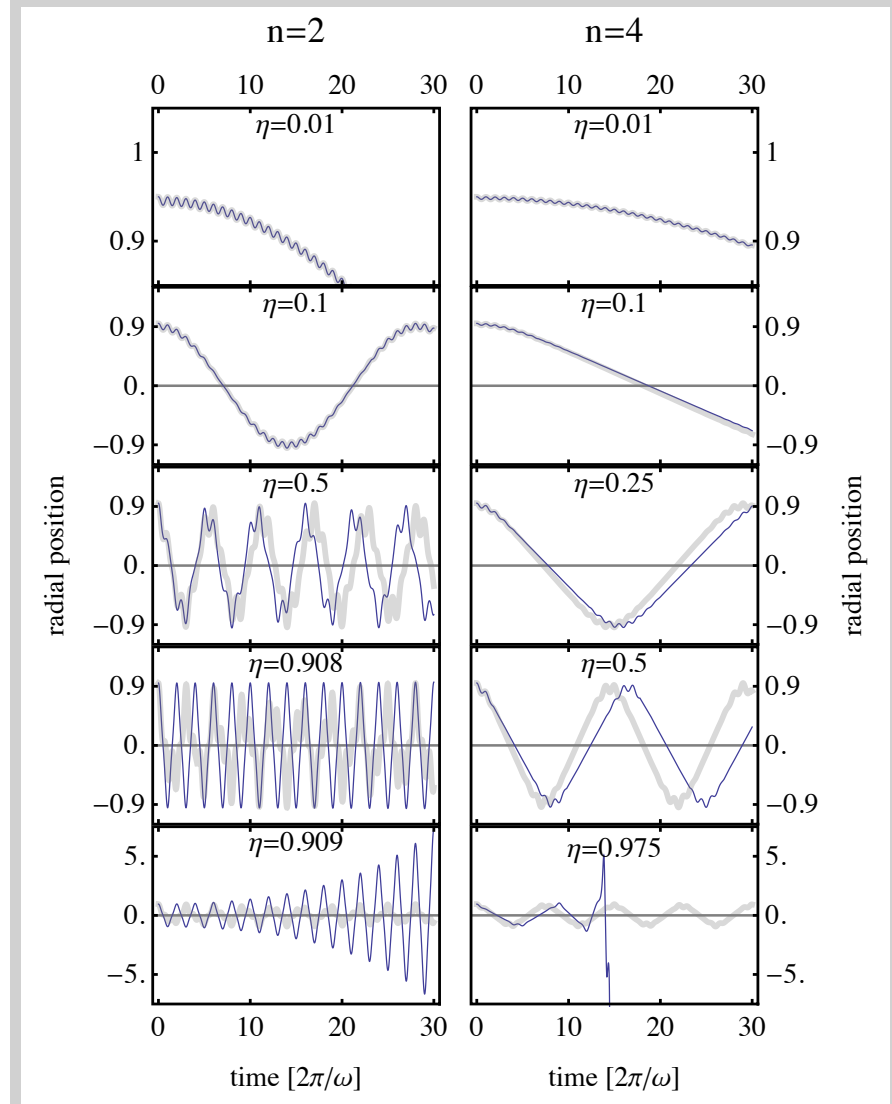


Figure 5: Ion trajectories for different stability parameters. The blue curves correspond to the exact solution of the ion's motion. The grey curves show the result of the adiabatic approximation. With increasing stability parameter, both results show a growing discrepancy. For large values of η the exact solutions become unstable.

ter η [92, 87] quantifies this condition, by comparing the magnitude of the third and fourth term in Eq. (6)

$$\eta = \frac{2(\vec{R}_{\text{rf}} \cdot \vec{\nabla}) \vec{F}(\vec{R}_d)}{\vec{F}(\vec{R}_d)} = q(n-1) \left(\frac{r}{r_0} \right)^{n-2}. \quad (7)$$

Consequently, truncating the Taylor series after the linear term is only justified for $\eta \ll 1$. The additional factor of two in the definition of η is used so that in case of a Paul trap the stability parameter η exactly equals the Mathieu parameter q . The Paul trap also has the unique feature that the stability parameter η is independent of the radial position of the ion. Fig. 5 shows the ion trajectories, for different

stability parameters and multipole orders. For $\eta \ll 1$, the period and amplitude of the micromotion are much smaller than the ones of the macromotion. With increasing η , the periods/amplitudes become of the same order of magnitude until they are essentially the same and it can no longer be distinguished between micro- and macromotion. This is the point where the trajectories become unstable. For a Paul trap this corresponds to the critical value $\eta = q_{\text{crit}}$ introduced earlier. This kind of stringent separation into stable and unstable trajectories cannot be done for any higher order trap, as the stability parameter directly depends on the ion's radial position.

The adiabatic approximation makes use of the fact that for $\eta \ll 1$, the characteristic time scale of the drift motion $\vec{R}_d(t)$ is much longer than the period of the fast oscillation $\vec{R}_{\text{rf}}(t)$, i.e. $\vec{R}_d(t)$ does not significantly change during one rf oscillation. In this case, Eq. (6) can be separated into a motion on long time scales (first and fourth term) and a motion on the time scale of the rf-oscillation (second and third term). The motion on fast time scales (micromotion) is solved by an oscillatory motion following the rf-field

$$\vec{R}_{\text{rf}}(r, \phi, t) = \frac{qr_0}{2} \left(\frac{r}{r_0}\right)^{n-1} \cos(\omega t) \vec{e}_{\text{mp}}, \quad (8)$$

with $q = \frac{2nQ_i U_{\text{AC}}}{m_i R_0^2 \Omega^2}$	\rightarrow	rf stability parameter*
$\vec{e}_{\text{mp}} = \begin{pmatrix} -\cos[(n-1)\phi] \\ \sin[(n-1)\phi] \\ 0 \end{pmatrix}$	\rightarrow	unit vector multipole field.

**Note that in contrast to the Mathieu equations, the factor of 4 in the RF stability parameter was replaced by 2n.*

Plugging this into the equation for long time scales and averaging over one rf-oscillation ($\sin^2(\omega t) \rightarrow 1/2$) yields the macromotions's equation of motion

$$\frac{d^2}{dt^2} \vec{R}_d(r) = -\frac{q^2 \omega^2}{4r_0} (n-1) \left(\frac{r}{r_0}\right)^{2n-3} \vec{e}_r, \quad (9)$$

with $\vec{e}_r \rightarrow$ radial unit vector.

Using the relation $\vec{F}(\vec{R}_d) = -\vec{\nabla} V_{\text{eff}}$ the macromotion can be expressed as a motion in an effective potential

$$V_{\text{eff}}(r) = \frac{q^2 \omega^2}{16} \left(\frac{r}{r_0}\right)^{2n-2}. \quad (10)$$

The effective potential ranges from a harmonic potential in case of a Paul trap to a box-like potential for $n \rightarrow \infty$. This has two interesting consequences, differentiating the Paul trap from all other rf traps. Firstly, neglecting the micromotion, the Paul trap is the only rf trap that exhibits closed ion trajectories (see Fig. 1). This is a direct consequence of Bertrand's theorem which states that there is only two types of central potentials leading to closed orbits, namely $V(r) \propto r^2$ and

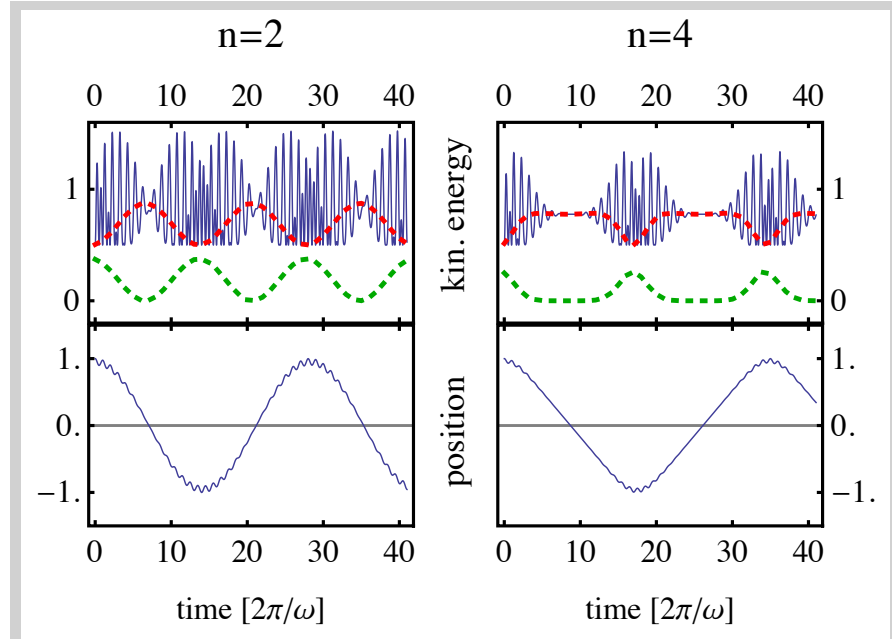


Figure 6: Ion's kinetic energy and position over several micromotion oscillations. The upper panels show the ion's total kinetic energy (Blue) as a function of time. Also shown is the kinetic energy of the macromotion (red) and the effective potential at the position of the ion. The macromotion energy is obtained by probing the ion's energy at every zero crossing of the micromotion velocity ($\omega t = \pi, 2\pi, \dots$). The lower panels show the ion's position. The ion oscillates through the trap center ($L = 0$).

$V(r) \propto 1/r$ (e.g. planetary motion in the solar system). The second unique feature of the Paul trap is a constant macromotion period, i.e. the oscillation period is independent of the initial displacement. This well known quality of harmonic potentials is also why the stability parameter η of a Paul trap is independent of the radial position.

Fig. 5 shows different ion trajectories calculated with the exact equation of motion from Eq. (2) (blue curve) and using the adiabatic approximation (grey curve). As expected, both solutions show good agreement for small η , whereas they show a growing discrepancy with increasing η as the adiabatic expression loses its validity. As we will make use of the adiabatic approximation in the following, all our discussions are limited to small stability parameters. Generally, sufficient agreement with the exact solution is found for $\eta < 0.1$.

2.1.4 Constants of the ion motion

In all conservative systems the total energy is a constant of motion. This is not the case in the periodically driven system of an ion inside an rf trap. Fig. 13 shows the ion's energy for an ion oscillating through the trap center. The energy oscillates with the rf field exhibiting the

strongest oscillations at the radial turning point r_{turn} of the macro-motion oscillation. It is apparent that the ion's total kinetic energy is not very useful for characterizing the state of the system. A better definition of the ion's energy can be made in the adiabatic approximation, by averaging the ion's kinetic energy over one rf-oscillation. This results in a constant value E_i , which we will associate with the ion's total energy. Separating this energy into a radial (E_r) and an axial (E_z) component results in the following expressions

$$E_i = E_z + E_r , \quad (11)$$

$$E_z = \frac{1}{2} m_i v_{d,z}^2 , \quad (12)$$

$$\begin{aligned} E_r &= \frac{1}{2} m_i v_{d,r}^2 + \frac{1}{2} m_i \langle v_{\text{rf}}^2 \rangle \\ &= \frac{1}{2} m_i v_{d,r}^2 + V_{\text{eff}}(r) , \end{aligned} \quad (13)$$

with $v_{\text{rf}} \rightarrow$ micromotion velocity,
 $v_{d,r} \rightarrow$ radial component of macromotion velocity,
 $v_{d,z} \rightarrow$ axial component of macromotion velocity.

It should be pointed out that the micromotion is a pure radial motion with no axial component whereas the macromotion can point in any direction. In the definition of E_r we used the fact that the micromotion averaged over a single RF-period equals the effective potential (Eq. (10)). The two contributions of E_r are shown by the dashed curves in Fig. 13.

The ion's energy can be translated into a characteristic length scale of the system using the effective potential. In the following we will use the three characteristic radii,

$$V_{\text{eff}}(r_{\text{lim}}) = E_i , \quad (14)$$

$$V_{\text{eff}}(r_{\text{max}}) = E_r , \quad (15)$$

$$V_{\text{eff}}(r_{\text{turn}}) = E_r - L^2 / (2m_i r_{\text{turn}}^2) , \quad (16)$$

with $L = m_i |\vec{r} \times \vec{v}_{d,r}| \rightarrow$ angular momentum in radial plane.

The radius r_{turn} denotes the ion's actual turning point in the effective potential. This turning point depends on the ion's angular momentum, which is another constant of the ion's motion. Fig. 7 illustrates the dependence of the three radii for different trap orders and angular momenta. For $L = 0$ the ion oscillates through the center of the trap, whereas for $L \neq 0$ there exists a region at the center of the trap which cannot be probed by the ion (gray area in Fig. 7). The probability to find an ion with arbitrary angular momentum L and radial energy E_r

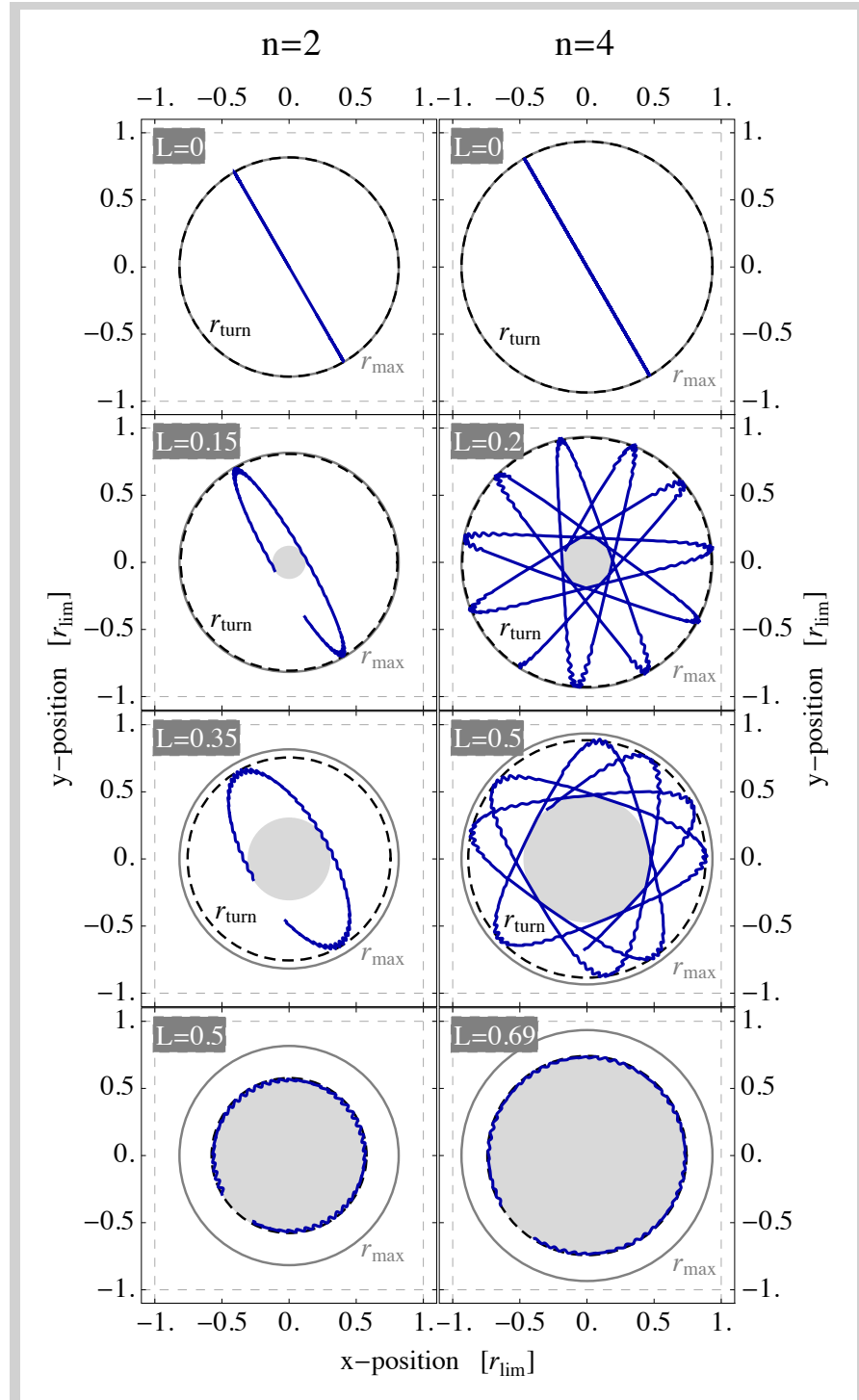


Figure 7: Ion trajectories for different angular momenta and multipole orders. The ion has equal kinetic energy in all three spatial dimensions. The ion trajectories are shown in blue in relation to the different characteristic radii, as defined in Eq. (14)-(16). The angular momenta were normalized by scaling the radius as well as the radial velocity with respect to r_{\max} , resulting in $L_{\text{norm}} = |(\vec{r}/r_{\max}) \times (\vec{v}_{d,r}(r)/v_{d,r}(r=0))|$. This normalized angular momentum has a defined maximum value L_{\max} . In a Paul trap $L_{\max} = 1/2$ and for $n \rightarrow \infty$ it tends towards unity. For $L_{\text{norm}} = L_{\max}$ the ion has a perfect circular orbit, for $L_{\text{norm}} = 0$ it oscillates through the trap center. The grey areas at the center represent the area in the radial plane which cannot be probed by the ion due to angular momentum conservation.

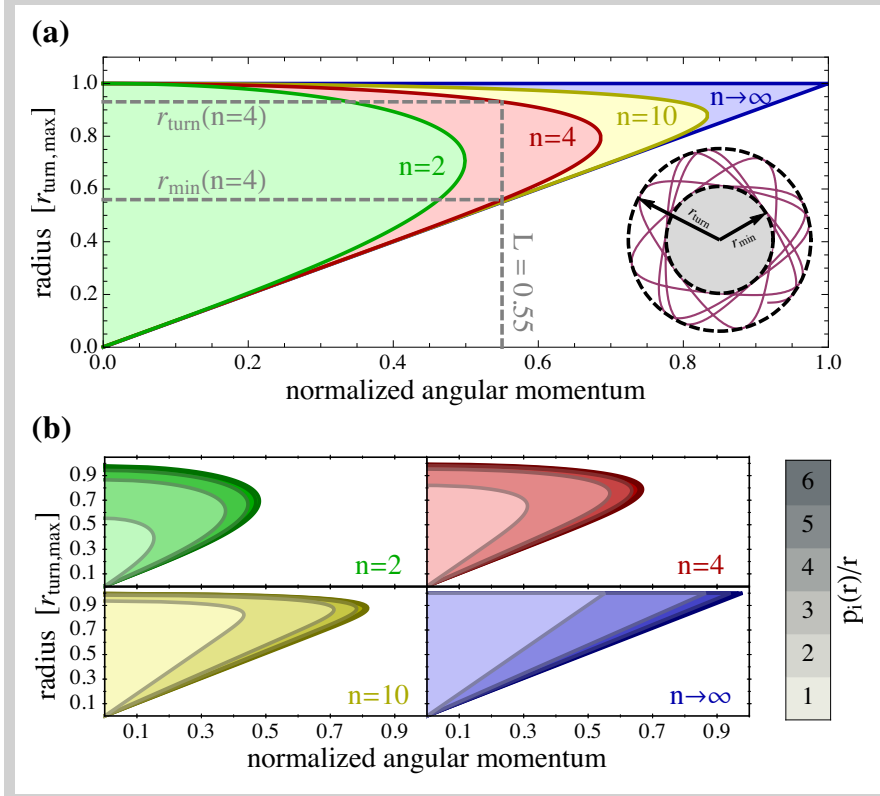


Figure 8: Ion's spatial probability distribution. The upper graph (a) shows the ion's minimum and maximum radius for different angular momenta and multipole orders. The inset shows an exemplary trajectory (red) with r_{turn} and r_{min} being indicated by the dashed circles. The lower graph (b) shows the radial probability distribution as a function of the angular momentum. In analogy to a one-dimensional pendulum, the probability distribution diverges at the radial turning points as the radial velocity \dot{r} becomes zero.

at a radius r is proportional to the inverse of the ion's radial velocity \dot{r} , which can be expressed as

$$p_i(r) \propto \left(\frac{2}{m_i} (E_r - V_{\text{eff}}(r)) - \frac{L^2}{m_i^2 r^2} \right)^{-1/2}. \quad (17)$$

Fig. 8 shows the spatial probability distribution for different trap orders.

2.2 ION-NEUTRAL COLLISIONS INSIDE AN RF TRAP

So far we identified three constants of motion, namely the radial and axial components of the ion's energy (Eq. (13) and (12)) and the angular momentum in the radial plane. We will now investigate how these three parameters change if the ion collides with a neutral buffer gas atom.

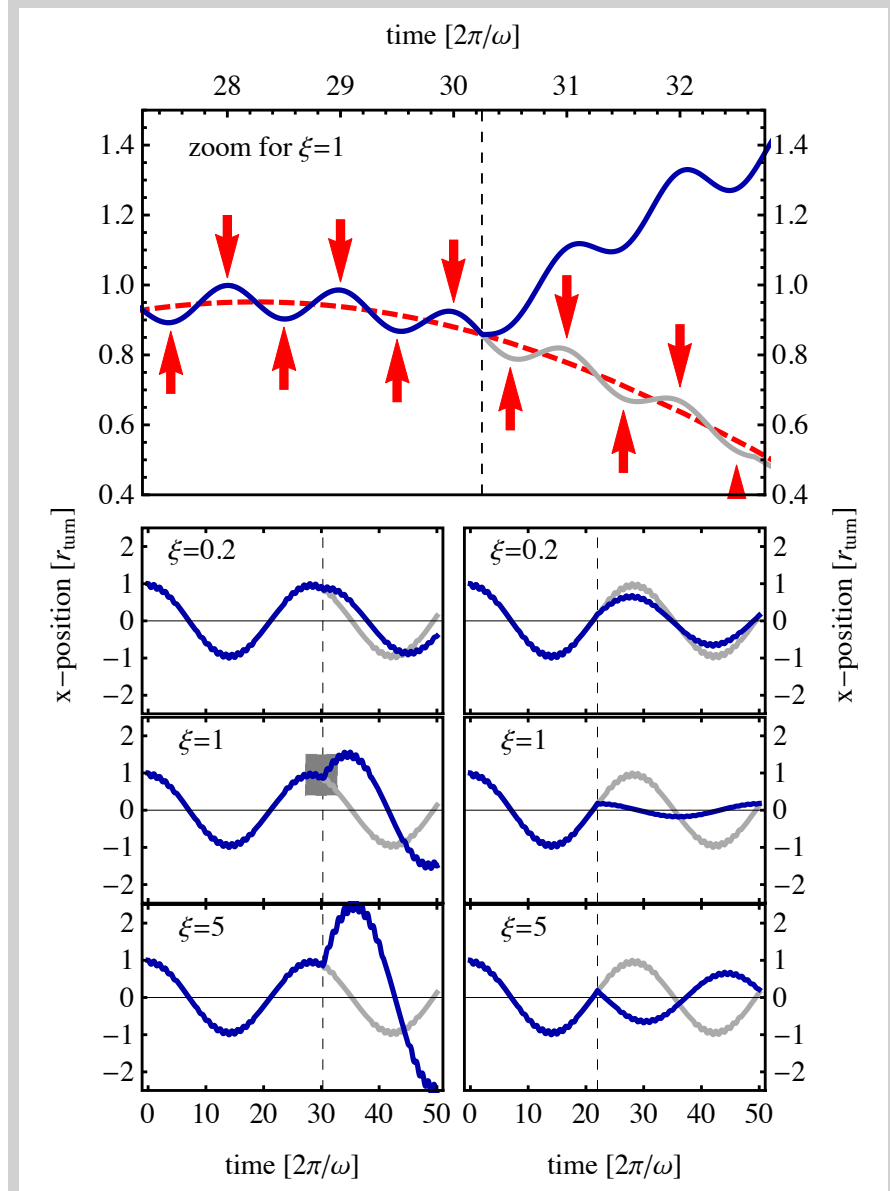


Figure 9: Elastic buffer gas collision. The shown trajectories (blue) correspond to a head on collision with a buffer gas atom which is initially at rest. Also shown are the unperturbed trajectories (grey). The six panels at the bottom correspond to three different mass ratios and two collision times. The upper graph shows a zoom into the area indicated by the dark grey box. The details of the upper graph are explained in the text. All trajectories lie in the radial plane and pass through the trap center ($v_{d,z} = 0$, $L = 0$).

2.2.1 Collisional heating

In a conservative system, an ion emerged into a neutral buffer gas cloud thermalizes to the buffer gas temperature. This is not the case for the periodically driven system of an rf trap. Inside the trap, even an ion colliding with a resting atom can gain a multiple of its initial

energy in a single elastic collision. Fig. 9 shows different ion trajectories including a single head-on collision with a buffer gas atom at rest. Also shown is a close-up of a collision around the ion's turning point r_{turn} where the amplitude of the micromotion is largest. Shown are the ion's trajectory without any collision (grey curve), the trajectory including a collision (blue curve) and the unperturbed trajectory excluding the micromotion (red dashed curve). Every time the ion crosses the red line, the rf field and thus the force acting on the ion, changes sign. The direction of the force is indicated by the red arrows.

We will first consider the unperturbed trajectory. In the absence of any collision, the force always points towards the red line which corresponds to the ion's drift motion (macromotion). The drift itself and thus the effective potential, is caused by the fact that the force exhibits a radial dependence of $F(r) \propto r^{n-1}$ (Eq. (2)). This leads to an imbalance between the upward and downward pointing force, resulting in a net force towards the trap center, also known as the field gradient or ponderomotive force. During a single period of the force pointing in one direction, the ion is first decelerated for half the period and then accelerated back in opposite direction during the second half.

This situation dramatically changes, if a collision occurs. In the trajectory shown in Fig. 9 (top panel), the time of the collision was chosen to be the exact moment when the rf-field changes its sign. Due to the head-on collision with the resting atom ($m_a = m_i$) the ion immediately comes to a complete stop. Afterwards, the ion is accelerated away from the red line for a full period, forcing it beyond the initial turning point r_{turn} . The resulting increased oscillation amplitude corresponds to an increase of the ion's energy, also known as rf-heating.

The bottom panels in Fig. 9 show the trajectories on a longer time scale for three different atom to ion mass ratios ζ and two different collision times. The three graphs on the left side show the same scenario as before with the collision occurring close to the ion's turning point in the effective potential. The graphs on the right correspond to collisions close to the trap center. For these two limiting cases, simple analytical expressions for the relative energy transfer through an elastic collision can be found,

$$\frac{\Delta E_i}{E_i} = \begin{cases} -\frac{4\zeta}{(1+\zeta)^2} & (r \simeq 0), \\ +\frac{8\zeta^2}{(1+\zeta)^2} \cos^2(\Phi_{\text{RF}}) & (r \simeq r_{\text{lim}}). \end{cases} \quad (18)$$

While the ion's energy loss due to collisions close to the trap center is most efficient for equal masses ($\zeta = 1$), the energy gain for collisions close to r_{lim} increases monotonically with the mass ratio, reaching up to eight times the ion's initial energy in a single collision for $\zeta \gg 1$. It is this dependence, which explains the emergence of a critical mass ratio, beyond which ions can no longer be cooled efficiently.

2.2.2 Elastic collision inside an rf trap

Elastic collisions are best treated by transforming all velocities into the center-of-mass (COM) frame which is defined by the COM velocity

$$\vec{V}_{\text{COM}} = \frac{m_i \vec{v}_i + m_a \vec{u}_a}{m_i + m_a}, \quad (19)$$

with $\vec{v}_i = \vec{v}_d + \vec{v}_{\text{rf}}$	→	ion's total velocity,
\vec{u}_a	→	buffer gas atom's velocity.

The atom's and ion's initial velocities in the lab frame can be expressed by the COM velocity and the relative velocity $\vec{v}_{\text{rel}} = \vec{v}_i - \vec{u}_a$, as

$$\begin{aligned} \vec{v}_i &= \vec{V}_{\text{COM}} + \frac{m_a}{m_i + m_a} \vec{v}_{\text{rel}}, \\ \vec{u}_a &= \vec{V}_{\text{COM}} - \frac{m_i}{m_i + m_a} \vec{v}_{\text{rel}}, \end{aligned} \quad (20)$$

with the second term of both sums being the ion's and atom's velocity in the COM frame. An elastic collision simply rotates the velocities in the COM frame, without changing their magnitudes. This results in a final ion velocity of

$$\vec{v}'_i = \vec{V}_{\text{COM}} + \frac{m_a}{m_i + m_a} \mathcal{R}(\theta_c, \phi_c) \vec{v}_{\text{rel}}, \quad (21)$$

with $\mathcal{R}(\theta_c, \phi_c)$	→	rotation matrix with polar and azimuthal scattering angles θ_c and ϕ_c .
--------------------------------------	---	--

As discussed previously, the ion's total velocity is not a very useful quantity as it is not conserved (see Fig. 6). Instead, the relevant quantity is the ion's macromotion as it defines all three constants of motion E_r , E_z and L . The final velocity of the macromotion is obtained by decomposing the ion's total velocity before and after the collision into its two components, namely $\vec{v}_i = \vec{v}_d + \vec{v}_{\text{rf}}$ and $\vec{v}'_i = \vec{v}'_d + \vec{v}'_{\text{rf}}$. The micromotion is an implicit function of the radial position r and the rf phase ωt (see Eq. (8)). As the duration of the collision is typically small compared to the period of the micromotion, one can assume that the micromotion remains unchanged during the course of the collision ($\vec{v}_{\text{rf}} = \vec{v}'_{\text{rf}}$). Plugging this into Eq. (21) yields a final macromotion velocity of

$$\vec{v}'_d = \frac{m_i \vec{v}_d + m_a \vec{u}_{\text{eff}}}{m_i + m_a} + \frac{m_a}{m_i + m_a} \mathcal{R}(\theta_c, \phi_c) (\vec{v}_d - \vec{u}_{\text{eff}}) \quad (22)$$

with $\vec{u}_{\text{eff}} = \vec{u}_a - \vec{v}_{\text{rf}}$	→	effective atom velocity.
---	---	--------------------------

2.2.3 The effective buffer gas picture

The effective atom velocity is chosen in a way that Eq. (21) and (22) become formally equivalent with $\vec{v}_i \simeq \vec{v}_d$ and $\vec{u}_a \simeq \vec{u}_{\text{eff}}$. Consequently, elastic collisions in an rf-trap can be described by an ion moving in the effective potential V_{eff} , colliding with buffer gas atoms exhibiting the spatial and time dependent velocity \vec{u}_{eff} . In this picture, the average effective energy of the buffer gas atoms is given by

$$\langle E_a \rangle = \frac{1}{2} m_a (\langle \vec{u}_a^2 \rangle + 2 \langle \vec{u}_a \vec{v}_{\text{rf}} \rangle + \langle \vec{v}_{\text{rf}}^2 \rangle). \quad (23)$$

The first term on the right side is the thermal energy of the buffer gas, the second term vanishes, as the thermal velocity is not correlated with the micromotion and the last term is proportional to the effective potential. For a thermal buffer gas this results in an average effective energy of

$$\langle E_a(r) \rangle = \frac{1}{2} m_a \langle u_{\text{eff}}^2 \rangle = \zeta V_{\text{eff}}(r) + \frac{3}{2} k_B T_a \quad (24)$$

with $k_B \rightarrow$ Boltzmann constant,
 $T_a \rightarrow$ buffer gas temperature.

The buffer gas exhibits an effective energy distribution, given by a Boltzmann distribution at the trap center, where micromotion can be neglected, with an increasing contribution of the micromotion for larger radii.

By comparing the radial dependence of the atoms effective energy to the one of the ion, as given by $\frac{1}{2} m_i v_d^2(r)$ (see Eq. (13)), two distinct regions, separated by the critical cooling radius r_c , can be identified: For $r < r_c$ the ion's kinetic energy exceeds the average energy of the atoms resulting in a net energy transfer to the atoms, whereas for $r > r_c$ the ion's energy is generally increased through a collision with the buffer gas atom. The radius r_c is obtained by solving the equation $\langle E_a(r_c) \rangle = E_i - V_{\text{eff}}(r_c)$ which leads to a critical cooling radius of

$$r_c = r_{\text{lim}} \left(\frac{1 - \frac{3}{2} k_B T_a / E_i}{1 + \zeta} \right)^{\frac{1}{2n-2}}. \quad (25)$$

For $E_i < k_B T_a$, the net energy transfer is always positive and thus the radius r_c no longer defined. In case the ion's energy is large compared to $\frac{3}{2} k_B T_a$, the cooling volume is always a fixed fraction of the total volume probed by the ion.

The micromotion induced heating at large radii is amplified with larger atom-to-ion mass ratio, as the velocity of the micromotion $v_{\text{rf}} \propto 1/m_i$, now being assigned to the atom of mass m_a , leads to the prefactor ζ in the effective buffer gas energy (see Eq. (24)). Hence, at large mass ratios and small multipole orders, the ion essentially

gains energy through collisions, whereas at low mass ratios and large multipole orders the energy is primarily reduced.

These considerations offer an intuitive picture for the occurrence of a critical mass ratio ζ_{crit} , beyond which the ion effectively gains energy through buffer-gas collisions, eventually resulting in the ion's loss from the trap. The critical mass ratio can be estimated by averaging the energy change $\Delta E_i = \frac{1}{2}m_i(\vec{v}'_d{}^2 - \vec{v}_d{}^2)$ over one rf-period which results in

$$\langle \Delta E_i \rangle = \frac{m_i m_a (1 - \cos \theta_c)}{(m_i + m_a)^2} [m_a \langle v_{\text{rf}}^2 \rangle - m_i \langle v_d^2 \rangle]. \quad (26)$$

The first term on the right side is proportional to the average effective potential $\langle V_{\text{eff}} \rangle$, the second term to the average kinetic energy of the macromotion $\langle E_d \rangle$. For the critical mass ratio, the average energy transfer has to be zero, which leads to the condition $\langle E_d \rangle = \zeta_{\text{crit}} \langle V_{\text{eff}} \rangle$. Assuming that the ion motion in the trap's effective potential obeys the virial theorem. The ratio between average potential and kinetic energy is given by $\langle V_{\text{eff}} \rangle / \langle E_d \rangle = 2 / (3n - 3)$ which results in a critical mass ratio of

$$\zeta_{\text{crit}} = \frac{3}{2}(n - 1). \quad (27)$$

The critical mass ratio grows linearly with the multipole order of the trap. Consequently, for any mass ratio a sufficiently large multipole order can be found which leads to stable trapping conditions. It should be noted, that Major and Dehmelt originally estimated the critical mass ratio for a Paul trap to be $\zeta_{\text{crit}} = 1$. This reduced critical mass ratio corresponds to a pure two dimensional system, where the ion has no velocity component in z -direction. In the following we will numerically calculate the critical mass ratio as the point where the mean energy of the ion's energy distribution diverges [80, 81, 83]. This alternative definition is commonly used in the literature and leads to the same linear multipole order dependence with a slightly varied pre-factor.

2.2.4 Collisional energy transfer

The relative change of the ion's energy $\Delta E_{\text{tot}} / E_{\text{tot}} = (\vec{v}'_d / \vec{v}_d)^2 - 1$ depends on the different parameters in Eq (22). Assuming that the buffer gas has zero temperature, i.e. $u_a = 0$, the initial conditions are given by the absolute values of the micro- and macromotion velocities and the angle between the two which we denote with α . The absolute micro- and macromotion velocities can be expressed as

$$v_{\text{rf}}(r) = \sqrt{\frac{4V_{\text{eff}}(r)}{m_i}} \sin(\omega t) \quad \text{and} \quad (28)$$

$$v_d(r) = \sqrt{\frac{2(E_{\text{tot}} - V_{\text{eff}}(r))}{m_i}}. \quad (29)$$

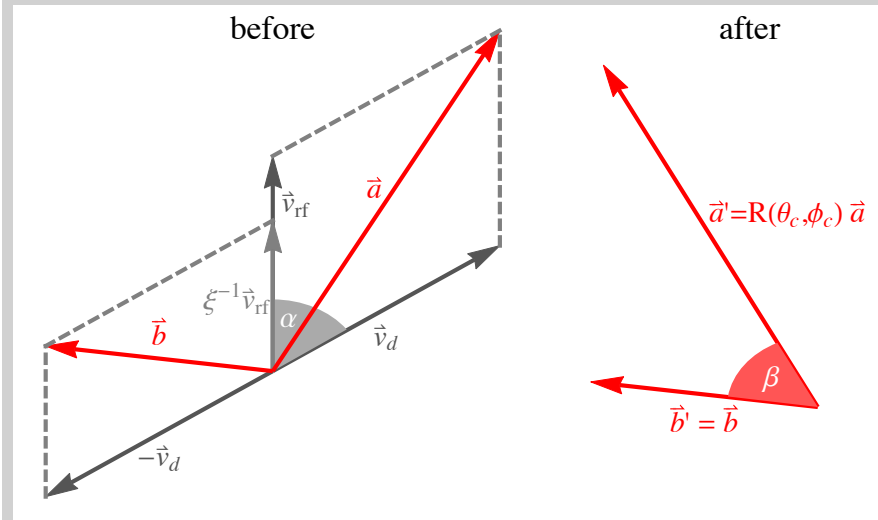


Figure 10: Schematic of an elastic ion-atom collision. The two velocity components \vec{v}_d and \vec{v}_{rf} of the ion's motion before the collision are used to construct the two velocities \vec{a} and \vec{b} , which determine the ion's final velocity \vec{v}'_d . These two constructed velocities are (exempt a prefactor) equivalent to the COM velocity (\vec{b}) and the ion's velocity in the COM frame (\vec{a}). After the collision the velocity in the COM frame is rotated according to the rotation matrix $\mathcal{R}(\theta_c, \phi_c)$. It should be noted that the two dimensional plane shown before and after the collision do not have to be the same, as $\mathcal{R}(\theta_c, \phi_c)$ is a three dimensional rotation.

These are implicit function of the ion's radial position r and the phase of the rf-field. Consequently, the initial velocities of ion (v_d) and atom ($u_{\text{eff}} = v_{\text{rf}}$) are fully characterized by r , $\phi_{\text{rf}} = \omega t$ and α . These parameters do not define the absolute orientation of the velocities in the lab frame but are sufficient to describe the elastic collision. Rearranging Eq. (22) to

$$\vec{v}'_d = \frac{m_a}{m_i + m_a} \left[\mathcal{R}(\theta_c, \phi_c) \underbrace{(\vec{v}_d - \vec{v}_{\text{rf}})}_{\vec{a}} + \underbrace{\xi^{-1} \vec{v}_d + \vec{v}_{\text{rf}}}_{\vec{b}} \right], \quad (30)$$

results in the combined velocities \vec{a} and \vec{b} . The velocity \vec{a} is proportional to the ion's velocity in the COM frame and the velocity \vec{b} is proportional to the COM velocity. Fig. 10 shows the relevant velocities before and after the collision. Using the combined velocities \vec{a} , \vec{b} and the angles α and β the absolute velocity of the ion's macromotion after the collision can be written as

$$v'_d = \frac{m_a}{m_i + m_a} \sqrt{a^2 + b^2 + 2ab \sin \beta}, \quad (31)$$

with $a = (v_{\text{rf}}^2 / \xi^2 + v_d^2 + 2v_{\text{rf}}v_d \sin(\alpha) / \xi)^{1/2}$,
 $b = (v_{\text{rf}}^2 + v_d^2 - 2v_{\text{rf}}v_d \sin(\pi - \alpha))^{1/2}$.

Finally, replacing the initial micro- and macromotion velocities with the expressions from Eq. (28) and (29), results in an expression which is fully defined by the seven parameters E_{tot} , n , ζ , r , ϕ_{rf} , α and β . Based on this expression one can calculate the probability distribution for a relative energy change $\Delta E_{\text{tot}}/E_{\text{tot}}$ caused by a single elastic collision

$$p(\Delta E_i/E_i) = \int \left[\left(\frac{v'_d(E_{\text{tot}}, n, \zeta, r, \phi_{\text{rf}}, \alpha, \beta)}{v_d(E_{\text{tot}}, n, r)} \right)^2 - 1 \right] \times \\ \times p(r, \phi_{\text{rf}}, \alpha, \beta) dr d\phi_{\text{rf}} d\alpha d\beta, \quad (32)$$

with $p(r, \phi_{\text{rf}}, \alpha, \beta)$ being the probability density of the four parameters $r, \phi_{\text{rf}}, \alpha, \beta$, while the other three parameters n, ζ and E_{tot} are kept constant.

Solving the integral in Eq. (32) requires knowledge about the distribution $p(r, \phi_{\text{rf}}, \alpha, \beta)$. In general, collisions between ions and atoms can be treated by a partial wave expansion leading to a total elastic cross section of $\sigma \propto E_{\text{col}}^{-1/3}$ [93], with E_{col} being the collision energy. This includes collisions at large impact parameters resulting in a forward scattering peak with small momentum transfer. It has been shown in previous work that using the simpler Langevin model [94, 95] yields the same equilibrium state [81] and relaxation rates [83] as the full partial wave expansion.

In the Langevin model the cross section scales as $\sigma \propto E_{\text{col}}^{-1/2}$ resulting in a velocity independent scattering rate. This means that the scattering rate does not depend on the micromotion velocity and thus the phase of the rf-field Φ_{rf} . The Langevin model also predicts an isotropic scattering angle distribution $p(\theta_c, \phi_c) \propto \sin \theta_c$ (Jacobian matrix element) which in turn results in uncorrelated angles α and β . This is in strong contrast to elastic neutral-neutral or ion-ion collisions where the rotation matrix $\mathcal{R}(\theta_c, \phi_c)$ usually directly depends on the initial conditions, i.e. there exists a correlation between the angles α and β . Such systems are usually better described in terms of an impact parameter. For ion-neutral collisions however the scattering angle is completely uncoupled from the initial velocities and the impact parameter.

We further assume that also the collision radius is not correlated with any of the other parameters. In this case, the probability density factorizes to $p(r, \phi_{\text{rf}}, \alpha, \beta) = p(r)p(\phi_{\text{rf}})p(\alpha)p(\beta)$. The total probability density is composed of

- the radial probability distribution $p(r)$ which depends on the ion's angular momentum and energy in radial direction (Eq. (17)).
- The constant rf-phase distribution (see above) $p(\phi_{\text{rf}}) = 1/(2\pi)$.
- The distribution of collision angles $p(\alpha)$. Assuming that the ion's macromotion has a random orientation in space, the angle α is distributed as $p(\alpha) = \frac{1}{2} \sin \alpha$ with $0 \leq \alpha \leq \pi$.

- The distribution of angles β between the COM velocity \vec{b} and the ion's final velocity in the COM frame \vec{a}' . Due to the isotropic scattering angle distribution, the velocity $\vec{a}' = \mathcal{R}(\theta_c, \phi_c)\vec{a}$ has a random direction. Consequently, there is no correlation between \vec{a}' and \vec{b} , which corresponds to a probability $p(\beta) = \frac{1}{2} \sin \beta$ with $0 \leq \beta \leq \pi$.

With these dependences a probability distribution $p_r(\Delta E_{\text{tot}}/E_{\text{tot}})$ can be calculated according to Eq. (32) with the last free parameter being the radial position of the collision. The normalized distribution function $p_r(\Delta E_i/E_i)$ gives the probability for a collision at radius r to result in a relative energy change of $\Delta E_i/E_i$. In combination with the probability distribution $p_i(r)$ to find the ion at radius r (Eq. (17)), this yields the total probability distribution

$$p(\Delta E_i/E_i) = \int p_r(\Delta E_i/E_i)p_i(r) dr \quad (33)$$

for an energy change of $\Delta E_i/E_i$ to occur.

Fig. 11 shows the probability distributions $p_r(\Delta E_i/E_i)$. The dependences on the multipole order n is eliminated by scaling the collision radius as $(r/r_{\text{lim}})^{n-1}$. Besides the scaled collision radius, the only free parameter left is therefore the mass ratio ζ . The left panels in Fig. 11 show the resulting distributions for five different mass ratios, the right panels show the result of independently performed numerical simulations which show good agreement.

As expected, collisions close to the trap center always reduce the ion's energy whereas collisions close to r_{max} increase the energy, with the two regimes being separated by the critical cooling radius r_c (Eq. (25)) indicated by the red dashed line. As expected, the overall energy change also shows a pronounced dependence on the multipole order n and the mass ratio ζ . On the one hand, with growing multipole order the volume of efficient cooling at small radii is extended as the radial dependence of $p_r(\Delta E_i/E_i)$ scales as $(r/r_{\text{max}})^{n-1}$. On the other hand, the micromotion induced heating at large radii is amplified with larger atom-to-ion mass ratio, as the velocity of the micromotion $v_{\text{rf}} \propto 1/m_i$, now being assigned to the atom of mass m_a , leads to the prefactor ζ in the effective buffer gas energy (see Eq. (23)). Hence, at large mass ratios and small multipole orders, the ion essentially gains energy through collisions, whereas at low mass ratios and large multipole orders the energy is primarily reduced.

2.3 ION'S ENERGY DISTRIBUTION

In order to numerically determine the ion's equilibrium energy distribution, the energy E_i has to be tracked over the course of many collisions. In previous investigations, this was done using the solutions of the Mathieu differential equations [80, 81, 83] or full trajectory

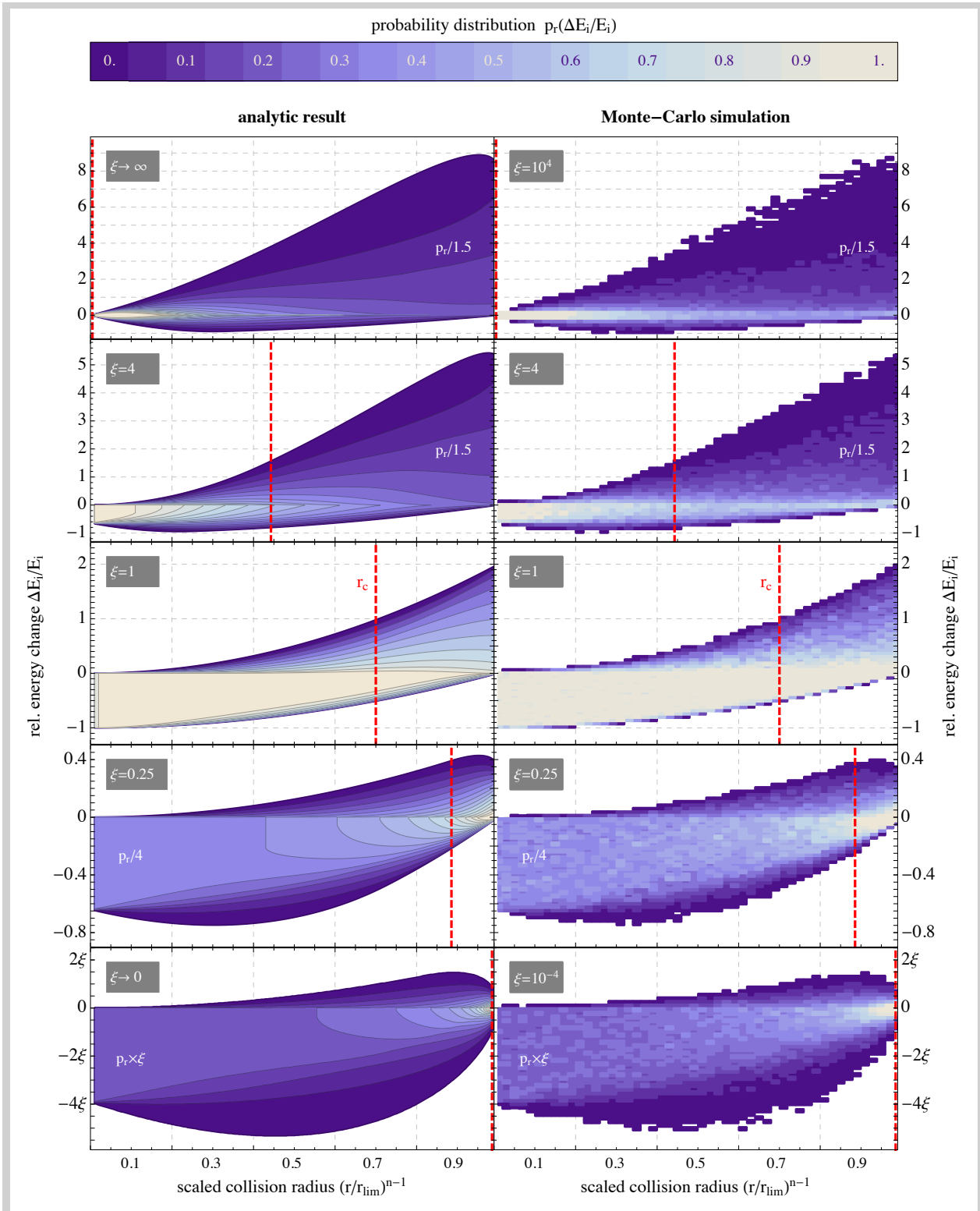


Figure 11: Probability distributions of a relative energy change $\Delta E_i/E_i$ in an elastic ion-neutral collision for an ion at energy E_i as a function of the normalized collision radius r/r_{lim} . The buffer gas is assumed to be at rest (temperature $T_a = 0$). Left graphs show the analytic distribution, right graphs show the result of independently performed numerical simulations. The mass ratios are indicated in the graphs. The color code provides the normalized probability function $p_r(\Delta E_i/E_i)$ of the energy change at a given radius r . The distributions (except for $\xi = 1$) were scaled by constant factors which are indicated in the graphs. Indicated by the red dashed line is the critical cooling radius (Eq. (25)) given by the condition that average energy transfer $\langle \Delta E_i/E_i \rangle$ becomes zero.

calculations [79, 38, 66]. The first approach has the disadvantage, that it is limited to Paul traps and homogeneous buffer gases. The second approach lifts these limitations as the full trajectory calculation can be applied to traps of any multipole order and evaluating the collision probability $p(t)dt$ for every infinitesimal time step dt allows to simulate arbitrary buffer gas configurations. However, full trajectory calculations result in very long computation times, as the time between consecutive collisions is usually much longer than the time scales set by micro- and macromotion. In the following we develop a general method, which can be used for any multipole order and buffer gas configuration, without the necessity to calculate the ion's full trajectory.

2.3.1 Numerical model

Our model is based on three main simplifying assumptions. First, we use the adiabatic approximation to describe the motion of the ion. This limits our model to small stability parameters η (see Eq. (7)). We find satisfactory agreement with the ion's exact trajectory for $\eta < 0.1$, which is also the regime most experiments are operated in. Second, for the energy regime discussed here, the classical Langevin model [94, 95] is used, which yields a velocity-independent scattering probability for ion-atom collisions [81, 83]. This is valid, as long as a large number of partial waves contribute to the scattering process and quantum interferences of scattering amplitudes can be neglected. Third, we assume that the time between consecutive collisions is long compared to the period of the macromotion, allowing one to apply a separation of time scales. As long as the ion undergoes many oscillations in the effective potential (macromotion) between every two consecutive collisions, the ion's exact trajectory can be substituted by a radial density distribution $p_i(r)$. The density distribution is independent of the two other cylindrical coordinates z and ϕ , as we assume perfect axial symmetry.

Based on these three simplifications, the probability of an collision to occur in the interval dr around a radial position r is given by the relative overlap of the buffer gas and ion distributions

$$p_{\text{coll}}(r) dr = \rho_a(r)p_i(r) dr, \quad (34)$$

with $\rho_a(r)$ being the normalized density distribution of the buffer gas.

In the simulation, the ion's radial and axial energy as well as its angular momentum are computed and stored after every collision. As initial conditions we typically use $E_r = k_B T_a$, $E_z = k_B T_a/2$ and $L = 0$. For every collision we then pick the following set of parameters:

- **Rf-phase** - the phase of the rf-field ϕ_{rf} is randomly chosen between 0 and 2π .

- **Atom velocity** - all three cartesian coordinates of the atom's velocity vector are chosen with a normal distribution with standard deviation $\sqrt{k_B T_a / m_a}$.
- **Collision radius** - the radial position of the collision r_{coll} is chosen according to $p_{\text{coll}}(r)$ which is determined by L and E_r (see Eq. (34)). For large radial ion energies $p_{\text{coll}}(r)$ can have a long tail of near zero values, in which case we use an upper boundary of $r_{\text{coll}} < 5\sigma_a$.
- **Incident angle** - the random incident angle θ_i between the ion's macromotion and the atom's effective velocity determines the COM velocity. The angle is picked according to the Jakobian determinant $p(\theta_i) = \sin \theta_i$.
- **Scattering angles** - using the Langevin model, the scattering angle in the center-of-mass frame is distributed isotropically. This is achieved by randomly choosing an azimuthal angle ϕ_c between zero and 2π and a polar angle θ_c between zero and π taking into account the Jakobian determinant $p(\theta_c) = \sin \theta_c$.

Based on these parameters the ions micro- and macromotion velocities are calculated and using Eq. (22), the ion's macromotion after the collision is obtained. The new macromotion velocity together with the collision radius defines the ion's radial and axial energy as well as its angular momentum after the collision based on which the next collision parameters can be calculated. The average time of free motion before the next collision occurs, is given by the inverse of the overlap of atom and ion distribution

$$\tau = \tau_{\text{coll}} / \left(\int \rho_a(r) p_i(r) dr \right). \quad (35)$$

where τ_{coll} is the collision time as derived from the Langevin cross section. After typically performing 10^6 such collisions, the distributions have converged. All energy values are weighted with the corresponding τ and binned, resulting in the ion's steady-state energy distribution.

2.3.2 Equilibrium regimes

The ion's final energy distribution depends on the one hand on the spatial distribution, temperature and mass of the buffer gas atoms and on the other hand on the trap parameters, namely the multipole order n and the stability parameter η . Fig. 12 shows some exemplary energy distributions $P(E_i)$ for different mass ratios in a Paul trap.

These energy distributions can be separated into different regimes which are characterized by the degree to which the effective buffer gas distribution in Eq. (24) matches a thermal distribution ("thermalicity").

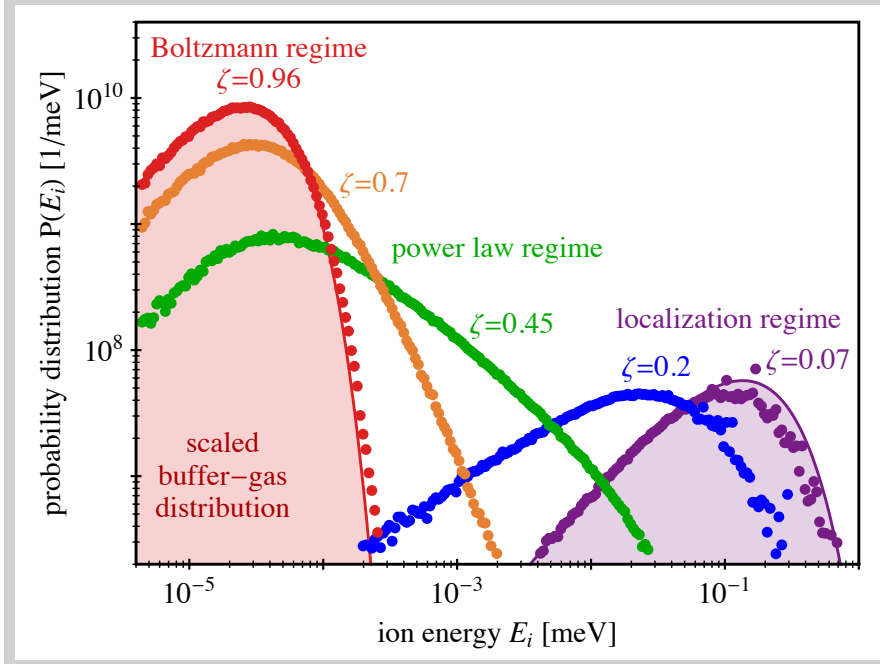


Figure 12: Normalized equilibrium energy distributions for different thermality parameters ζ in a Paul trap ($n = 2$). The buffer gas cloud distribution is given by a Gaussian of size $\sigma_a = R_0/100$ and temperature of $T_a = 200\mu\text{K}$. Also shown is the energy distribution in the Boltzmann regime (red curve) and an energy distribution in the localization regime for $\zeta = 34$ (purple curve), according to Eq. (38) and (43).

The atoms effective energy consists of two parts, the micromotion induced energy $\zeta V_{\text{eff}}(r)$ and the thermal energy of the buffer gas $\frac{3}{2}k_B T_a$. So far we have only considered the radial dependence of the effective energy which resulted in the critical cooling radius (Eq. (25)). Additionally to this spatial dependence, the effective energy implicitly depends on the ion's energy E_i . This dependence can be expressed by replacing $V_{\text{eff}}(r)$ by its average value given by the virial theorem, resulting in an effective energy of

$$\langle E_a \rangle = \frac{2\zeta}{3n-1} E_i + \frac{3}{2} k_B T_a. \quad (36)$$

A parameter ζ which characterizes the thermality is obtained by comparing the atoms' thermal energy $\frac{3}{2}k_B T_a$ to their total effective energy $\langle E_a \rangle$, assuming that the ion has an energy of $E_i = \frac{3}{2}k_B T_a$,

$$\zeta = \frac{3n-1}{3n-1+2\zeta}. \quad (37)$$

This parameter ranges from zero (distributions determined by the buffer gas' potential energy) to unity (distributions determined by the buffer gas' temperature). For $\zeta \approx 1$, the atom's effective energy distribution resembles a pure thermal distribution (Boltzmann regime).

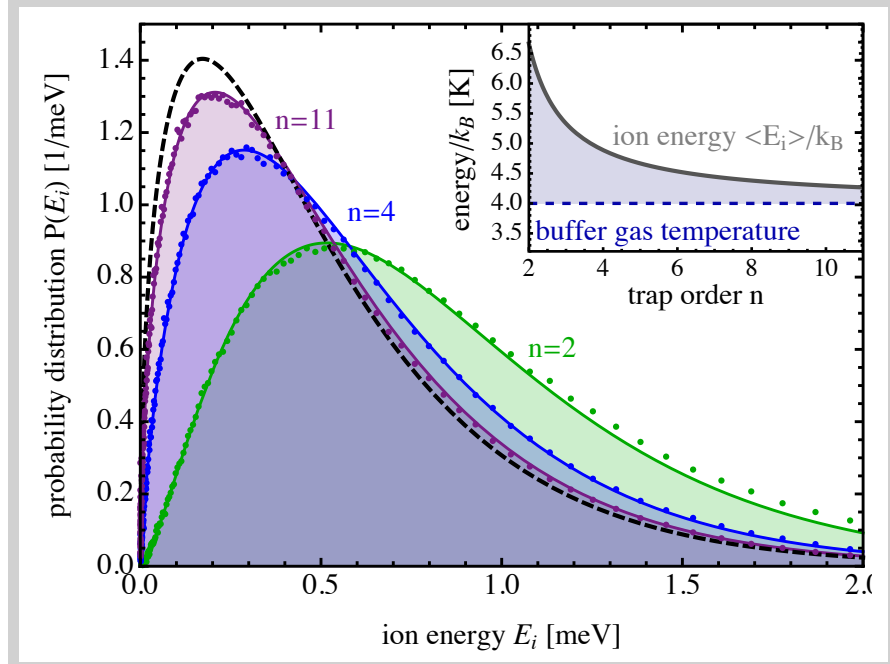


Figure 13: Ion's energy distribution in the Boltzmann regime. The difference between the energy distribution of the ion and the one of the buffer gas (dashed line) is caused by the effective potential, confining the ion in the trap. Depending on the multipole order, the influence of the effective potential differs. The inset shows the ion's mean energy as a function of the trap order. The mean energy is largest for an ion inside a Paul trap and converges towards the mean energy of the buffer gas for large multipole orders.

With decreasing ζ , the contribution of the micromotion induced energy becomes relevant and the ion's energy distribution exhibits growing power laws towards higher energies (power law regime). Finally for ζ approaching zero, stable energy distributions can only be realized using a localized buffer gas (localization regime). These three regimes will be discussed in detail in the following.

2.3.3 Boltzmann regime

For $\zeta \approx 1$ (which corresponds to $\xi \ll 1$) the ion thermalizes to the buffer gas temperature as the atoms' effective energy is dominated by the thermal energy (see Eq. (36)).

Fig. 13 shows the resulting energy distributions for three different multipole orders with $\zeta = 0.95$ as well as the energy distribution of buffer gas atoms (dashed black line). The deviation of the ion's energy distributions from the three dimensional Maxwell Boltzmann distribution of the buffer gas atoms is caused by the effective potential.

By applying the virial theorem, the pole order dependent energy distribution in the Boltzmann regime is given by

$$P_{\text{br}}(E_i) \propto E_i^{\frac{1}{2} + \frac{1}{n-1}} \exp(-E_i/k_B T_a). \quad (38)$$

This analytic expression matches well to the results of our numeric simulations. For large multipole orders, the distribution converges towards a Maxwell Boltzmann distribution, whereas, for a Paul trap the ion's mean energy exceeds the mean energy of the buffer gas by a factor of $3/2$ (see inset of Fig. 13).

The ion's spatial distribution is obtained by summing over all radial probability distributions $p_i(r)$ (Eq. (17)) weighted with the average time the ion spends on this energy shell (Eq. (35)). The resulting spatial distributions are well described by

$$p_i(r) \propto \exp\left(-\frac{V_{\text{eff}}(r)}{k_B T_a}\right). \quad (39)$$

For a Paul trap this corresponds to a Gaussian density distribution, converging towards a boxlike density distribution for $n \rightarrow \infty$.

2.3.4 Power-law regime

With decreasing ζ , the contribution of the micromotion to the atoms effective energy (Eq. (36)) becomes significant. It is important to notice that there is a fundamental difference between the two contributions to the atoms effective energy. On the one hand, the thermal energy has a fixed value and for large ion energies ($E_i \gg \frac{3}{2}k_B T_a$) the probability for the ion to gain energy from the thermal motion of the buffer gas decreases exponentially. On the other hand, the micromotion induced energy is directly proportional to the ions energy. Consequently, even at very large energies $E_i \gg \frac{3}{2}k_B T_a$, the probability for the ion to gain energy (as shown in Fig. 11) from the micromotion remains constant. As a result, the ion can gain a large fraction (or even multiples) of its energy during every collision which can cause a temporary exponential growth of the ion's energy, if a series of consecutive heating collisions occurs. It is well known, that such kind of multiplicative processes lead to the emergence of power law distributions, also known as heavy sided or levy flight distributions [96, 97].

Fig. 14 (a) shows the resulting energy distributions for different mass ratios in a Paul trap. The energy distributions in the power-law regime $P_{\text{plr}}(E_i)$ are well described by Tsallis functions (solid lines) given by [98]

$$P_{\text{plr}}(E_i) \propto \frac{E_i^{\frac{1}{2} + \frac{1}{n-1}}}{[1 + a E_i / (k_B T_a)]^b}, \quad (40)$$

which were fitted to the numerical data using the two free parameters a and b . These Tsallis functions are characterized by a power law towards

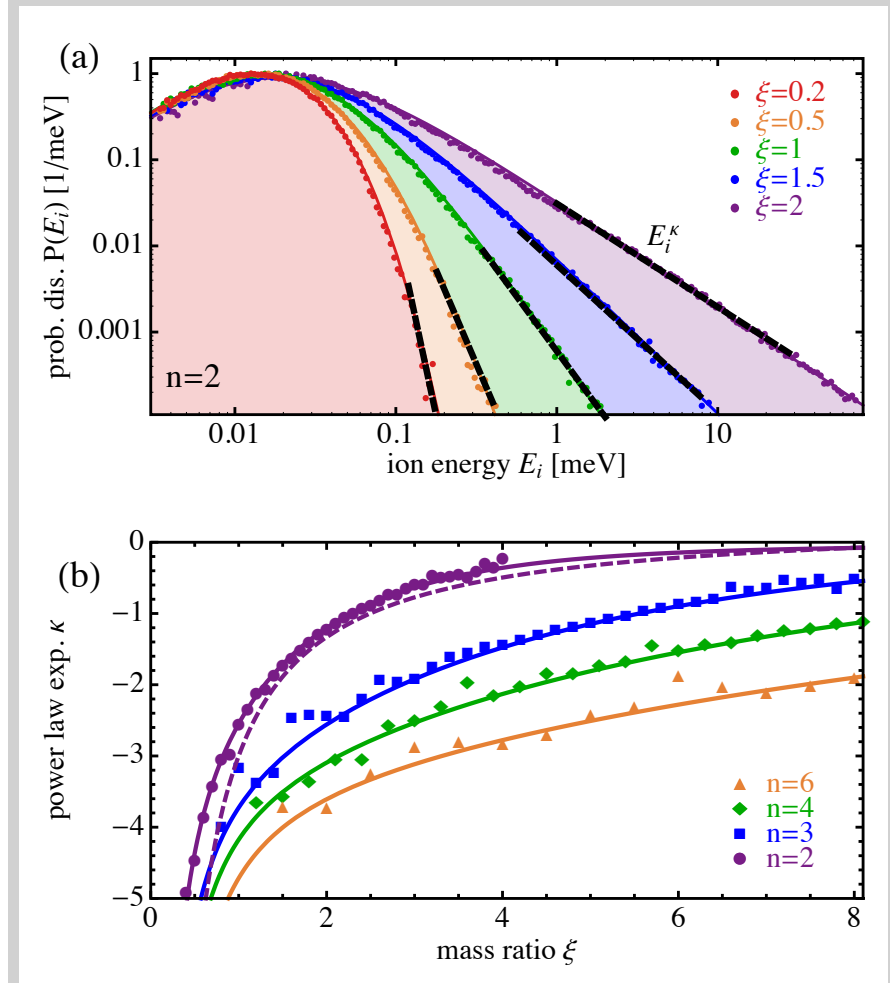


Figure 14: Energy distributions in the power-law regime. (a) Shown are five distributions corresponding to five different mass ratios. With increasing mass ratio the energy distribution exhibits a growing power law towards higher energies. The solid lines correspond to Tsallis functions (Eq. (40)) which were fitted to the numerical data. (b) Mass ratio dependence of the power law exponent κ for four different multipole orders. For a fixed mass ratio, the power law exponent is always largest for an ion inside Paul trap and monotonically decreases with increasing multipole order. The solid lines correspond to Eq. 41, the dashed line shows the analytic result of Chen *et al.* [83] for a Paul trap, which shows reasonable agreement with our numeric results.

low as well as large energies, centered around the characteristic energy scale $k_B T_a$. The power law towards low energies is the same as in the Boltzmann regime (Eq. (38)). The power law E^κ towards higher energies exhibits a steadily rising power law exponent κ for increasing mass ratios, as the impact of micromotion induced heating grows. Fig. 14 (b) shows the mass ratio dependence of κ for four different

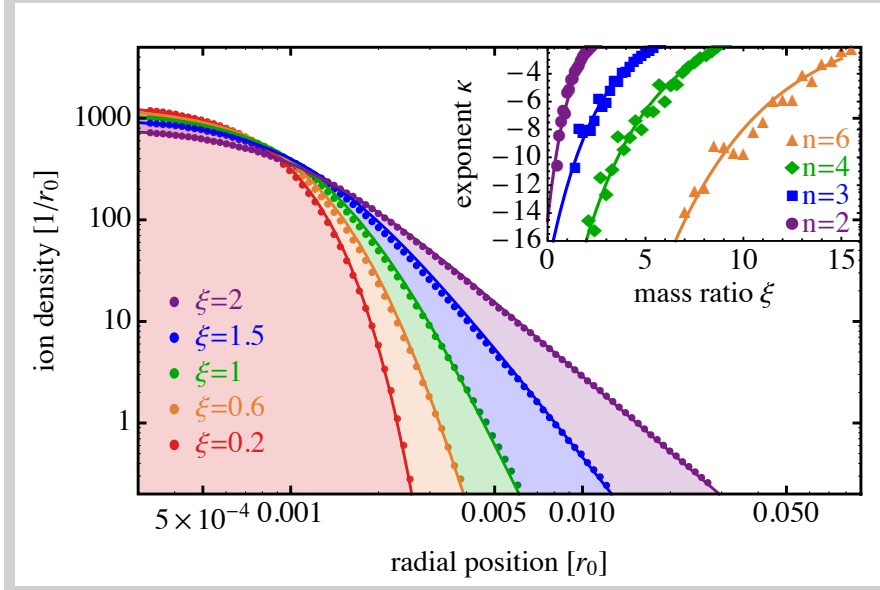


Figure 15: Spatial distribution in the power-law regime. Shown are five distributions for an ion inside a Paul trap, corresponding to different mass ratios. For small mass ratios, the spatial distribution corresponds to the one in the Boltzmann regime (Eq. (39)). For larger mass ratios, the distributions exhibit a power law towards large radii, much like the energy distributions. The inset shows the mass ratio dependence of the power-law exponent for different multipole orders. The solid lines are a guide to the eye.

multipole orders. In lack of an analytical model, the mass ratios is well described by

$$\kappa \approx A \exp[-\zeta/B] - C\zeta^{-D} \quad (\text{for } \kappa \lesssim -0.5), \quad (41)$$

with the four fit parameters $A = 3.5$, $B = 2.6n - 3.8$, $C = n/6 + 0.5$ and $D = 1.2$. If the exponent is close to zero the ion's energy diverges very fast, making it impossible to calculate a steady state energy distribution. Already for $\kappa \geq -2$ the ion's mean energy diverges and the ion is no longer confined by the trap. This condition is commonly used to define the critical mass ratio ζ_{crit} [80, 83]. From the simulations we obtain $\zeta_{\text{crit}} \approx 1.4(n - 1)$, which is in good agreement with the analytical result derived before (Eq. (27)). The critical mass ratio corresponds to a thermalicity parameter of $\zeta \approx 0.6$ for a Paul trap approaching $\zeta \approx 0.5$ with increasing multipole order.

Fig. 15 shows the corresponding spatial distributions for a Paul trap, which show a similar power law behavior [80]. The inset shows the exponent of the power law for four different multipole orders. An ion inside a Paul trap always exhibits the largest power law exponent, which steadily decreases with increasing multipole order.

Another important quantity characterizing the sympathetic cooling process is the thermalization rate. On the one hand, the micromotion induced heating is strongly reduced for small mass ratios. On the other

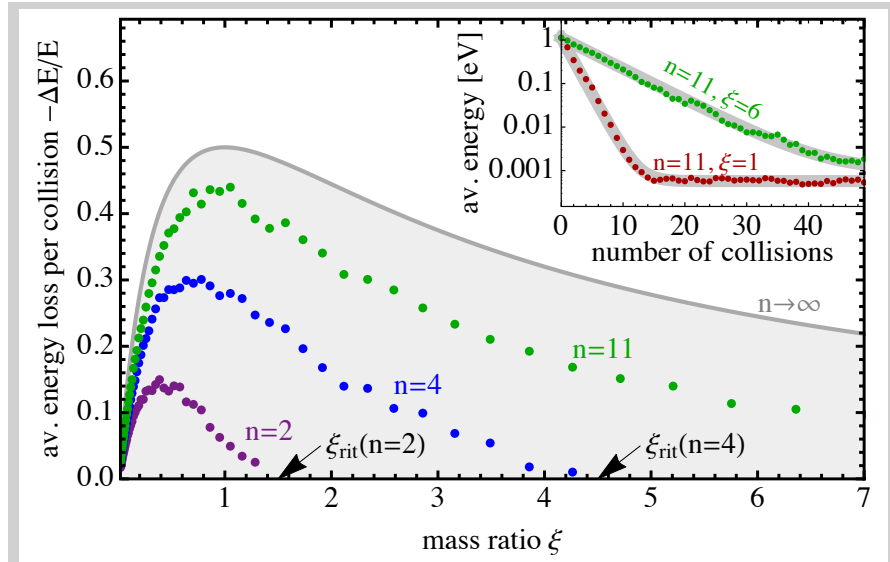


Figure 16: Thermalization rates in different rf traps. Shown is the average energy loss per collision for different mass ratios and multipole orders. The gray curve shows the average energy loss in absence of the rf trap which is equivalent to a trap with an infinite multipole order. The mass ratio where the average energy loss turns into an energy gain, corresponds to the critical mass ratio. The inset shows two exemplary energy traces. The average energy loss was extracted from the exponential decay at the beginning of the trace where the ion's energy exceeds the one of the buffer gas.

hand, small mass ratios greatly reduce the average energy transfer per collision. Fig. 16 shows the resulting average energy loss per collision for different trap orders. The solid line corresponds to the thermalization of an untrapped ion. This case represents an upper boundary for the thermalization rate as the presence of rf heating inside the multipole trap results in lower thermalization rates. In a Paul trap this effect leads to a 3-fold decrease of the maximum cooling rate, which is reached for a mass ratio of $\xi \approx 1/2$. With growing multipole order, the thermalization rates become larger and the optimal mass ratio tends towards unity as in the case of a free particle.

2.3.5 Localization regime

So far we have focused the discussion on homogeneous spatial distributions of buffer gas filling the entire volume of space. In this scenario, one finds an upper limit for the atom-to-ion mass ratio, beyond which the ion's are mainly heated until they are expelled from the trap. This limitation can be overcome by localizing the buffer gas to the center of the trap. We have seen in the previous section, that with decreasing

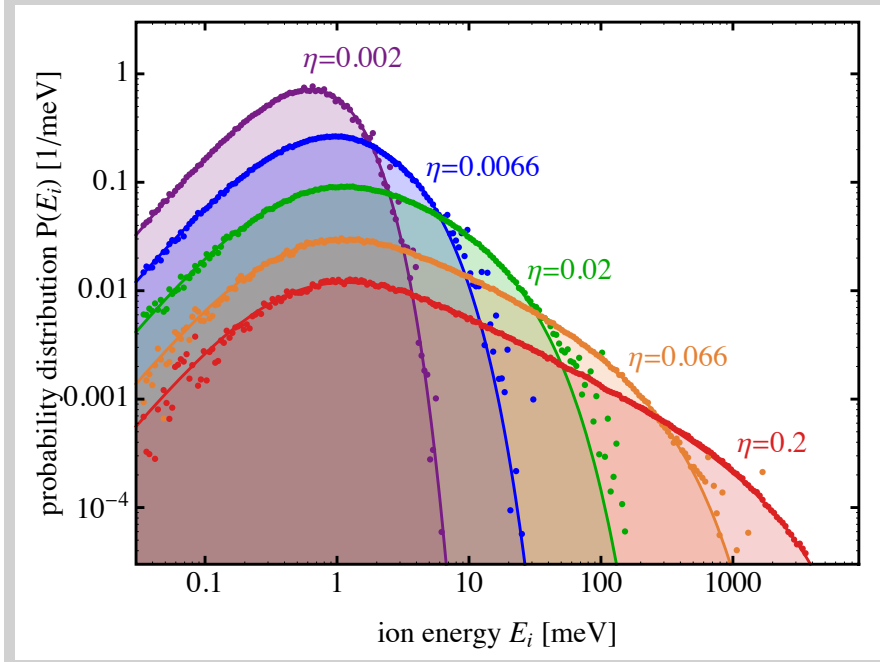


Figure 17: Ion's energy distribution for a localized buffer gas in a Paul trap. The buffer gas has a Gaussian density distribution with standard deviation $\sigma_a = r_0/10$ and an atom-to-ion mass ratio of $\zeta = 3$. The five graphs correspond to five different multipole stability parameters (Eq. (7)).

thermalicity parameter, the energy distributions exhibit an increasing power-law tail towards higher energies. At large energies E_i the probability for a collision to result in a gain of energy (Fig. 11) increases with the mass ratio. As the relative energy transfer has a distinct radial dependence, this can be overcome by localizing the buffer gas to the trap center. As soon as r_{\max} exceeds the extension of the buffer gas, collisions are restricted to small radii r/r_{\lim} .

We find that the resulting energy distributions are bound by an additional exponential decay. The energy scale of this exponential decay is well estimated by the atoms total effective energy $E_{a,\text{tot}}$ accessible for collisions with the ion, as given by integrating $\langle E_a \rangle$ (Eq. 23) over the entire buffer gas cloud. For a Gaussian shaped buffer gas cloud with standard deviation σ_a this results in an energy of

$$E_{a,\text{tot}} = \frac{3}{2}k_B T_a + 2^{n-1}(n-1)! \zeta V_{\text{eff}}(\sigma_a). \quad (42)$$

Fig. 17 shows the resulting energy distributions for different stability parameters η . With decreasing stability parameter, the energy distribution is bound towards lower energies. Small stability parameters correspond to a shallow effective potential meaning that the ion probes a volume of the same size as the buffer gas cloud already at relatively low energies E_i . In contrast, for large η , the ion is strongly confined to the trap center and only at very large energies does the

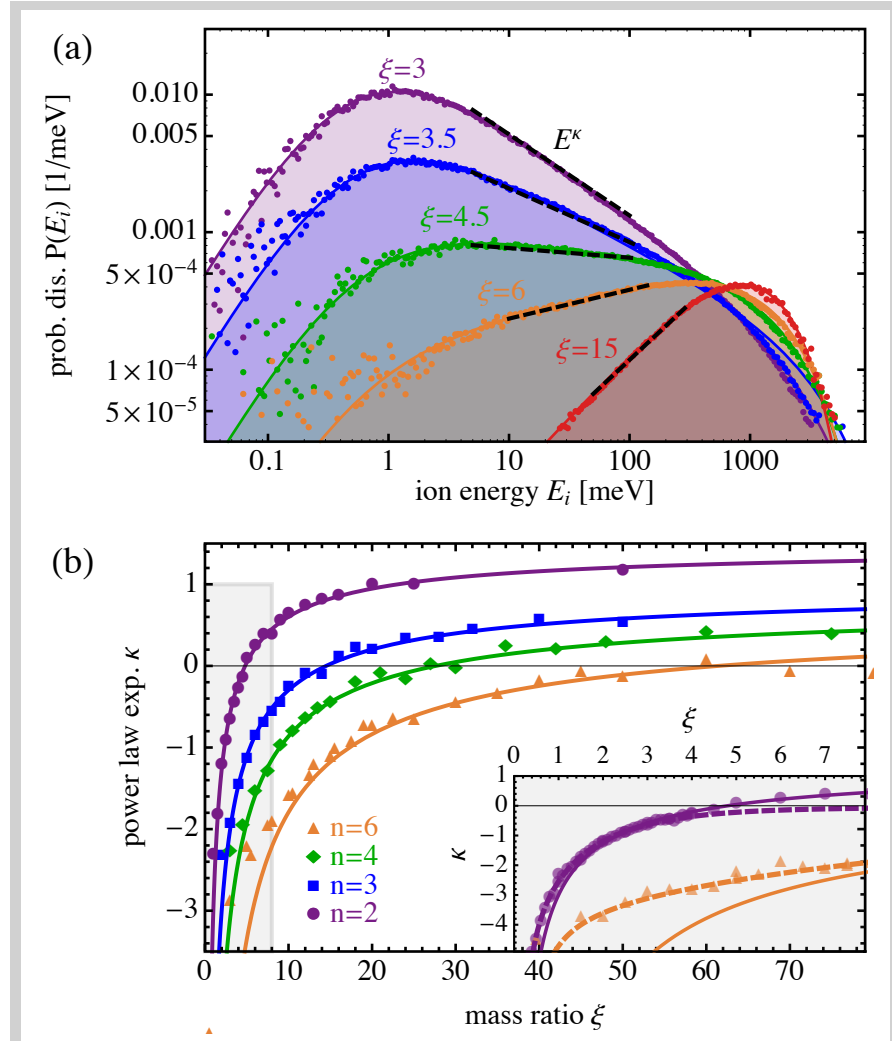


Figure 18: Energy distributions in the localization regime. (a) Ion's energy distribution for different mass ratios in a Paul trap. The energy scale $E_{a,tot}$ was kept constant at 1eV. (b) Power law exponents for different multipole orders as indicated by the dashed lines in the upper graph. Shown are the power law exponents as a function of the mass ratio. The solid curves correspond to the analytic expression given in Eq. (44) which show good agreement with the numerical data for large mass ratios. For small mass ratios however, the exponent is better described by Eq. (41) as indicated by the close up into the area marked in gray. Shown is the numerical data for $n = 2, 6$ and the corresponding analytic expressions from Eq. (44) (solid lines) and Eq. (41) (dashed lines).

ion experience the localization of the buffer gas. Instead of varying the stability parameter η , which can be done by tuning the trap's rf voltage, it is also possible to tune the size of the buffer gas cloud. Neglecting the contribution of the thermal energy, the atoms total effective energy is proportional to $E_{a,tot} \propto \sigma_a^{n-2} U^2$.

The energy distribution in the localization regime is given by

$$P_{lr}(E_i) \propto P_{plr}(E_i) \exp \left[- \left(\frac{E_i}{\gamma E_{a,\text{tot}}} \right)^{1/(n-1)} \right], \quad (43)$$

with γ being a free parameter which is on the order of one.

The emergence of the additional exponential decay towards large energies also allows the use of heavy buffer gases with $\zeta \gg \zeta_{\text{crit}}$. Fig. 18 shows the energy distributions for different mass ratios with the energy scale $E_{a,\text{tot}}$ kept constant. For small mass ratios, the distributions are equivalent to the ones shown in Fig. 17, with the power law turning into an exponential decay around $E_{a,\text{tot}}$. With increasing mass ratio, the power law exponent keeps growing until for $\zeta \approx 5$ a plateau-like distribution is reached which has a constant probability all the way from the thermal energy of the buffer gas up to the energy $E_{a,\text{tot}}$. For even larger mass ratio, the power law exponent becomes positive, eventually making the thermal energy irrelevant and the energy distribution is fully characterized by $E_{a,\text{tot}}$.

Fig. 18 shows the power law exponent κ as a function of the mass ratio, as obtained from our numerical simulations. For large mass ratios, the exponent is well described by

$$\kappa \approx A' - C' \zeta^{-D'} \quad (\text{for } \kappa \gtrsim -0.5), \quad (44)$$

with the fitting parameters $A' = 0.5 + (n-1)^{-1}$, $C' = 2n + 0.5$ and $D' = 0.7$. For very large mass ratios the power law converges to the same one found in the Boltzmann regime. Fig. 18 (b) shows the mass ratio dependence of κ , with the inset showing a close up for small mass ratios where Eq. (44) (solid lines) loses its validity and Eq. (41) (dashed lines) provides the correct mass ratio dependence. The transition between the two dependencies happens around $\kappa \approx -0.5$.

2.3.6 Forced sympathetic cooling

The idea behind forced sympathetic cooling (FSC) is to tune the ion's energy distribution by changing the energy scale $E_{a,\text{tot}} \propto \sigma_a^{2n-2} U^2$. FSC does not work for homogeneous buffer gas distributions, as it is the localization of the buffer gas which introduces the energy scale $E_{a,\text{tot}}$. In the three regimes discussed above, FSC has different effects on the ion's energy distribution. In the Boltzmann regime, the impact of FSC is very limited as the characteristic energy scale of the ion's energy distribution is set by the thermal energy of the buffer gas. Nevertheless, if the energy scale $E_{a,\text{tot}}$ is chosen smaller than the thermal energy of the buffer gas, small collision radii r/r_{max} will be favored. Eventually, for $E_{a,\text{tot}} \ll k_B T_a$ the ion's energy distributions independently of the mass ratio, will exactly equal the one of the buffer gas (dashed line in Fig. 13). For larger mass ratios, the localization leads to the additional

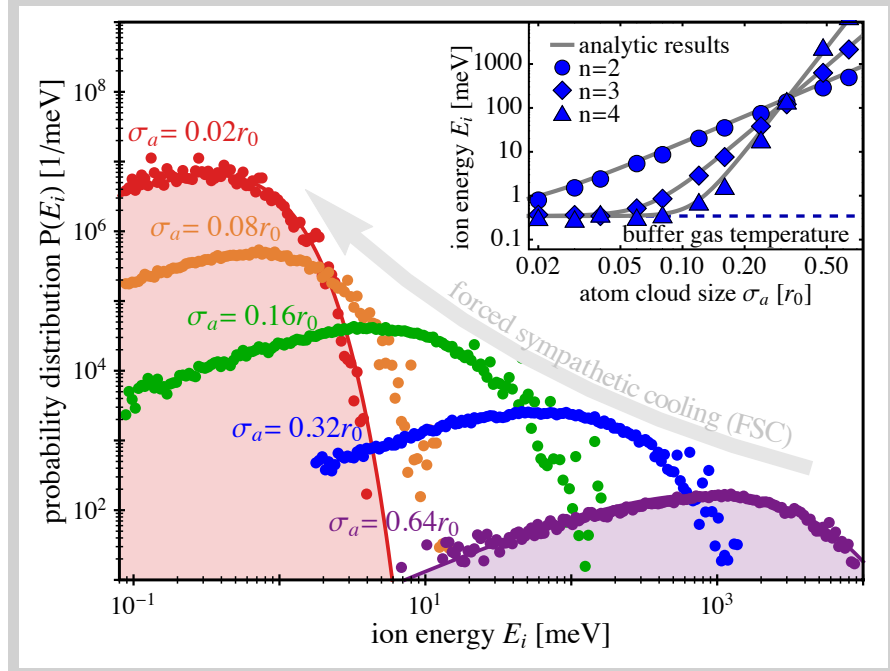


Figure 19: Forced Sympathetic Cooling. Shown are five energy distributions in an octupole trap ($n = 4$) for different buffer gas sizes. The buffer gas has a temperature of $T_a = 4\text{K}$ and $\zeta = 30$. The two curves correspond to the analytic expressions found in the text for $\sigma_a = 0.02$ and 0.64 . The inset shows the ion's mean energy and the effective buffer gas energy (Eq. (42)) as a function of the buffer gas size for three different trap orders. Both energies are in good agreement.

exponential decay towards higher energies as discussed in the context of Fig. 17. In this case, FSC can be used to substantially reduce the ion's mean energy as illustrated in Fig. 17 for $\zeta = 3$.

The largest effect of FSC is achieved for very large mass ratios, where the energy distribution is dominated by the energy scale $E_{a,\text{tot}}$. In this case, the entire distribution can be shifted to smaller energies, not just the exponential cut off of the power law. This is illustrated in Fig. 19 which shows the ion's energy distribution for five different buffer gas sizes in an octupole trap ($n = 4$). In this case, reducing the buffer gas size by a factor of two leads to a reduction of the ion's mean energy by a factor of 64. This illustrates that especially in traps with high multipole orders, already small reductions of the buffer gas size can have a large impact on the ion's energy distribution. Adiabatically changing the size of the buffer gas or the rf voltage does not change the relative overlap of atom and ion distribution and thus the collision rate. The size of ion and atom cloud always maintains a fixed ratio.

HYBRID ATOM ION TRAP

This chapter summarizes the experimental setup of the HAITrap experiment. The experiment was planned and constructed in collaboration with the group of Roland Wester at the university of Innsbruck. Parts of the results presented here have already been published in form of a master [99] and a bachelor thesis [100]. A publication about the detuned saturation absorption imaging presented in the last section is in preparation. The ion trap itself has already been used in previous experiments, details of which can be found in two publications [101, 102]. The main vacuum chamber and the laser system have been adapted from a previous setup in our group [103].

The hybrid atom ion trap (HAITrap) combines a radio frequency trap for the ions with a Dark Spontaneous Force Optical Trap (Dark SPOT) for rubidium atoms. A picture of the trap is shown in Fig. 20. The trap is designed in a way, that ions and atoms can be trapped simultaneously within the same trapping volume. Therefore, the radio frequency trap consists of thin wires rather than solid rods granting sufficient optical access for the laser beams required to cool and trap the atoms.

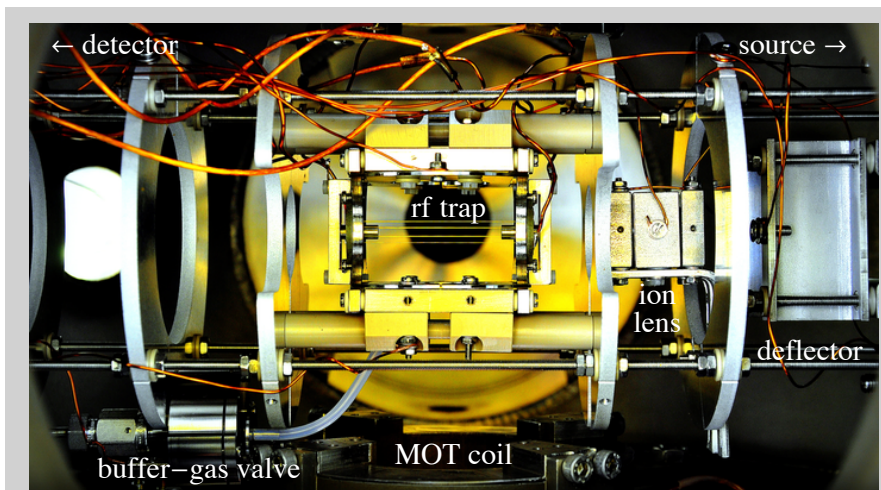


Figure 20: Picture of the HAITrap. The ion trap consists of thin gold-coated molybdenum wires ($100\mu\text{m}$). Axial confinement is achieved by two hollow endcap electrodes. The magneto optical trap for the rubidium atoms is created by three counter-reflected laser beams two of which pass the trap under 45° in the horizontal plane and one in vertical direction.

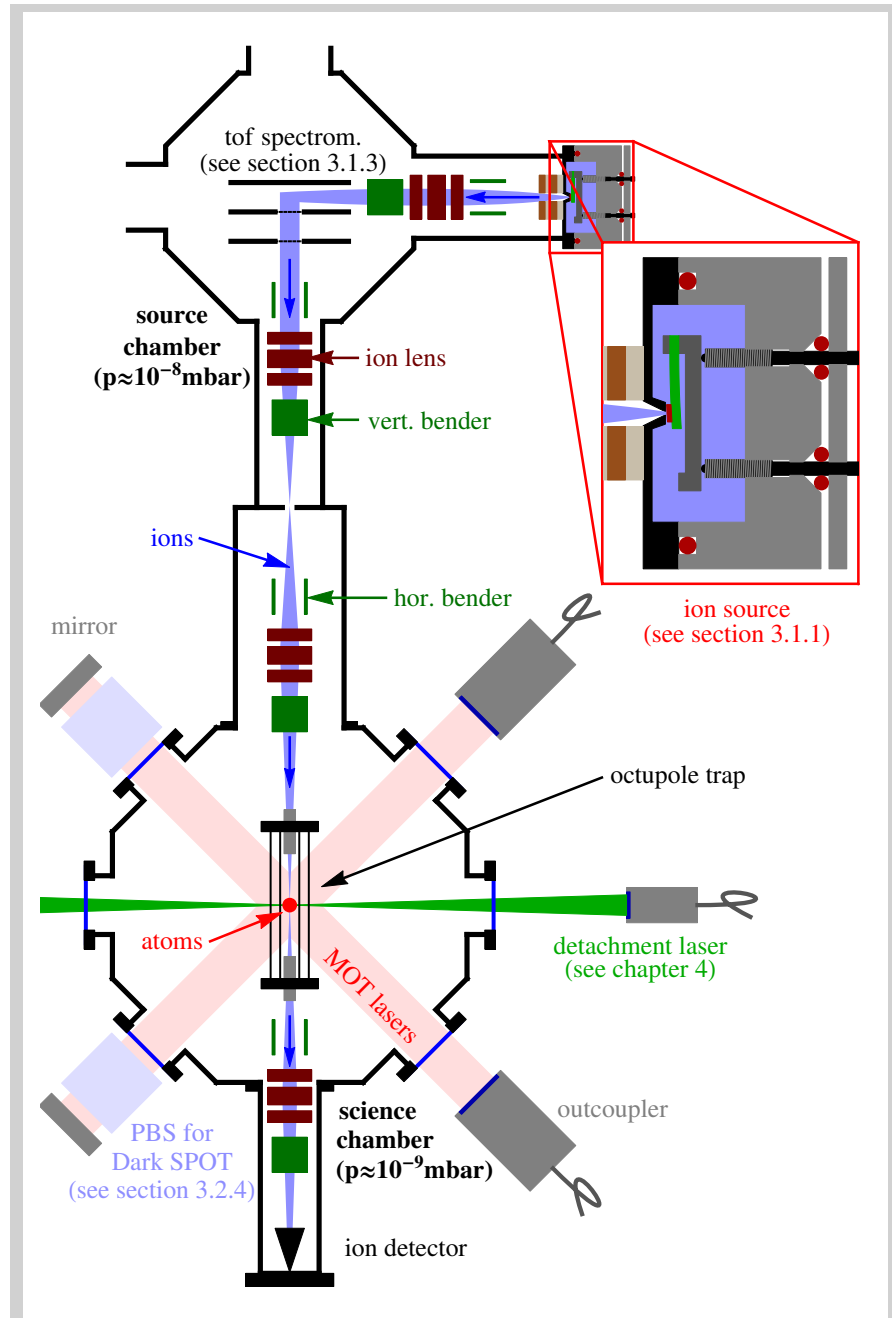


Figure 21: Schematic of the HAITrap setup. The setup is composed of two vacuum chambers which are connected via a differential pumping stage. In the source chamber, the ions are created in a plasma discharge source from where they are guided through the differential pumping into the science chamber where they are trapped in a radio frequency trap. At the center of the ion trap, also a magneto optical trap for rubidium atoms is available.

In the following we will discuss the different aspects of the setup in detail. Fig. 21 shows a schematic overview of the entire HAITrap setup. The entire setup is designed to provide favorable conditions for sympathetically cooling the trapped ions using laser-cooled atoms. In order to find the optimal system parameters we can use the findings of the previous chapter. This chapter is split into two main sections. In the first section the creation, trapping and detection of the ions are discussed. The second part of this chapter covers the trapping, cooling and detection of the rubidium atoms.

3.1 TRAPPING OF ANIONS

A schematic of the ions path through the HAITrap setup is shown in Fig. 21 as a blue beam. The ions are created from a pulsed gas jet in a plasma discharge. All details of the piezo valve (inset in Fig. 21) for creating the short gas pulses, as well as the plasma discharge are discussed in section 3.1.1. In order to efficiently guide the ions through the vacuum chamber, a combination of electrostatic lenses and benders is used (see section 3.1.2). After leaving the source, the ions are guided into a tof spectrometer from where they are accelerated in transversal direction towards the radio frequency trap. The working principle of the tof spectrometer is explained in section 3.1.3. The spectrometer is optimized to separate the ions according to their charge to mass ratio which allows to selectively load ions of a single species into the radio frequency trap. The ion trap consists of eight gold-coated molybdenum wires (diameter $100\mu\text{m}$) which provide the radial confinement. In axial direction two hollow endcap electrodes allow the loading, trapping and extraction of the ions. Details of the trap setup are discussed in section 3.1.4. Finally, the ions can be detected by a channel electron multiplier (CEM) which is placed behind the ion trap. The read out electronics as well as the algorithm for the ion detection are discussed in section 3.1.5. In combination with a photo-detachment (PD) laser which is used to neutralize the negatively charged ions, the detected ion signal can be used to measure the ions density distribution (PD tomography) as well as the internal state population (PD spectroscopy) which will be discussed in detail in chapter 4.

3.1.1 Ion source

There is a wide variety of ion sources, based on different techniques such as hot filaments, plasmas, electron bombardment, laser ionization and many more [104, 105]. These sources greatly differ in complexity and size and not all of them are applicable for the production of anions [106]. The source used in the HAITrap setup is a modified version of the design introduced by Osborn et al. [107]. This pulsed plasma discharge source is characterized by the following features.

- Compact design. The entire source is placed on a single CF100 flange with a height of only 15cm from the surface of the flange.
- Low extraction voltages. A lot of sources require voltages of several kV to extract the ions from their point of creation. This means that the entire setup has to be operated at similar voltages. In our design the ions leave the source with energies typically below 1eV.
- Pulsed operation. As the entire experiment is run in pulsed operation, a source creating short ion pulses is advantageous. With our design, pulses as short as a few tens of microseconds can be created.
- Easy piezo adjustment. Using the micrometer adjustment screws the piezo position can be optimized while the valve is in operation.
- Low ion flux. Compared to other sources, our design creates a relatively low ion flux. This poses no problem as in the experiment we want to exclude effects of ion-ion interactions such as coulomb repulsion. This limits the number of trapped ions to a few hundreds which can easily be achieved with the relatively low flux created by our source.

Fig 22 shows a schematic of the pulsed plasma discharge source. The ions are created from a pulsed jet of a neutral gas mixture which is ionized in a glow discharge inside the vacuum chamber.

3.1.1.1 Gas reservoir

The gas reservoir (blue area in Fig. 22) contains a carrier gas which enables good plasma ignition (usually hydrogen, helium or argon) seeded with a small fraction of other gases which enable the creation of the desired ions. For the creation of OH^- we use argon seeded with water vapor. An argon gas bottle is connected to the reservoir using a Swagelok system, based on 6mm metal pipes including two pressure reducers which allow a good control of the Ar pressure in the reservoir. In two steps, the Ar pressure is reduced from the bottle pressure (up to 200 bar) to an intermediate pressure of 10 bar and finally down to the reservoir pressure which is typically on the order of 1-4 bar. In order to seed the argon with water vapor, a small water reservoir is connected via a T-piece between the last pressure reducer and the reservoir itself. The water concentration is not actively controlled, only the pressure of the argon and the temperature of the entire setup ($22 \pm 0.5^\circ\text{C}$) is stabilized which results in a stable vapor pressure.

The pressure inside the reservoir is maintained using several sealing rings. A single ring (\varnothing 50mm) is used to seal the connection between the flange and lid B (see Fig. 22). Three more rings (\varnothing 5mm) are

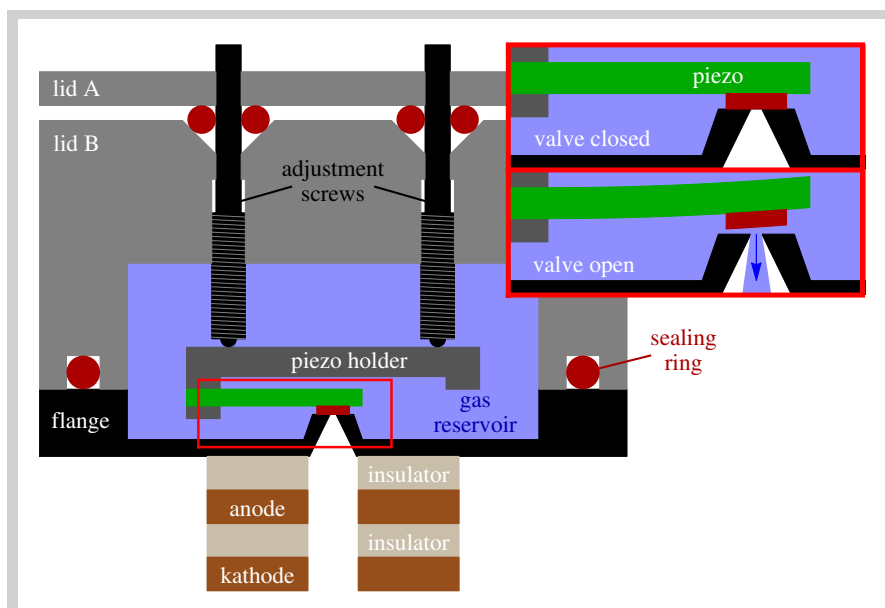


Figure 22: Schematic of the ion source. Shown is a vertical cut through the valve, including a close up of the piezo element and the inlet nozzle. In operation, a pulsed gas jet is created by applying a short voltage pulse to the piezo. Inside the vacuum, the gas is ionized in a plasma discharge. A detailed discription of the setup is given in the text.

used to seal the bore holes for the three adjustment screws (two of which are shown in Fig. 22) used to position the piezo element. In order to achieve a leak-proof seal, the screws are only threaded at the bottom and end in a polished shaft ($\varnothing(5 \pm 0.02)\text{mm}$) at the top which is placed inside a fitting in lid B. The sealing rings are pressed into a countersink at the top of the fitting using lid A (see Fig. 22). For a smooth operation of the screws some vacuum grease is put onto the shaft of the screws. The use of vacuum grease prevents an unwanted contamination of the gas mixture. This design has shown to seal pressure differences of more than 4 bar while it is still possible to turn the screws and adjust the piezo element.

3.1.1.2 Piezo valve

From the cylindrical reservoir the gas can be released into the vacuum chamber through a small exit nozzle which can be opened and closed using the piezo valve. The valve is based on a $12 \times 12 \times 1\text{mm}^3$ bimorph piezo element of type PTZ503. These piezos have conducting surfaces on both sides and by applying a voltage between -165V and $+165\text{V}$ to one side while grounding the other, the piezo bends up or down (depending on the polarity of the applied voltage). This is achieved by mounting the piezo element on a metal holder between two metal electrodes, one of which is grounded, while the other one is connected to

an external voltage supply via an electric feedthrough. The maximum displacement achieved is on the order of $\pm 100\mu\text{m}$ which is sufficient to open and close the $200\mu\text{m}$ exit hole which connects the gas reservoir directly to the vacuum chamber. In order to properly seal the exit hole, a small piece of VMQ silicon rubber (about 1mm diameter) is glued to the bottom surface of the piezo element using vacuum epoxy (Varian Torr Seal). Caution should be taken that no gas bubbles form inside the glue (e.g. by heating up the glue before usage), as these might lead to an unwanted displacement of the rubber seal once the reservoir is put under operating pressure. One should keep in mind that the full dynamic range of the piezo element is only on the order of $100\mu\text{m}$ which means that all parts have to be mechanically stable to a fraction of this distance.

In order to position the piezo with the same accuracy, the three adjustment screws with a thread pitch of only $250\mu\text{m}$ are used. The design is based on typical optomechanical mirror mounts. Three mechanical springs connect the piezo holder with lid B pressing it onto the three adjustment screws. Turning all screws simultaneously, the holder can be moved up- and downwards, while using only one or two of the screws, the holder can be tilted in any direction. A special feature of our design is that in combination with the sealing rings introduced earlier, the screws can be adjusted from outside the gas reservoir. This has proven to be a great advantage in day to day operation, compared to a previous design where the piezo had to be fully adjusted prior to installation in the gas reservoir. Especially during the first couple of hundred or thousand operating cycles of the valve, the rubber seal can slightly deforms as it is repeatedly pressed onto the exit nozzle which requires a readjustment. In our setup the piezo has been adjusted to be closed if grounded and is opened by applying a short voltage pulse of 150V.

3.1.1.3 Plasma discharge

While the valve is open, gas flows through the $200\mu\text{m}$ exit hole which has an increasing diameter in the direction of gas flow. This shape has shown to be advantageous for the production of internally cold ions [107]. The resulting gas jet is directed into a cylindrical channel formed by a stack of an insulation layer, an anode, a second insulation layer and a grounded cathode. Once the gas reaches the volume between anode and cathode about $\Delta t_{\text{val}} = 160\mu\text{s}$ after the valve is opened, the voltage at the anode is rapidly ramped from ground to $U_{\text{pla}} = -800\text{V}$ for about $80\mu\text{s}$ producing a strong electric field. Any free charges in the vicinity are accelerated and can create secondary charges by impact ionization. This results in an avalanche of positive and negative charges which leads to a self-sustaining glow discharge between anode and cathode as long as the voltage is applied. In the glow discharge of Argon seeded with water vapor, OH^- and O^-

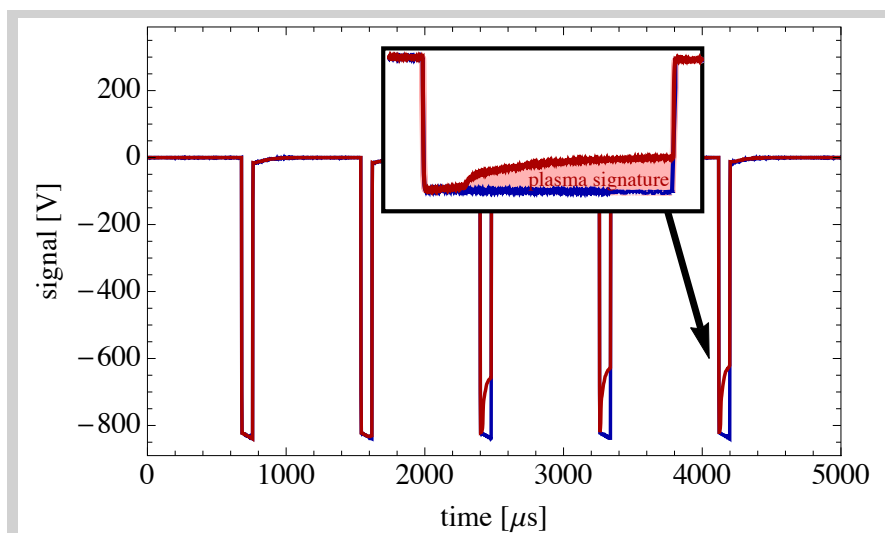


Figure 23: Voltage at the cathode. The blue curve shows the signal without a plasma ignition, the red curve features the typical voltage drop caused to the plasma discharge. The voltage is pulsed five times and the last three pulses all contain a plasma. The inset shows a zoom to the last pulse, the red area between indicates the signature of the plasma ignition, which is also recorded by the experimental control software.

are created via dissociative detachment of water molecules. Once the anode is switched back to ground, the plasma collapses and the constant flow of neutral gas guides the ions out of the nozzle into the vacuum chamber. During this process, the ions repeatedly collide with carrier gas particles which in case of molecular ions such as OH^- leads to efficient cooling of the rotational and vibrational degrees of freedom [108].

A main disadvantage of this technique is that the plasma ignition depends on the presence of free initial charges. These charges can be gas particles ionized by cosmic radiation or remaining charges from previous plasma ignitions. In order to get a more stable plasma we ignite the plasma several times every five milliseconds and only use the last plasma for the experiments. We found that once a single plasma is successfully ignited, all subsequent ignitions are successful. This is indicated in Fig. 23 which shows the plasma signal recorded by monitoring the voltage between anode and cathode using a high voltage probe. Without the plasma the cathode voltage shows the behavior of an ordinary charge and discharge process of a capacitor (blue curve in Fig. 23). However, if a plasma is created, a current flows from anode to cathode reducing the measured voltage (red curve in Fig. 23). The area between both curves, marked in red, is directly correlated with the number of created ions and thus the resulting peak size at the detector. By constantly monitoring the voltage at the cathode and determining the red area via numerical integration in the

experimental control software, weak plasma pulses can be identified. These create only a small number of ions resulting in a low signal at the detector. If the integrated area is below a certain threshold the experimental cycle can automatically be aborted and any recorded data is discarded. This procedure minimizes the influence of fluctuations of the ion source on the recorded data.

3.1.2 *Electrostatic lenses and benders*

The goal of the ion optics is efficient guiding of the ions from the source through the time of flight (tof) spectrometer into the radio frequency trap and finally onto the ion detector. For this purpose a combination of different electrostatic lenses and benders is used. The benders are used to manipulate the direction of the ion beam, the lenses are used to modify the beam divergence.

3.1.2.1 *Working principle of the ion optics*

Every bender consist of two metal plates, one of which is grounded while the second one is connected to an external voltage supply. By applying a voltage to the second electrode the horizontal/vertical direction of the ion beam can be adjusted. The additional electrostatic ion lens is used to focus and defocus the ion beam. An ideal ion lens consists of three coaxial cylindrically-shaped electrodes. Typically the outer electrodes are grounded ($\Phi_0 = 0$), while the potential of the center electrode Φ_1 is adjusted. Fig. 24 (a) shows the potential surface as well as a simulated beam path for $\Phi_0 < \Phi_1$. An ion passing the lens perfectly on the center axis will only experience a force in axial direction decelerating the ion in the vicinity of the center electrode before being accelerated back to its initial velocity. For an off-center trajectory however, the ion experiences an additional force in transversal direction. The strength of this force depends on the curvature of the electric potential in radial direction $\Phi''(z) = d^2\Phi/dr^2|_z$. For $\Phi''(z) > 0$ the transversal force points towards the center axis, for $\Phi''(z) < 0$ away from the center axis, focusing and defocusing the ion beam respectively. Fig. 24 (b) shows the curvature in radial direction as the ion passes through the lens (dashed red line). At the border between every two electrodes (indicated by the dashed black lines) the ion experiences a region of focusing and a region of defocusing, as schematically depicted in Fig. 24 (c). An overall focusing of the ion beam is achieved as the ions are decelerated inside the center electrode thus spending more time in the regions focusing the beam than in the regions defocusing it. The same argument holds if the potential of the center electrode is chosen to be smaller than the ones of the outer electrodes. In this case the ion is accelerated in the center part of the lens, but also the regions of focusing and defocusing are reversed, leading to the same overall focusing effect as before.

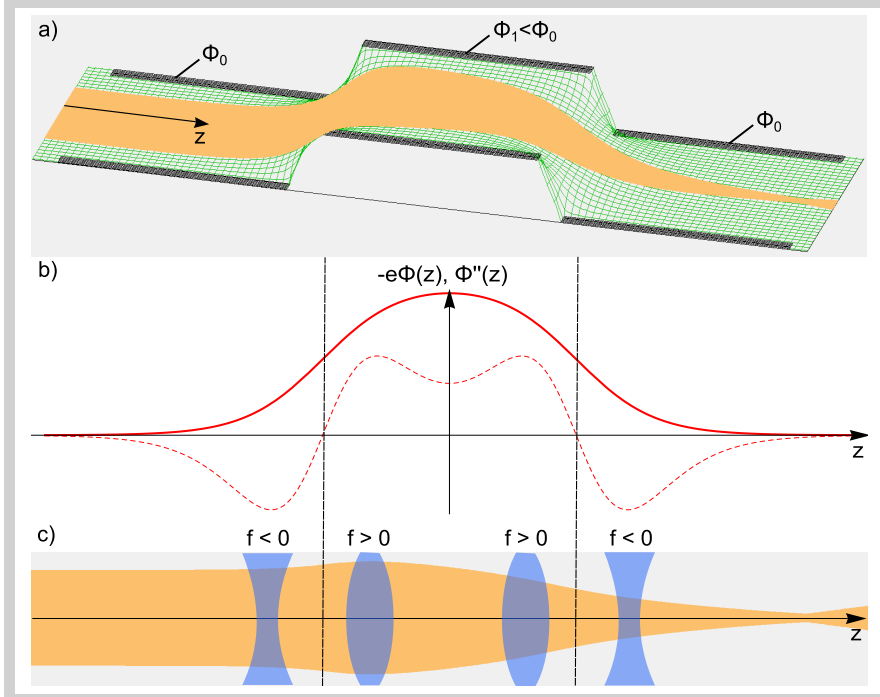


Figure 24: Working principle of an electrostatic einzel lens. (a) The potential surface for a lens with $\Phi_0 < \Phi_1$ is shown (green grid). Also shown are simulated ion trajectories passing through the lens. (b) Electric potential and second derivative on the center axis [109] as a function of z -position. (c) Illustration of the beam path in analogy to an optical system consisting of four separate lenses. Taken from [100].

In the so called paraxial approximation which assumes small initial beam divergences, the focal length f of the lens is given by [109]

$$f = 4 \sqrt{\frac{E_{\text{kin},i}}{q}} \left(\int_{z_0}^{z_1} \frac{\Phi''(z)}{\sqrt{\Phi(z)}} dz \right)^{-1}, \quad (45)$$

with $q \rightarrow$ ions' charge,
 $E_{\text{kin},i} \rightarrow$ initial kinetic energy of the ions.

The zero of the potential $\Phi(z)$ corresponds to a vanishing ion energy. The points z_0 and z_1 mark the axial position of the entrance of the first and the exit of the last cylinder respectively.

3.1.2.2 Ion optics used in the HAITrap setup

In the HAITrap setup always a combination of two benders for both transversal dimensions and a lens are combined to one unit. In total four of these units are placed in the ions' beam path (see Fig. 21). The first unit is placed directly behind the source and is used to optimize the ion flux into the tof spectrometer. Behind the tof spectrometer

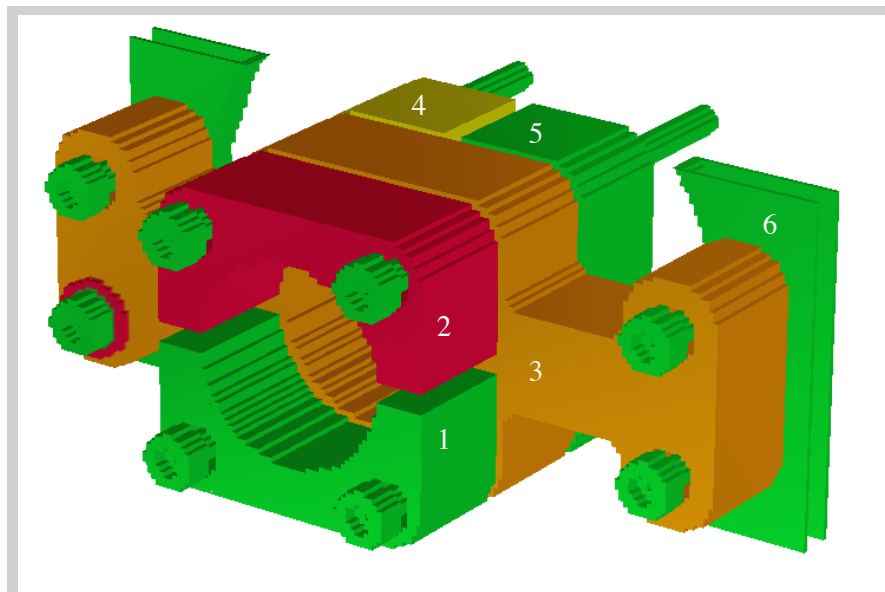


Figure 25: Electrode configuration of the lens-bender combination. Different colors indicate different applied voltages. All green electrodes are grounded. Potential separation is achieved by insulating spacers made from PEEK, placed between the electrodes. The same spacers also insulate the six screws which are used to hold the entire setup together and fix it to a mounting plate (6). Electrodes 1,2 and 4,5 are used as vertical and horizontal benders respectively. All these electrodes combined add up to the outer electrodes which in combination with the center electrode 3 serve as the ion lens.

the ions are guided through a differential pumping stage (second unit) and into the radio frequency trap (third unit). After the ions are released from the trap, they are guided onto the ion detector using the fourth unit. Due to spatial limitations of the first and fourth unit, these units consist of a combined bender-lens setup. Fig. 25 shows the used electrode configuration. The outer cylinders of the lens are both split into two sections which are then used as benders. This setup works well as long as the voltage applied to the benders is by far smaller than the voltage applied to the lens. In our setup this condition is met, as typical voltages applied to the lens are on the order of 100V and beyond, whereas the benders are typically operated with only a few volts.

3.1.3 Time of flight separation

The key element for loading the ions into the trap is the time of flight (tof) mass spectrometer. It is based on the design by Wiley and McLaren [110] and whose discussion we will summarize in this section. The spectrometer employs a combination of three thin plate

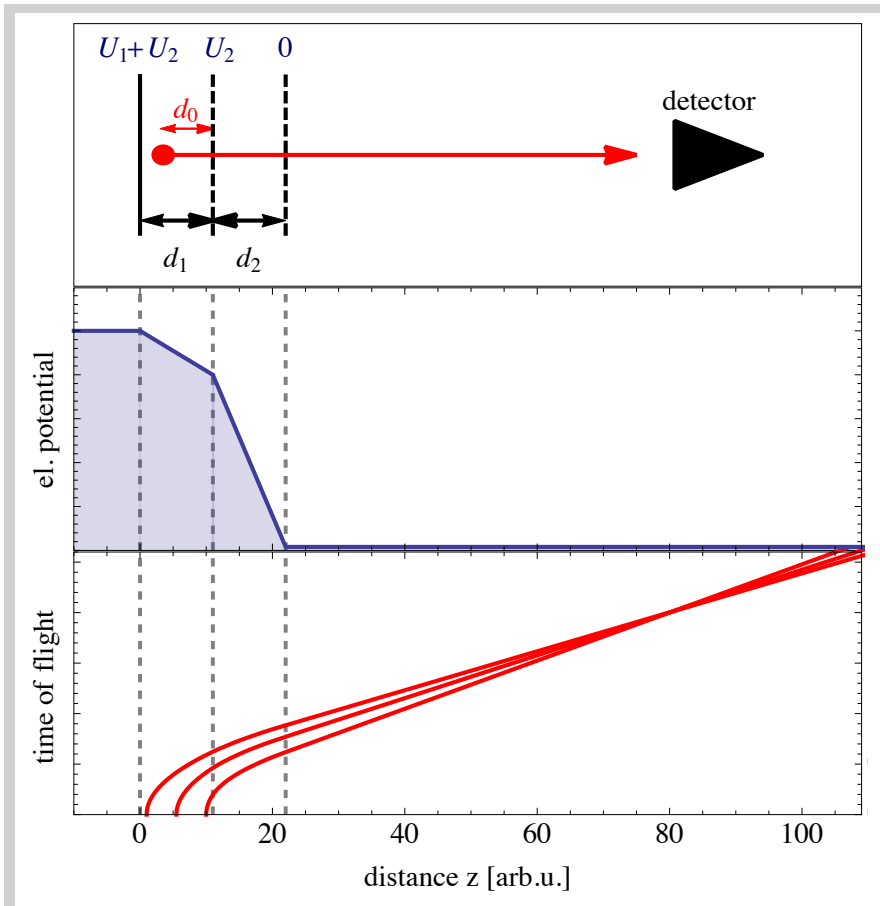


Figure 26: Schematic of the time of flight spectrometer. The top graph shows a schematic of the used setup. The middle figure illustrates the potential landscape and the lower graph shows calculated trajectories for OH^- .

electrodes to separate the ions according to their charge-to-mass ratios. Fig. 26 shows the working principle of this tof mass spectrometer. The ions are placed between two electrodes which have a distance of d_1 and a voltage difference of U_1 . A third electrode is placed behind the second electrode with a distance of d_2 and a voltage difference of U_2 . An ion detector is placed a distance L from the third electrode.

This electrode configuration creates three separate regions which are characterized by their constant field gradients. Placing an ion at a distance d_0 from the center electrode (see Fig. 26), it is accelerated to a velocity of

$$v_1 = v(d_1) = \sqrt{\frac{2q d_0}{m d_1} U_1}, \quad (46)$$

with $q \rightarrow$ ion charge,
 $m_i \rightarrow$ ion mass.

before passing the center electrode and entering the second acceler-

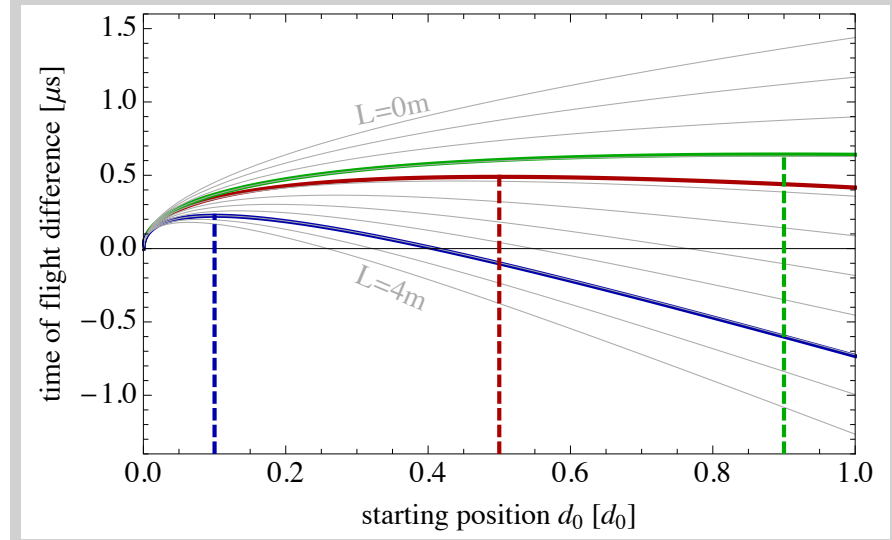


Figure 27: Time of flight of OH^- ions as a function of their starting position d_0 . The top curve corresponds to a detector placed directly behind the third extraction electrode ($L = 0\text{m}$). The other curves correspond to detector positions which are successively increased by 40cm. Also shown are the curves for three optimized positions L_{opt} for small ion distributions centered around $\hat{d}_0 = 0.1d_1, 0.5d_1$ and $0.9d_1$.

ation region. When the ion passes the third electrode and enters the field free drift region, it has reached a final velocity of

$$v_2 = v(d_2) = \sqrt{\frac{2q}{m} \left(\frac{d_0}{d_1} U_1 + U_2 \right)}. \quad (47)$$

Using these two velocities the ion's time of flight to the detector can be expressed by

$$t_{\text{tot}} = \frac{m}{q} \frac{d_1}{U_1} v_1 + \frac{m}{q} \frac{d_2}{U_2} (v_2 - v_1) + \frac{L}{v_2} \propto \sqrt{\frac{m}{q}}, \quad (48)$$

where each summand corresponds to the time of flight in one of the three regions. The total time of flight is proportional to the square root of the ion's mass-to-charge ratio. Fig. 27 shows the ion's time of flight as a function of the starting position d_0 for different placements of the detector. The other variables correspond to the distances and typical voltages used in the HAITrap experiment with $d_1 = d_2 = 11\text{mm}$, $U_1 = 20\text{V}$ and $U_2 = 250\text{V}$.

Fig. 27 illustrates what happens if multiple ions are extracted starting at different positions d_0 . Different starting positions are equivalent to a difference in the time of flight, which is recorded as a wider time of flight distribution at the detector. To minimize this effect, the parameters of the mass spectrometer can be optimized. For an ion cloud centered around \hat{d}_0 with a small spacial spread $\Delta d_0 \ll d_1$, the optimal

detector position L_{opt} corresponds to the one where the derivative of the total time of flight becomes zero at \hat{d}_0 , namely

$$L_{\text{opt}} = \frac{2d_2(\hat{d}_0U_1 + d_1U_2)}{d_1U_1} + \frac{2(\hat{d}_0U_1 + d_1U_2)^{3/2}(d_1U_2 - d_2U_1)}{\sqrt{\hat{d}_0}d_1U_1^{3/2}U_2}. \quad (49)$$

At this position the first order time of flight spread is perfectly compensated, which means that for a small ion cloud, all ions of a given mass reach the detector at the same time t_{tot} . Fig. 27 shows three examples for different starting positions \hat{d}_0 . One should keep in mind that this optimal position is only meaningful for relatively small ion clouds. If however, the ions fill up a substantial volume between the first two electrodes, it is best to choose a large \hat{d}_0 as in this region the optimal time of flight distribution is relatively flat over a large distance. In the HAITrap setup, the distance to the detector is $L \approx 1.4\text{m}$ which lies somewhere between the green and red curve in Fig. 27. Two resulting time-of-flight distributions are shown in Fig. 28. They show good agreement with numerical distributions* calculated using Eq. (48).

3.1.4 Radio-frequency trap

The working principle of linear radio frequency (rf) traps was discussed in great detail in chapter 2. We found that sympathetic cooling with a homogeneous buffer gas is only feasible if the atom-to-ion mass ratio $\xi = m_a/m_i$ is below the critical value of $\xi_{\text{crit}} \approx 1.4(n-1)$, with n being the multipole order of the rf trap. As our first experimental efforts are aimed at cooling OH^- ions ($m_i = 17$) using the ultra-cold rubidium atoms in the MOT ($m_a = 85$), this requires a minimum multipole order of $n = 5$. Only considering the optimal conditions for sympathetic cooling, the multipole order should be chosen as large as possible. Unfortunately, a large number of electrodes creates a problem for the magneto optical trap, as they limit the available optical access. Even with the thin wires used in our trap design, every additional wire disturbs the propagation of the laser beams. The optimal number of electrodes is therefore a trade-off between good sympathetic cooling conditions and sufficient optical access.

We have shown in the previous chapter that the strict limitation $\xi < \xi_{\text{crit}}$ on the mass ratio only holds for homogeneous buffer gases. In case of a localized cloud such as a magneto optical trap, we found that the critical mass ratio loses its meaning as even arbitrarily large mass ratios can lead to stable trapping conditions. Moreover, using a mass ratio beyond ξ_{crit} allows forced sympathetic cooling (FSC), as introduced in section 2.3.6. Using FSC it is possible to tune the ions final energy distribution by simply changing the size of the atom cloud or the radio frequency voltage applied to the ion trap. We therefore decided to use an octupole trap ($n = 4$) for the HAITrap experiment.

* By comparing the measured distribution to numerically calculated distributions using Eq. (48) it is possible to get a good estimate about the center and the size of the ion cloud.

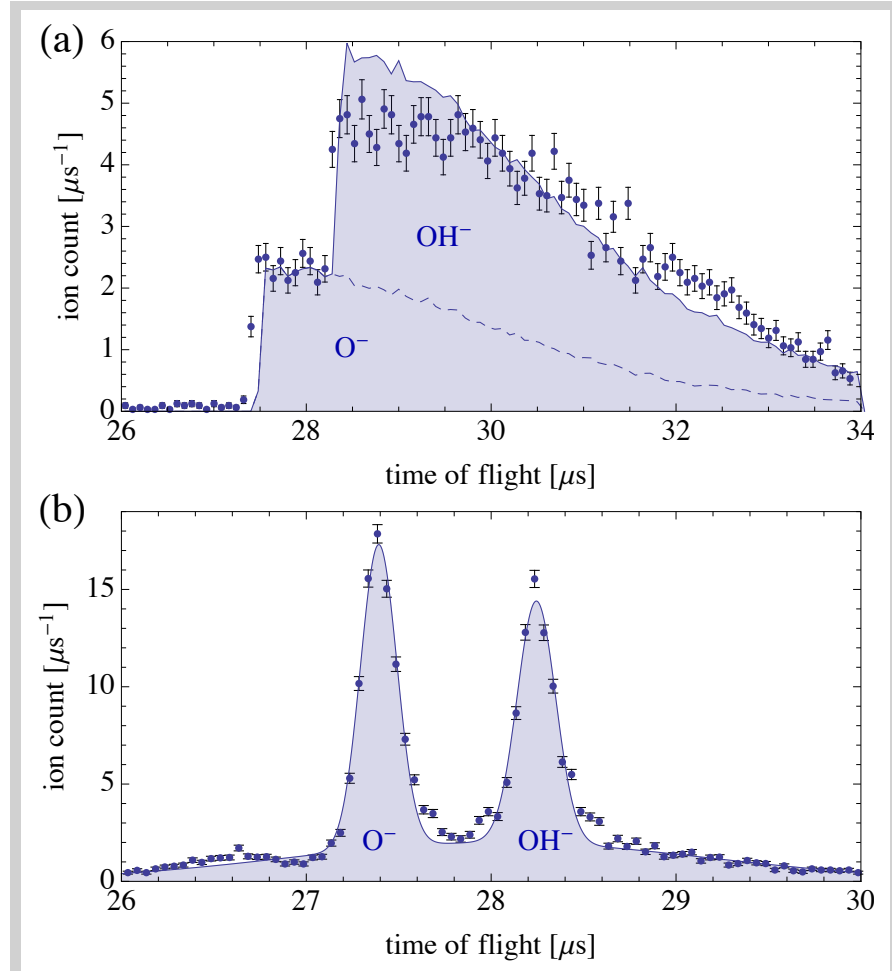


Figure 28: Comparison of measured and calculated tof distributions for two settings of the tof mass spectrometer. The top graph (a) shows an extraction with a single acceleration stage ($U_2 = 0$). In this case the detector is far from the optimal position and the O^- and OH^- ions are not separated. The calculated curve corresponds to a small cloud starting close to the first electrode ($d_0 \approx d_1$). It seems that ions starting further away from this electrode do not gain enough energy to efficiently reach the detector. The bottom graph (b) corresponds to the optimal settings with the detector at L_{opt} . In this case, the OH and OH^- ions are well separated.

3.1.4.1 Trap design

A picture of the trap was already shown at the beginning of the chapter (Fig. 20). The ion trap was designed and constructed in the group of Roland Wester [101, 102] and only slightly modified to fit all requirements of the HAITrap setup. Fig. 29 shows a technical drawing of the trap and its mounting cage. The cage consists of four 5mm threaded rods which are screwed into a CF160 vacuum flange. They are mechanically stabilized by circular metal plates with a hollow center which are placed roughly every 5cm. All components,

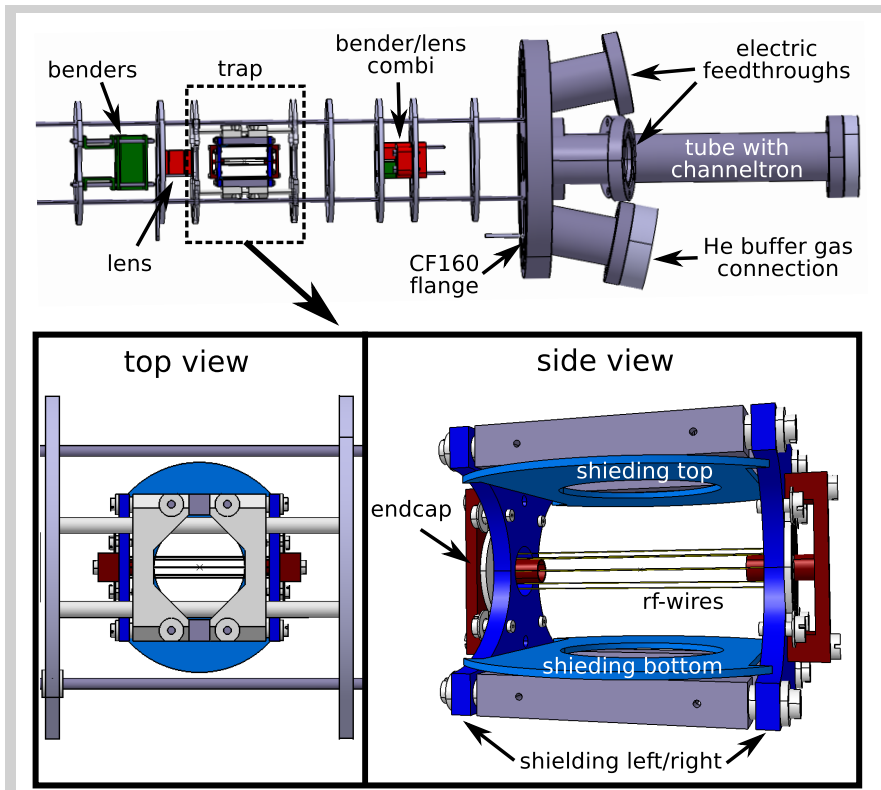


Figure 29: Electrode configuration of the radio frequency trap. At the top the full setup of the CF160 flange holding the ion trap, two lens-bender combinations and the ion detector is shown. All parts are mounted in a cage system built from four threaded rods and circular metal plates placed approximately 5cm. The bottom figures show a top and side view of the ion trap. The different electrodes are indicated by different colors. All blue electrodes are used to shield external fields, the red electrodes are the hollow endcaps used to load the trap and for axial confinement. All white parts are insulators which are placed in a way that they never face the trap itself.

including two sets of benders and electric lenses placed in front and behind the trap are mounted on these circular plates. The CF160 flange splits up into five smaller CF40 flanges, three of which are equipped with electric high-voltage feed-throughs, the center one containing the ion detector and one being currently unused. The main motivation behind this setup was to have the complete mechanical setup as well as the electrical connections to all electrodes on a single vacuum flange. This way, the entire setup could be easily assembled and all electric connections were checked before the entire setup was placed inside the vacuum chamber.

The ion trap consists of eight rf electrodes, two hollow endcap electrodes and four shielding electrodes, two of which are placed in axial direction around the endcaps and two are placed above and

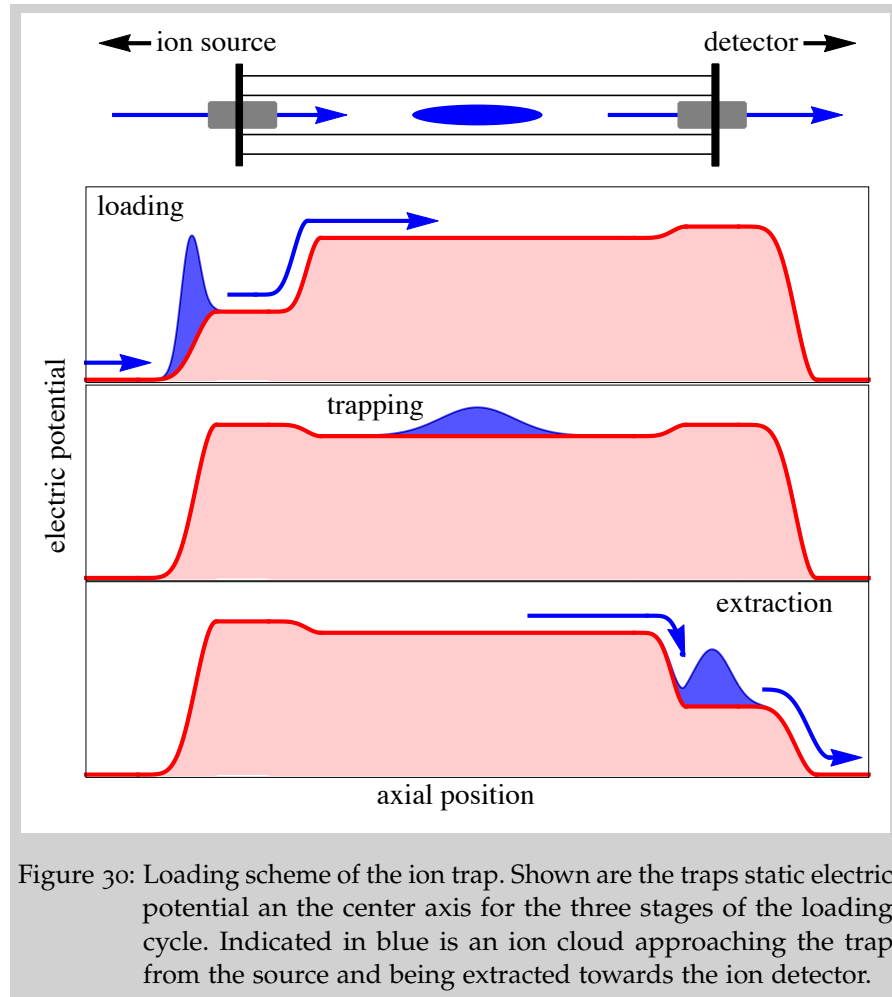


Figure 30: Loading scheme of the ion trap. Shown are the traps static electric potential an the center axis for the three stages of the loading cycle. Indicated in blue is an ion cloud approaching the trap from the source and being extracted towards the ion detector.

below the trap. All these electrodes are held together by plastic screws and are mounted between two of the circular metal plates of the cage. The trap itself has a total length of 34mm and a diameter of 6mm. Radial confinement is provided by eight gold coated molybdenum wires with a diameter of only $100\mu\text{m}$. This is far less than the ideal rod diameter of $d = 2\text{mm}$ (cf. Fig. 1) which results in deviations from the perfect multipole field (Eq. 1) of the ideal linear multipole trap. These deviations are strongest close to the electrodes and become very small around the trap center. We therefore expect the difference to be negligible as long as the ion's are confined sufficiently close to the trap's center.

Typically a radio-frequency voltage of $V_{\text{rf}} = 400\text{V}$ (peak to peak) and $\omega_{\text{rf}} = 2\pi \times 7.8\text{MHz}$ is used which corresponds to a stability parameter of $\eta = 0.03$ for OH^- . The rf-voltage source is based on a design by Jones and Anderson [111, 112]. An additional offset voltage V_{off} can be applied to the rf electrodes putting the whole trap on a higher potential which is used to decelerate the ions when they enter the trap.

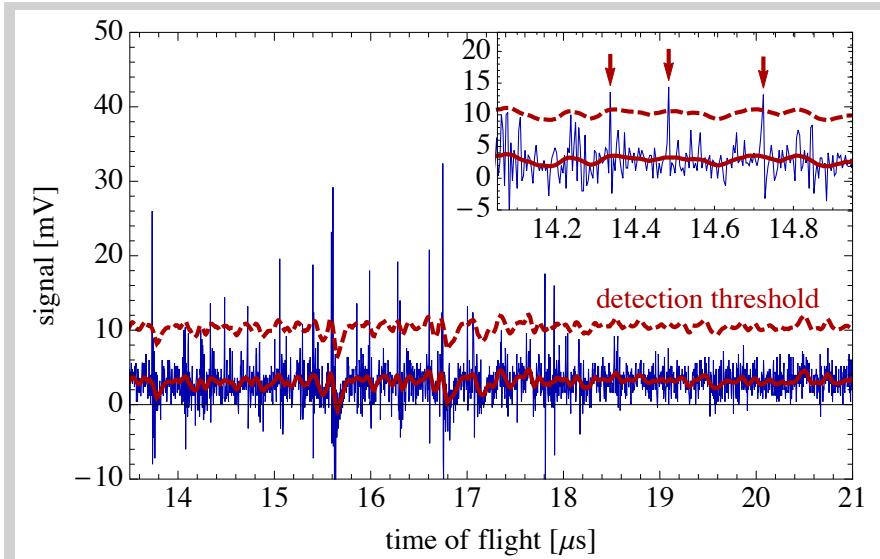


Figure 31: Detection of ions. From the recorded signal a moving average is calculated and shifted by a fixed offset settings the detection threshold. Every time the signal rises over the threshold is counted as an ion, as indicated by the three arrows in the inset showing a zoom into a small part of the trace.

3.1.4.2 Loading and extraction sequence

The ions are guided into the trap through the hollow endcap electrodes placed on both ends of the trap. A typical trapping sequence is shown in Fig. 30. The ions approach the trap from the source with an energy that is determined by the voltages applied to the tof mass spectrometer (Eq. (47)) and is typically on the order of $E_{\text{kin}} \approx 250\text{eV}$. During the loading sequence, both endcaps are open ($V_{\text{open}} \approx 125\text{V}$) and the trap offset is chosen to roughly match the energy of the approaching ions. After the ions pass the endcap facing the source and enter the trap, both endcaps are closed ($V_{\text{close}} \approx 260\text{V}$), providing axial confinement for the ions. In combination with the radial confinement of the rf electrodes the ions are now trapped.

Below the trap a second piezo valve is mounted which is a simplified version of the one presented in section 3.1.1.2 and provides the possibility to flood the trap with helium gas. This way the ions thermalize to approximately room temperature, which significantly increases the trapping efficiency as well as the average storage time. Finally, some time t_{trap} later, the ion's are extracted through the endcap electrode facing the ion detector.

3.1.5 Ion detection

The ions are detected in a channel electron multiplier (channeltron). The detector is placed inside a 20cm long CF₄₀ tube which is connected

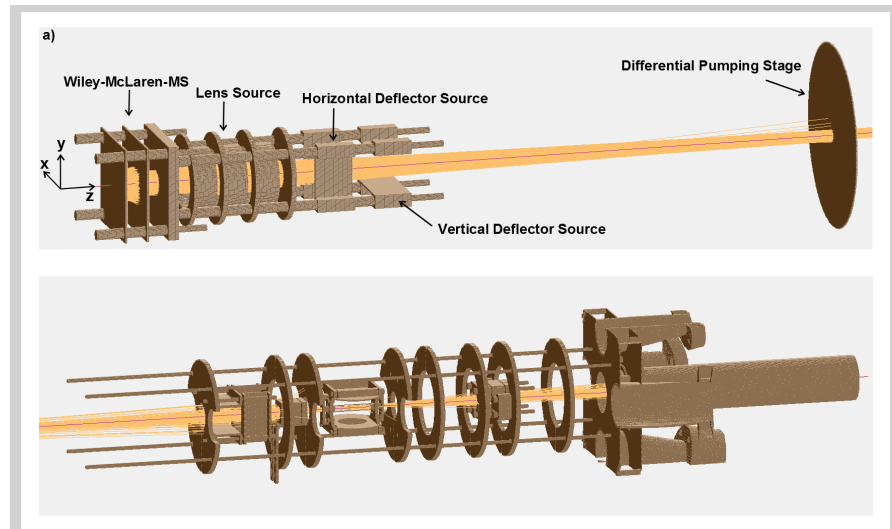


Figure 32: Electrode configuration of the HAITrap setup as implemented in SIMION. The top part shows the setup of the source chamber up to the differential pumping stage, including the tof mass spectrometer. The bottom part shows the science chamber, including the radio-frequency trap. In SIMION the fields are calculated based on a three dimensional grid with cubic unit cells. In order to account for the different sizes of different electrodes, the whole setup has been constructed out of multiple grids with different resolutions. Especially the trap electrodes were simulated with an increased resolution to account for the very small rf electrodes. Some resulting trajectories are shown in orange. Adapted from [100].

to the center of the CF160 flange holding the ion trap setup (see above). Depending on the charge of the ions, the detector and the read out electronics can be operated in two different modes, one for positive and one for negative ions. A single ion hitting the detector leads to a small voltage peak with a width of approximately 5ns and a height of $30\mu\text{V}$. This signal is amplified by a fast pre-amp and recorded by a digital oscilloscope which is connected to the experimental control software. After a full ion trace is recorded it is transferred to the computer where it is analyzed directly by the software to display the number of detected ions and saved for later analysis. The algorithm for counting the number of ions in a single trace is illustrated in Fig. 31.

3.1.6 Optimization of the trapping efficiency

The trapping efficiency of the ions depends on a large number of parameters, from the ion production all the way to the extraction from the trap. We will discuss the relevant parameters in the order of their location in the ions beam path. Due to the large number of parameters involved and the fact that many of them are strongly correlated we

decided to simulate the ion's beam path through the entire setup using a numerical simulation software called SIMION. Fig. 32 shows the entire electrode configuration as it was implemented in the software, including a set of simulated ion trajectories. A detailed description and all results of these numeric calculations can be found elsewhere [100].

3.1.6.1 Ion production

The efficiency of the ion production depends on different parameters starting with the used gas mixture and gas pressure. The gas mixture determines which kind of ions are produced and the pressure influences the velocity distribution of the gas jet leaving the valve. In order to achieve a stable plasma ignition the gas mixture typically contains a large fraction of a gas like hydrogen, oxygen, argon, nitrogen or neon seeded with a small fraction of a different gas which is chosen depending on which ions are desired. For the production of OH^- we use argon seeded with water vapor [113, 114].

The piezo valved is opened for $t_{\text{valve}} = 80\mu\text{s}$ and $\delta_{\text{plasma}} = 160\mu\text{s}$ after the valve opens a voltage of $U_{\text{plasma}} \approx 830\text{V}$ is applied to the anode for $t_{\text{plasma}} = 80\mu\text{s}$. As explained before, this procedure is repeated five times with a delay of $750\mu\text{s}$ between consecutive pulses which greatly increases the chances of a successful plasma ignition. The last pulse is then used to load the ion trap.

3.1.6.2 Ion benders and lenses

The voltages applied to the different benders and lenses differ for each bender/lens combinations. Voltages applied to the benders are typically below 20V, whereas the voltages applied to the electro-static lenses strongly depends on the velocity of the ions. From the numeric simulations we know, that the voltages for the lenses have two optima, one at positive and one at negative voltages [100]. We found the same behavior in the experiment. For an acceleration voltage of $U_{\text{off}} = -250\text{V}$, the positive optimum for all lenses following the mass spectrometer lies close to +400V, the negative optimum lies in the range between -150V and -200V. Only the lens between source and mass spectrometer is operated at much lower voltages (below 5V), as at this point of the beam path the ions only have thermal velocities. The settings used for all measurements presented in this work can be found in Table 1.

3.1.6.3 Time-of-flight mass spectrometer

There are two main settings for the mass spectrometer, the applied voltages and the time at which the spectrometer is triggered. The time is set as a fixed delay δ_{spec} relative to the plasma ignition which has to match the ions time-of-flight from the source to the spectrometer.

	hor. bender	vert. bender	lens
source	0V	-19V	0V
mass spec.	-17.3V	10.7V	200V
trap	2V	-12.3V	165V
detection	0V	0V	140V

Table 1: Typical settings of the benders and lenses.

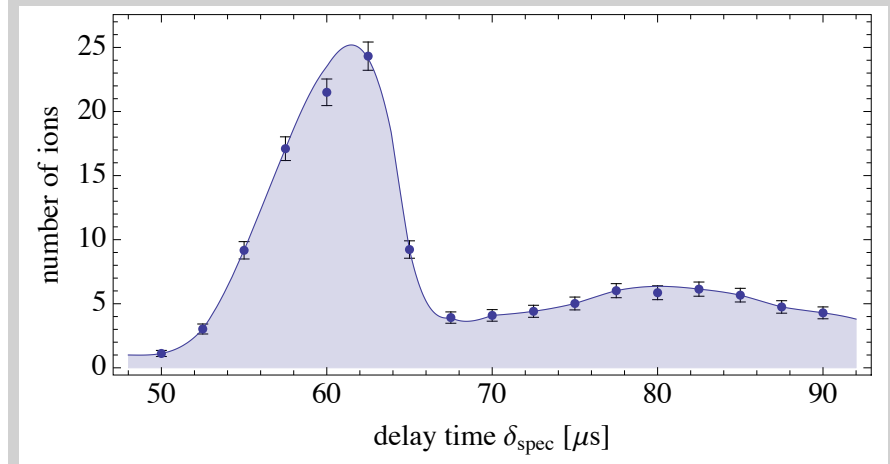


Figure 33: Number of ions depending on the timing of the mass spectrometer. Every delay time corresponds to a different time-of-flight from the source and thus a different velocity. Therefore, the shape of the curve directly relates to the velocity distribution of the ions.

By varying the length of the delay (see Fig. 33), it is possible to gain information about the velocity distribution of the ion beam from the source.

Choosing the voltages of the time of flight mass spectrometer, different aspects have to be considered. First, the ratio of the two voltages U_1 and U_2 define the focus point of the mass spectrometer as defined in Eq. (49). In order to efficiently load the trap, the focus should lie somewhere inside the rf-trap such that ions of the same species reach the trap in a tightly focused bunch with the time of flight of the different species being proportional to $\sqrt{q/m}$. This way, different species can be selectively loaded into the trap by adjusting the closing time of the endcap electrodes.

Second, the voltage U_1 also determines the energy spread of the ions as they reach the trap. As typical trap depths are typically below 1eV, all energy spreads larger than this reduce the loading efficiency. This is particularly the case for ion clouds with a large initial spatial distribution Δd_0 (cf. Fig. 27).

Third, the absolute magnitude of the voltages U_1 and U_2 influences the time it takes the ion's to reach the trap. On the one hand, choosing

low voltages results in a better temporal separation of the different species which simplifies the selective loading process. On the other hand, large voltages typically increase the transfer efficiency from the mass spectrometer to the trap as fast ion beams are easier to focus and the initial momentum and spatial spread becomes less relevant.

Consequently, the best choice of U_1 and U_2 is a trade-off balancing all these opposing effects. For the HAITrap experiment the voltages $U_1 = -10\text{V}$ and $U_2 = -245\text{V}$ voltages are chosen in a way, that the focus of the mass spectrometer lies behind the trap

3.1.6.4 Ion trap

The voltage applied to the rf-electrodes is $U_{\text{off}} + U_{\text{rf}} \sin(\omega t)$ with $U_{\text{rf}} \approx 200\text{V}$ and $\omega = 2\pi \times 7.6\text{MHz}$. The voltage offset is required to decelerate the ions inside the trap and is therefore chosen to match the voltages of the mass spectrometer with $U_1 + U_2 < U_{\text{off}} < U_2$. While the ions enter the trap from the mass spectrometer, the endcap electrodes are set to a voltage of $U_{\text{ec,open}} = -120\text{V}$ (cf. Fig. 30) and $\delta_{\text{close}} \approx 20\mu\text{s}$ after the mass spectrometer is triggered the OH^- ions reach the trap. At this moment, the endcap electrodes are switched to $U_{\text{ec,open}} = U_{\text{off}} - 5\text{V}$, confining the ions inside the trap.

The time delay between the arrival of the OH^- and the O^- ions is too short to selectively only load a single species. In order to eliminate all O^- ions from the trap, the laser of the magneto optical trap can be used as it's wavelength of 780nm is only sufficient to neutralize O^- via photodetachment* [115].

Other crucial parameters are the voltages applied to the four shielding electrodes. Fig. 34 shows the axial and radial potentials of all electrodes surrounding the trap. In order to achieve stable trapping conditions, a potential minimum in all dimensions has to be achieved. Unfortunately, the offset voltage U_{off} applied to the rf wires creates a potential maximum in axial direction which cannot be compensated by endcap electrodes on a similar voltage. Consequently, an axial potential minimum can only be achieved by applying an additional voltage to the shielding electrodes placed to the left and right of the trap, surrounding the endcaps.

The voltages applied to the endcap and shielding electrodes create a de-confinement in radial direction which close to the center scales as $-r^2$. Close to the center, this de-confinement can therefore not be compensated by the radio frequency field which creates a r^6 potential. As a result, the total radial potential always exhibits a local maximum at the trap center surrounded by off-center minima**.

Fig. 35 shows two calculated potentials for voltage combinations resulting in a three dimensional minimum. Also indicated are the ions density distributions assuming a thermal energy distribution. For an offset voltage of $U_{\text{off}} = 250\text{V}$ as used for loading the ion trap from the mass spectrometer, the depth of the radial pockets is on the same order

* The photo-detachment threshold of O^- is 1.49eV whereas the one of OH^- is on the order of 1.83eV. Therefore the 780nm ($E_\gamma \approx 1.59\text{eV}$) laser only detaches O^- .

** This is a common problem of all multipole traps with $n > 2$. Only in a Paul trap with it's r^2 effective potential can a harmonic de-focusing be compensated.

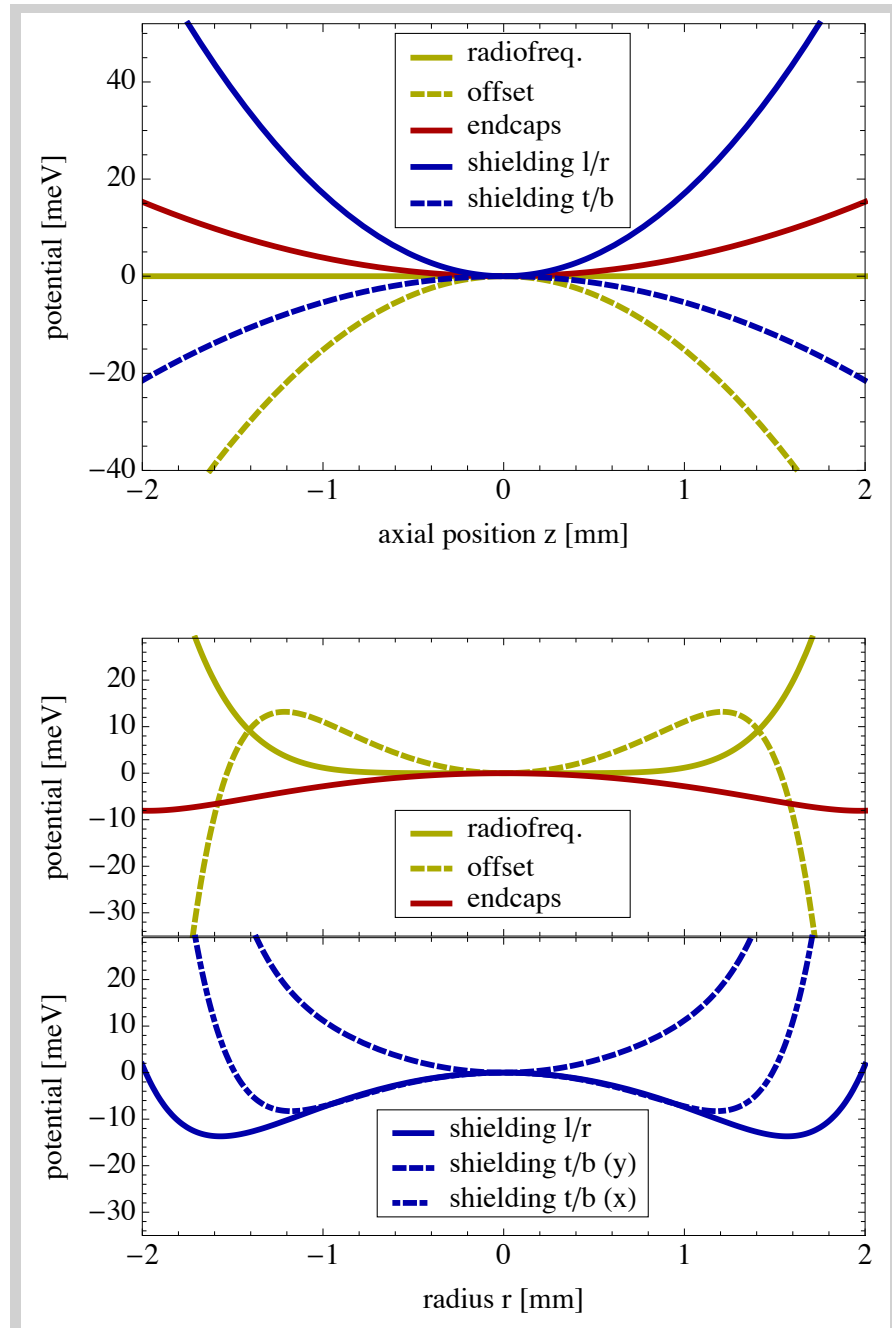


Figure 34: Calculated trap potentials along the center axis of the trap and in radial direction. In axial direction the offset voltage creates a harmonic deconfinement which has to be compensated using the shillings to the left and right and the endcaps. These electrodes than create a deconfinement in radial direction which leads to the advent of radial pockets.

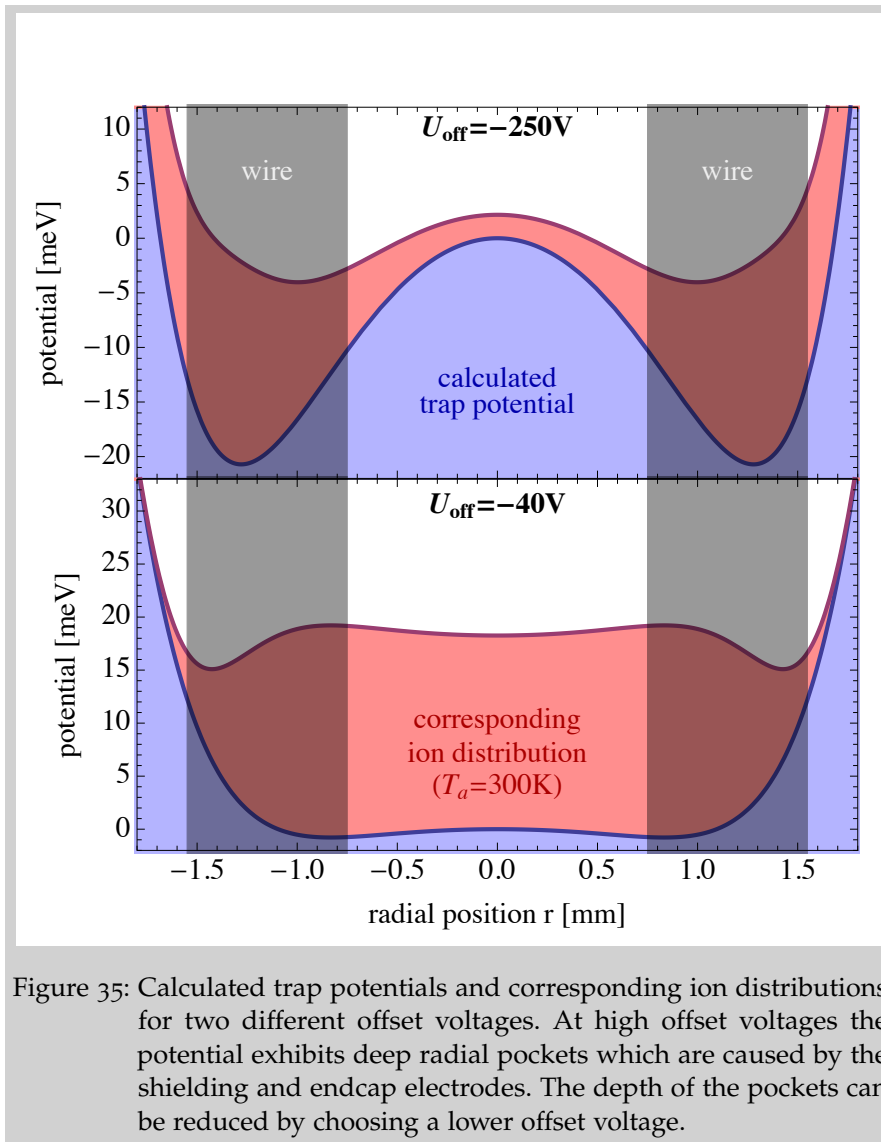


Figure 35: Calculated trap potentials and corresponding ion distributions for two different offset voltages. At high offset voltages the potential exhibits deep radial pockets which are caused by the shielding and endcap electrodes. The depth of the pockets can be reduced by choosing a lower offset voltage.

of magnitude as the thermal energy. The ions are therefore no longer located at the center of the trap. This poses two main problems for the later experiments. First, the ion distribution is imaged from the side of the ion trap by photodetachment spectroscopy (see next chapter). Unfortunately, the line-of-sight to the radial pockets is completely blocked by the radio-frequency wires which are indicated by the gray area in Fig. 35. The laser can therefore not probe a large fraction of the ion density. Second, if the ions are located off-center, the sympathetic cooling is far less efficient. As we have seen in the previous chapter, it is desirable to restrict all collisions to a volume as close to the trap center as possible. In the presence of radial pockets however, collisions at the center cannot reduce the ion's kinetic energy as they mainly possess potential energy at this position.

In order to circumvent this problem, lower offset voltages have to be applied as allows to reduce all other voltages as well with the

exception of the radio-frequency voltage which can remain the same. The resulting radial potential exhibits only pockets which are much smaller than the thermal energy of the ions (cf. bottom graph in Fig. 35).

3.1.6.5 *Extraction and detection*

Finally, at the end of every experimental cycle, the ions are extracted from the trap. This can be done by simply opening the endcap electrode facing the detector. It is preferable however, to apply an additional voltage ramp to the left and right shieldings. These two electrodes can be used in a similar configuration as the electrodes of the time-of-flight mass spectrometer focusing the ions according to their charge-to-mass ratio.

The extraction can be optimized under two different aspects. First, the extraction voltages can be chosen to focus the ion's onto the detector. In this case, different ion species which might be present inside the trap can be separated by time-of-flight which might be particularly useful to investigate chemical reactions happening inside the trap. Second, the focus point can be chosen as far away from the detector as possible. In this case, the ions time-of-flight mainly depends on their starting position inside the trap. Consequently, the measured time-of-flight distributions give direct informations about the ions axial density distribution.

3.2 THE ATOM TRAP

In this section we will discuss the magneto optical trap for rubidium atoms used in the HAITrap experiment. Laser cooling and trapping of the atoms is achieved by six laser beams which are slightly detuned from a closed atomic transition. An introduction into the principles of atom light interactions is followed by a discussion of the cooling and trapping forces in a magneto optical trap. After this conceptual introduction, details of the experimental setup as used in the HAITrap are presented. All required laser beams are prepared on a separate optical table and transported to the experiment via optical fibres. In the experiment the atoms are pre-cooled in a two dimensional magneto optical trap which creates a dense beam of rubidium atoms which has an average velocity by far lower than the thermal velocity. This beam is directed towards the center of the science chamber where the atoms are trapped in a dark spontaneous force optical trap which is an improved version of the standard magneto optical trap. Finally using a resonant laser beam the atoms are detected on a CCD camera placed below the science chamber.

3.2.1 Principle of a magneto-optical trap

A magneto-optical trap uses the light forces acting on an atom placed inside a near-resonant laser beam which is detuned from the atoms resonance frequency ω_0 by $\delta_\gamma = \omega_\gamma - \omega_0$ with ω_γ being the frequency of the laser. The actual frequency experienced by the atom depends on its velocity in propagation direction of the laser which induces a Doppler-shift of $\delta_{\text{dop}} = \vec{k}\vec{v}_a$ with \vec{k} being the wave vector of the light field and \vec{v}_a being the atom's velocity. The resulting velocity dependent force is largest for a velocity v_{res} leading to a Doppler shift exactly matching the detuning of the laser ($\delta_{\text{dop}} = \delta_\gamma$). For a laser with $\delta_\gamma < 0$ the atom experiences a strong decelerating force if traveling with v_{res} towards the laser ($\delta_{\text{dop}} < 0$) compared to a much weaker accelerating force if moving away from the laser. Using six of these red-detuned laser beams ($\delta_\gamma < 0$) pointing on the atom from all direction this leads to a force which always acts against the propagation direction of the atom. Consequently, the atom performs a strongly damped motion efficiently reducing the atoms velocity. A resulting gas of laser cooled atoms is called an optical molasses.

Additional spatial confinement of the atoms can be achieved by superimposing a magnetic quadrupole field and using circularly polarized laser beams. In the same way, the velocity dependent force lead to a strong damping of the atoms velocity, the interplay of magnetic field and light polarization leads to a spatially dependent force which points to the center of the quadrupole field [116]. Fig. 36 shows the magnetic quadrupole field and corresponding light polarizations

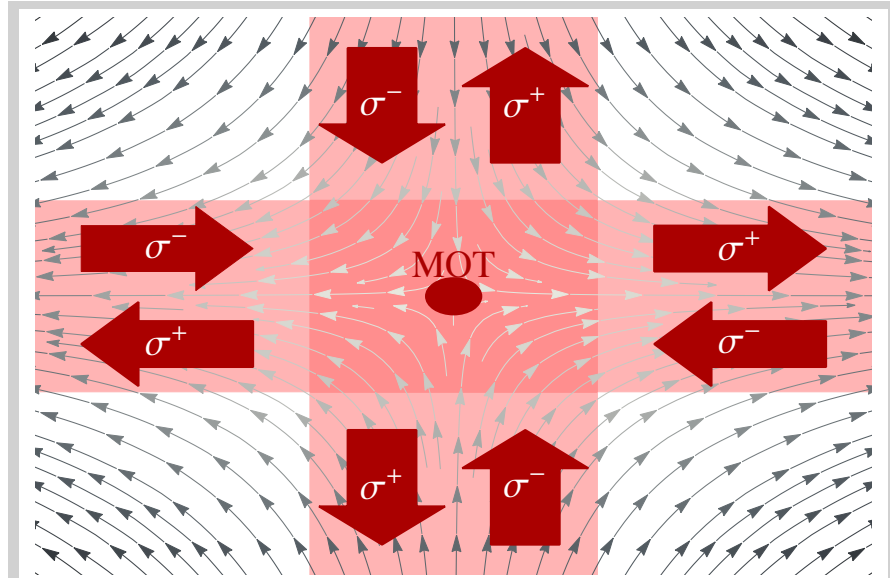


Figure 36: Magnetic field and laser configuration of a magneto optical trap. With the shown combination of magnetic quadrupole field and circular polarization a magneto optical trap can be realized. The polarization of every beam before and after the center of the magnetic field is indicated.

needed for a magneto-optical trap (MOT). In the literature there is some confusion about the correct light polarization which is mainly caused by miss-labeled polarization states. The beams in Fig. 36 are labeled with σ^+ and σ^- indicating their sense of rotation with respect to the magnetic field direction. Consequently, every beam changes its label as the orientation of the magnetic field inverts at the center of the quadrupole field (see Fig. 36). The confining force results from the spatially dependent Zeeman splitting of the atomic sublevels resulting in different transition frequencies for the two light polarizations. For the definition used here, σ^+ polarization results in a larger, σ^- in a smaller transition frequency. As before, the laser is red-detuned from the unshifted transition which yields a stronger photon scattering and thus a force from the beams with σ^- polarization. Only at the center the forces are balanced as the magnetic field becomes zero. Therefore, if all beams approaching the center have σ^- polarization, a confining force pointing to the zero of the magnetic field is achieved.

3.2.2 Laser system

Fig 37 (left side) shows the level scheme of the rubidium (^{85}Rb) D_2 line which is used in our experiment. In order to set up a magneto optical trap for any species, one is always trying to find so called closed cooling transitions. A closed cooling transition refers to a transition from an initial state $|i\rangle$ to an excited state $|e\rangle$ with the only possible

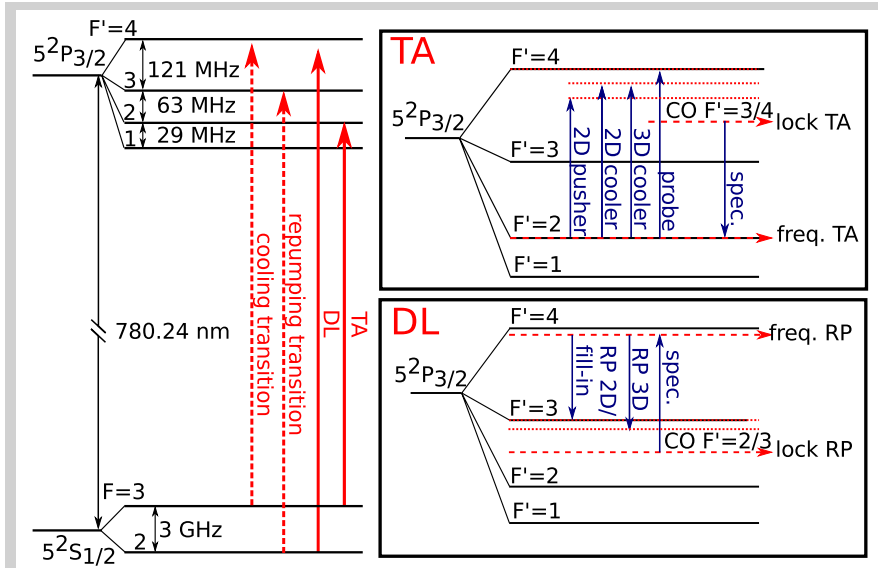


Figure 37: Preparation of all laser frequencies used for the Dark SPOT. The left side shows a hyperfine level scheme of the ^{85}Rb D2 transition (not to scale). Marked are the cooling and repumping transition used for laser cooling and the frequencies of the used lasers. On the right side the preparation of the different beams is illustrated. Both lasers are locked on the strongest crossover peaks. Using an AOM before the spectroscopy setup, the actual laser frequency can be altered independent of the locking point. The use of all indicated laser beams is explained in the text.

decay leading back to $|i\rangle$). Using this kind of transition, the atoms can be pumped between these two states without ever being lost which means that the MOT can be operated using a single laser. Such kind of closed cooling transitions can easily be found in all Alkali metals as they have a simple electronic structure with only a single electron occupying the outermost shell. For ^{85}Rb the transition $5^2\text{S}_{1/2}(F=3) \rightarrow 5^2\text{P}_{3/2}(F'=4)$ is a closed cooling transition.

The only problem of this transition is the relatively small energy splitting of the upper hyperfine states which is only about one order of magnitude larger than the natural line width of the transition $\Gamma = 2\pi \times 6.066\text{MHz}$. Consequently, roughly every 1000 transitions, the atoms are pumped to the $5^2\text{P}_{3/2}(F'=3)$ state from where they can decay to $5^2\text{S}_{1/2}(F=2)$. This state cannot be addressed by the laser pumping the cooling transition as the splitting of the lower hyperfine levels is too large ($\approx 3\text{GHz}$). In order to pump the atoms back to the cooling transition, a second laser is used on the so called repumping transition $5^2\text{S}_{1/2}(F=2) \rightarrow 5^2\text{P}_{3/2}(F'=3)$.

The preparation of all laser beams used in the HATrap experiment is illustrated in Fig 37 (right side). Two lasers are used, a Toptica TA-pro (780nm) with an output power of approximately 750mW and a home-build diode laser with an output power of about 70mW. Both

Beam name	Laser	AOM	detuning
TA spec.	TA	$+2 \times 62$ MHz	—
3D cooler	TA	$+2 \times 83$ MHz	-2Γ
probe	TA	$+2 \times 92$ MHz	0
2D cooler	TA	$+2 \times 87$ MHz	-1.5Γ
2D pusher	TA	$+2 \times 83$ MHz	-6Γ
DL spec.	DL	-2×72 MHz	—
3D RP	DL	-2×56 MHz	0
fill-In	DL	-112 MHz	0
2D RP	DL	-112 MHz	0

Table 2: Laser frequencies typically used in the HAITrap experiment.

lasers are actively stabilized by doppler-free frequency modulation spectroscopy [117]. The required sidebands are added directly in the laser by modulating the current of the diode. The output beam of the laser is split up by a combination of half-wave plates and polarizing beam splitters into five (TA) and four beams (DL). Every beams then passes an acusto-optical modulator (AOM) and is subsequently coupled into an polarization maintaining single-mode fiber which transports the light to the experiment. The AOMs are used to shift the frequency of every beam to the desired value and to turn single beams on and off. Table 2 summarizes all frequencies used in the experiment. All AOM frquencies which are include a factor two correspond to beams which are set up in a double-pass configuration [118]. On the one hand, this configuration has the advantage that the light frequency of the beam can be modified in the experiment without decoupling the beam from the optical fibers. On the other hand, the light has to pass the AOM twice resulting in a lower efficiency as on every pass about 20% of the light is lost. Therefore, only beams whose frequency is adjusted regularly are set up in a double pass configuration.

The two beams labeled with DL spec. and TA spec. refer to the ones used in the Doppler-free spectroscopy setup. These beams are shifted in frequency prior to the spectroscopy setup used to lock the lasers. Consequently, the locking position differs from the actual laser frequency (see Fig. 37). The idea behind this setup is to be able to lock the lasers on the strongest peak of the spectroscopy signal. Unfortunately, starting at this frequency it is not possible to shift all beams to their desired frequencies, as the small shift possible with an AOM is on the order of 60MHz. The purpose of all other beams listed in Table 2 is explained in the following two sections.

3.2.3 Two-dimensional magneto-optical trap

One of the limitations of a magneto optical trap is it's limited capture velocity. The capture velocity denotes the maximum velocity at which

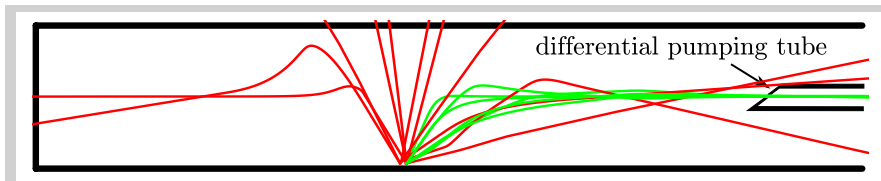


Figure 38: Exemplary trajectories in the glass cell of the 2D MOT. The shown trajectories were calculated by solving the atoms equation of motion in the light field of the 2D MOT setup. All atoms were chosen to start on the surface of glass cell, assuming that inter-atomic collisions can be neglected. The atom flux out of the 2D MOT can be estimated by comparing the number of trajectories passing the exit hole (green) to the number trajectories ending in another wall (red) [120].

an atom can enter the light field of the trap and still be trapped. As discussed previously (see section 3.2.1), the light force is strongest for the velocity v_{res} leading to a Doppler shift matching the laser detuning. Atoms moving faster than this velocity experience a weaker decelerating force and beyond a certain limit (the capture velocity) they pass through the trapping region without being stopped. Typical capture velocities for rubidium are 30-40m/s [119]. This is much lower than the atoms thermal velocity at room temperature ($\approx 300\text{m/s}$) which is why we use a pre-cooled atom beam to load the magneto optical trap.

The atom beam is provided by a two-dimensional magneto-optical trap (2D MOT). A 2D MOT works in the same way as a normal MOT with the only difference being that atoms are only cooled in two dimensions creating a cold atom beam in the third. One could naively think, that the resulting atom beam still has thermal velocities in propagation direction, as the atoms are not actively decelerated in this direction. This is not the case however, as there is a passive selection of slower atoms. Fast atoms pass the light field of the 2D MOT very quickly and are therefore hardly affected by the light forces. Only slow atoms interact long enough with the light field to be confined into the beam and pass a small exit hole which connects the 2D MOT with the main science chamber. This behavior is illustrated in Fig. 38, which shows a set of calculated trajectories with the geometry of the setup matching the one used in the HAITrap experiment.

Fig. 39 shows the 2D MOT setup used in the HAITrap experiment. The central aspects and ideas which led to this final setup are listed in the following.

- Compact design. The 2D MOT is a build as a single module which is connected to the main chamber via a CF16 flange with a tube shaped differential pumping stage in between. All laser beams are transferred to the setup via optical fibers from a separate optical table. The fiber couplers and all the other optics

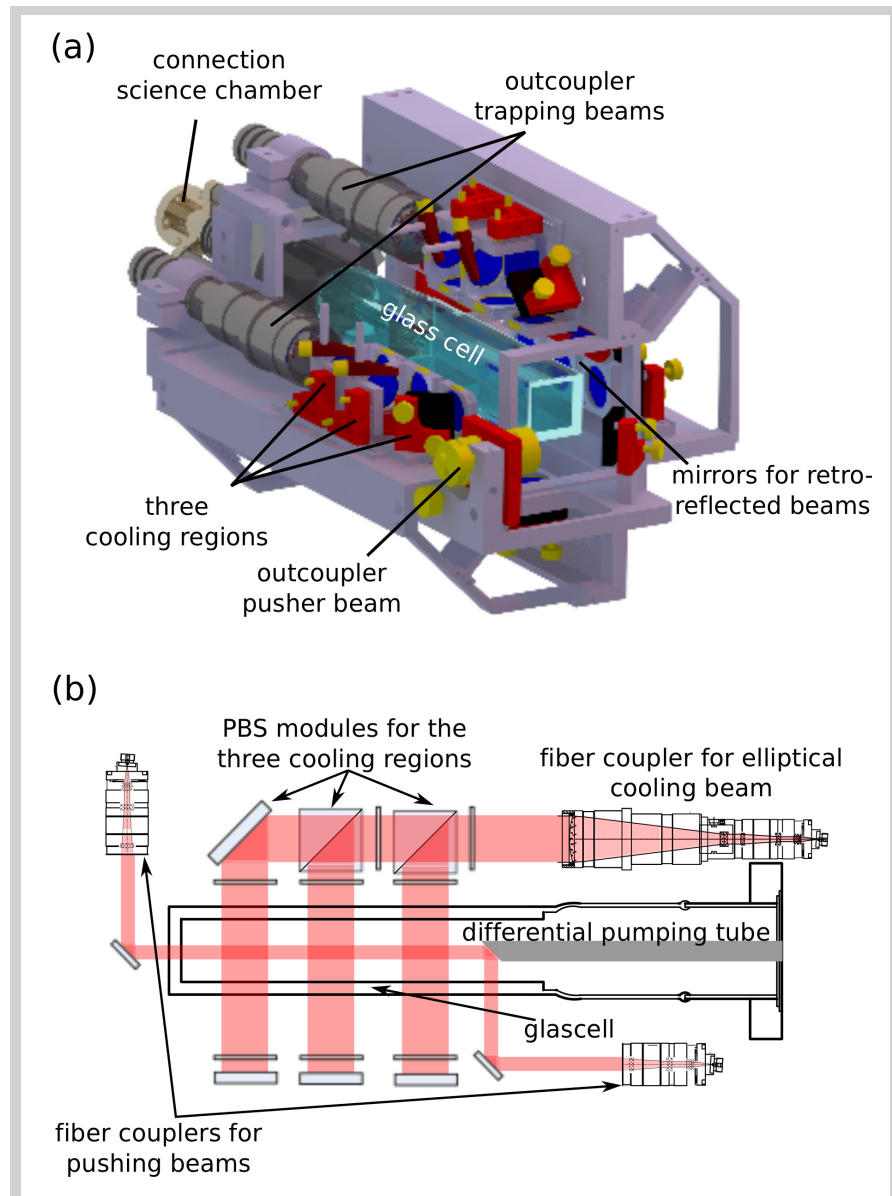


Figure 39: 2D MOT setup as used in the HAITrap experiment. At the top the three dimensional CAD model which was used to machine all parts of the 2D MOT is shown. The bottom figure shows a cut through the center plane of the setup, illustrating the path of all used laser beams. Details about the setup can be found in the text.

is placed on a metal cage which surrounds an AR-coated glass cell which contains two Rb dispensers.

- Sufficient Rb pressure. It has been shown that the flux of the 2D MOT largely depends of the Rb pressure in the glass cell. On the one hand, the higher the pressure, the larger the number of available atoms that can be confined into the beam. On the other hand, a larger pressure also reduces the mean-free-path

length of the atoms which can reduce the achieved flux once it becomes comparable to the average distance to the exit hole. The resulting optimal rubidium pressure has been measured to be approximately 1.8×10^{-6} mbar [121]. In our setup the rubidium is provided by two dispenser located at the end of glass cell facing the science chamber.

- Length of cooling region. A larger cooling region enhances the total trapping volume leading to an increased flux. Moreover, using a longer trapping volume also lets the atoms more time to interact with the light field which increases the number of atoms which can be confined to the beam (see above). We use three separate cooling regions which are created by splitting up the trapping beam using two polarizing beam splitters (see Fig. 39). It has been shown that using multiple cooling regions instead of a single large cooling volume results in nearly the same flux as the transfer efficiency between different cooling regions is very good [122].
- Pushing beam. An additional cooling beams used which passes the glass cell on it's center axis. We find that by choosing a relatively large detuning for this beam, the total atom flux of the 2D MOT can be increased by nearly a factor of two. We attribute this to the atoms which are confined to the center axis but travel in opposite direction. The pusher beam can turn this second beam around which explains the factor of two. In other work it has been found that a second pusher beam in opposite direction can further increase the atom flux and reduce the average velocity of the atom beam [123, 124]. In our setup however, this additional beam only resulted in a lower atom flux which is why it is no longer used.
- Robust magnetic field. A two-dimensional quadrupole field as required for the 2D MOT is created by a total of 12 permanent magnets which are placed on two metal holders around the glass cell. The advantage of using permanent magnets instead of magnetic coils is reduced magnetic noise. Both magnetic holders can be moved in and out to create different magnetic field gradients. The best flux is achieved with a field gradient of 15-18 G/cm. We found that additional compensation coils are required to guide the atom beam through the small exit hole. These two pairs of coils are placed around the cage holding all the optics.
- Differential pumping. In order to maintain good vacuum conditions in the science chamber while still achieving sufficient Rb pressure in the glass cell, a differential pumping stage is placed between the two which can maintain a pressure difference of

up to three orders of magnitude. It consists of a 13cm long tube with a $800\mu\text{m}$ hole on the end facing the glass cell. The small exit hole also filters out faster atoms which as discussed previously are less confined to the center axis (see Fig. 38).

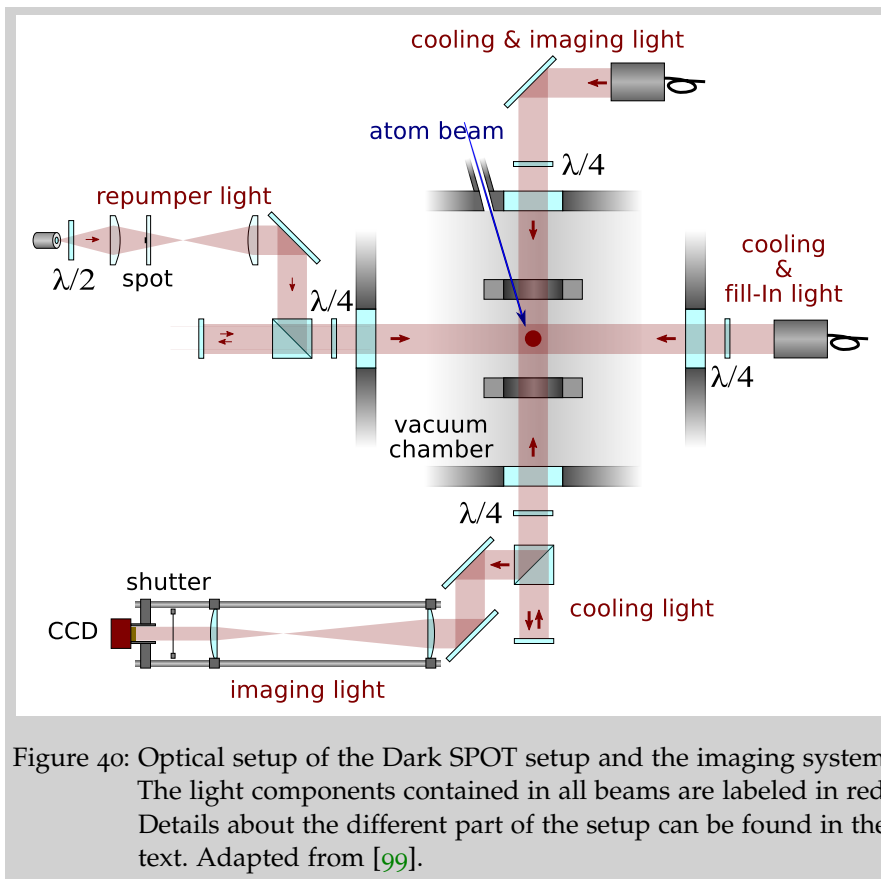
- Laser frequencies and intensities. As explained previously, a magneto optical trap for Rb requires two lasers, one on the cooling (2D cooler) and one on the repumping transition (2D RP). The achieved atom flux strongly depends on the used laser powers as well as the detuning of the cooling laser. We found that the atom flux saturates for a total power (added power of all beams) of $P \approx 110\text{mW}$ for the 2D cooler and $P \approx 5\text{mW}$ for the 3D RP. The optimal detuning of the cooler was found to be $\delta_\gamma \approx 2\Gamma$. For the pusher beam a power of 1mW and a detuning of 6Γ is used.

This setup creates a beam with a total atom flux of 4×10^9 atoms/s, a beam divergence of 26mrad (FWHM) and an average velocity of only 14 m/s, which compares favorably to most other 2D MOTs [125, 123, 126, 121, 124, 127]. Further details about the 2D MOT setup and it's characterization can be found elsewhere [120].

3.2.4 Dark spontaneous force optical trap setup

The atom beam from the 2D MOT is trapped in a dark spontaneous force optical trap (Dark SPOT) [128]. This is a slightly modified version of a normal MOT leading to larger final densities and a larger population of atoms in the ground state. In order to understand the working principle of a Dark SPOT we first have to understand what limits the density in a magneto optical trap. There are three main processes which limit the density. First, multiple photon scattering disturbs the trapping forces, as photons are scattered in random directions with random polarization. These photons are therefore not consistent with the polarization of the trapping and lead to a repulsive force if absorbed by other atoms. Second, inelastic collisions of an atom with a second excited atom lead to losses from the trap, as the trap depth of a MOT is not very large. Third, an elastic collisions with the room-temperature background gas also expels the atom from the trap.

The last loss mechanism can simply be avoided by a sufficiently low background pressure. In our vacuum chamber the background pressure is 10^{-9}mbar which results in an atom lifetime of approximately $3\text{-}4\text{s}$ which is considerably longer than the time required to load the trap which is on the order of 300ms . We are therefore not limited by the background pressure. The other two loss mechanisms however, directly depend on the atom density in the trap. This limits



the maximum achieved densities in a MOT to about 10^{10} atoms/cm³ [129, 130].

The main improvement of the Dark SPOT is to reduce both of these loss mechanisms which is achieved by increasing the population of atoms in the $5^2S_{1/2}(F=2)$ state and thus removing them from the cooling cycle. Less atoms in the cooling cycle results in fewer scattered photons and less excited atoms which were exactly the main factors limiting the density of the MOT. Increasing the number of atoms in $5^2S_{1/2}(F=2)$ the so called dark state, can be done by means of a reduced repumping power or an increased detuning of the repumper.

The problem of this entire scheme is that once the atoms are in the dark state they are no longer actively cooled or trapped. This is why many Dark-SPOTs are operated in two steps. First, in the initial trapping phase the trap is operated with full laser power to achieve efficient loading of a large number of atoms. In a second step the trap is then switched to Dark SPOT operation which leads to a fast increase of the atom density which occurs on a time scale of tens of milliseconds. This is particularly useful if the Dark SPOT is used only as a first cooling step and is for example used to load a dipole trap. In this case a momentary increase of the phase space density is all that is required.

In the HAITrap experiment the Dark SPOT serves as a cold buffer gas for the trapped ions. As the ion-neutral collision rate is typically only on the order of a few Hz, a steady state operation of the Dark SPOT is required. Fig. 40 shows the setup used in our experiment. The setup features the following components.

- **Magnetic fields.** The quadruple field for the MOT is created by two coils placed above and below the ion trap which are operated in anti-Helmholtz configuration. The coils are placed inside the vacuum chamber to minimize the distance to the trap center which allows fast switching times ($\approx 1.2\text{ms}$). Both coils have a total of 12 windings each and are placed 12cm apart with an inner diameter of 7cm. With this configuration magnetic field gradients of up to 60G/cm can be achieved by applying a current of 100A. The coils are made from caption insulated copper wires (2x3mm) with a hollow core which is used for water cooling.
- **Trapping beams.** Three large fiber couplers provide beams with a diameter of 24mm ($1/e^2$) for the magneto optical trap. Two horizontal beams pass the ion trap in a 45° angle with respect to the center axis (see Fig. 21). The third beam passes through the circular holes in the shielding plate at the top and bottom of the ion trap (see Fig. 29). All beams are retro-reflected after passing the chamber and quarter-wave plates placed on all sides of the chamber provide the necessary polarization for the MOT. Every beam contains light on the cooling transition and one additional wavelength which is coupled into the same fiber with crossed polarization. The vertical beam contains resonant light on the cooling transition which is used to probe the atom cloud. Both horizontal beams include light on the repumping transition which we call "fill-in" light.
- **Dark SPOT.** The "fill-in" light included in the two horizontal trapping beams is not used in standard operation but only for absorption imaging as explained below. Instead, two additional fibers provide light on the repumping transition. These beams pass a glass plate with a circular spot in the center blocking the light. This spot is imaged to the center of the chamber where the MOT is created. Fig 41 (a) illustrates the used optics creating a hollow beam with a measured extinction ratio of more than 1:200 at the center. The beams are overlapped with the horizontal trapping beams using a PBS which is placed between the chamber and the mirror for the back-reflected beam (see Fig. 40). With this setup a steady state Dark SPOT has been realized where the atoms at the center are kept in the dark state and only atoms approaching the outer parts of the trap are pumped back to the cooling transition.

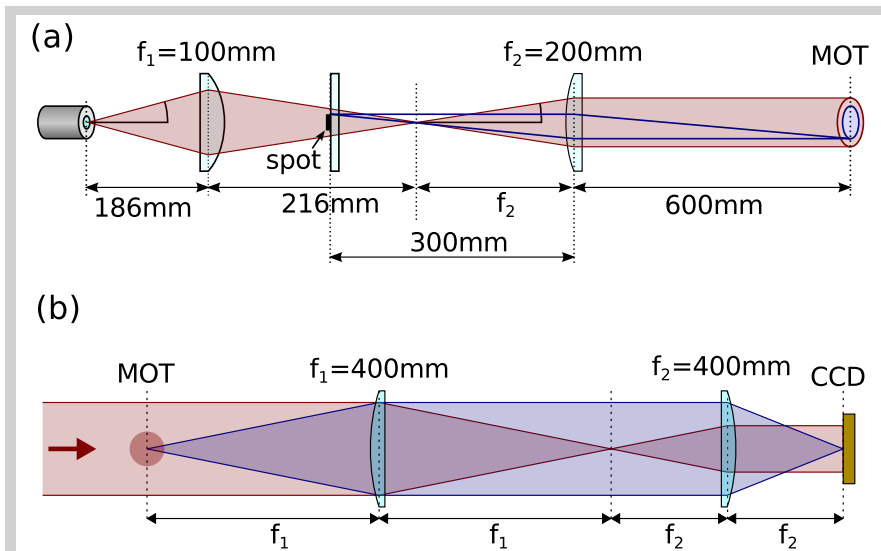


Figure 41: Schematic of the optical setups used to prepare the hollow repumping beam and the imaging system. Adapted from [99].

- Absorption imaging. In order to characterize the atom cloud an absorption imaging system as illustrated in Fig 41 (b) is used. By illuminating the cloud with a resonant laser beam the density profile of the cloud can be characterized. For this purpose the cloud which casts a shadow in the probe beam is imaged onto a CCD camera. As the probe beam only addresses atoms which are in the $5^2S_{1/2}(F=3)$ state all atoms are pumped into this state prior to the imaging sequence using the "fill-in" beam. The probe light is split from the horizontal trapping beam by another polarizing beam splitter which is placed below the chamber. As the cooling and probe light have crossed polarization the MOT operation is not influenced. The used 4-f imaging system reduces the cloud size on the camera by a factor two. Further details about the absorption imaging can be found in the next section.

3.2.5 Saturated absorption imaging

In order to investigate the shape and density of laser-cooled atomic clouds there are two main techniques, fluorescence and absorption imaging. The first one observes the light scattered by an atom cloud illuminated by a resonant laser beam, the latter one detects the shadow in the probe beam created by the scattered photons. With both techniques a two-dimensional projection of the atom density profile can be calculated. This is based on the precise knowledge of the photon scattering rate and angular scattering distribution of all atoms in the cloud. While the magneto optical trap is operated this is a nearly impossible task, as the complicated interplay of beams of different polarizations and the magnetic quadrupole field leads to a complex

spatial dependence of the scattering cross section and angular distribution. In order to measure the atom density with high accuracy it is therefore necessary to take the image under more controlled conditions.

3.2.5.1 Atom-light interaction

The rate at which an atom scatters light from a laser beam can be derived from the optical Bloch equations. For a laser pumping the transition between the ground state $|g\rangle$ and an excited state $|e\rangle$, the atom population in the excited state is given by [131]

$$\rho_{ee} = \frac{(\Omega/\Gamma)^2}{1 + 4(\delta_\gamma/\Gamma)^2 + 2(\Omega/\Gamma)^2}, \quad (50)$$

with Ω	\rightarrow	Rabi frequency,
Γ	\rightarrow	natural linewidth of transition,
$\delta_\gamma = \omega_\gamma - \omega_0$	\rightarrow	detuning from resonance.

This steady state excited state population results from the corresponding photon scattering rate of $R_\gamma = \Gamma\rho_{ee}$ which is typically written in terms of a saturation intensity

$$R_\gamma = \left(\frac{\Gamma}{2}\right) \frac{(I/I_{\text{sat}})}{1 + 4(\delta_\gamma/\Gamma)^2 + (I/I_{\text{sat}})} \quad (51)$$

with I	\rightarrow	laser intensity,
I_{sat}	\rightarrow	saturation intensity of transition.

The saturation intensity corresponds to the intensity at which the scattering rate on resonance reaches half its maximum value of $R_\gamma = \Gamma/2$. This intensity is specific to the driven transition and can be expressed as

$$I_{\text{sat}} = \frac{c \epsilon_0 \Gamma^2 \hbar^2}{4|\vec{\epsilon} \cdot \vec{d}|^2}, \quad (52)$$

with $\vec{\epsilon}$	\rightarrow	unit polarization vector,
\vec{d}	\rightarrow	atomic dipole moment,
$c = 2.997... \cdot 10^9 \text{m/s}$	\rightarrow	speed of light,
$\hbar = 1.054... \cdot 10^{-34} \text{J s}$	\rightarrow	Planck constant,
$\epsilon_0 = 8.854... \cdot 10^{-12} \text{F/m}$	\rightarrow	vacuum permittivity.

This means that the rate at which photons are scattered by the atomic cloud strongly depends on the used polarization and the specific atomic sublevels which are being pumped. The relative transition strengths in the sum are given by the Clebsch-Gordon coefficients of the transition. Table 3 summarizes the coefficients for the cooling transition $5^2S_{1/2}(F=3) \rightarrow 5^2P_{3/2}(F'=4)$. For atoms with multiple

magn. sub-level	σ^+ pol.	π pol.	σ^- pol.
$m_F = 3$	$\sqrt{1/2}$	$-\sqrt{1/8}$	$\sqrt{1/56}$
$m_F = 2$	$\sqrt{3/8}$	$-\sqrt{3/14}$	$\sqrt{3/56}$
$m_F = 1$	$\sqrt{15/56}$	$-\sqrt{15/56}$	$\sqrt{3/28}$
$m_F = 0$	$\sqrt{5/28}$	$-\sqrt{2/7}$	$\sqrt{5/28}$
$m_F = -1$	$\sqrt{3/28}$	$-\sqrt{15/56}$	$\sqrt{15/56}$
$m_F = -2$	$\sqrt{3/56}$	$-\sqrt{3/14}$	$\sqrt{3/8}$
$m_F = -3$	$\sqrt{1/56}$	$-\sqrt{1/8}$	$\sqrt{1/2}$

Table 3: Clebsch-Gordan coefficients of the $5^2S_{1/2}(F = 3) \rightarrow 5^2P_{3/2}(F' = 4)$ transition.

magnetic sublevels, the total scattering rate of the cloud illuminated by a light field with a polarization q is given by

$$R_{\gamma,q} = \Gamma \sum_{m'_F} \rho_{em'_F em'_F} |\langle F' m'_F | F 1 m_F(-q) \rangle|^2, \quad (53)$$

with	$\rho_{em'_F em'_F}$	\rightarrow	population of magnetic sub-level m'_F ,
	F'	\rightarrow	hyperfine level of excited state,
	F	\rightarrow	hyperfine level of ground state,
	m'_F	\rightarrow	magnetic sub-level of excited state,
	$m_F = m'_F + q$	\rightarrow	magnetic sub-level of ground state.

The different polarizations correspond to $q = \pm 1$ for σ^\pm polarized light and $q = 0$ for π polarized light. Besides the different scattering rates, different polarizations also lead to different angular distributions of the scattered light

$$p(\theta, \phi) = \frac{3}{16\pi} (1 + \cos^2\theta) \quad (\text{for } \sigma^\pm),$$

$$p(\theta, \phi) = \frac{3}{8\pi} \sin^2\theta \quad (\text{for } \pi). \quad (54)$$

These complicated dependences on the level populations and light polarizations makes it very difficult to calculate the total scattering rate and angular distribution for arbitrary systems. This is exactly why fluorescence as well as absorption imaging has to be performed under well known conditions.

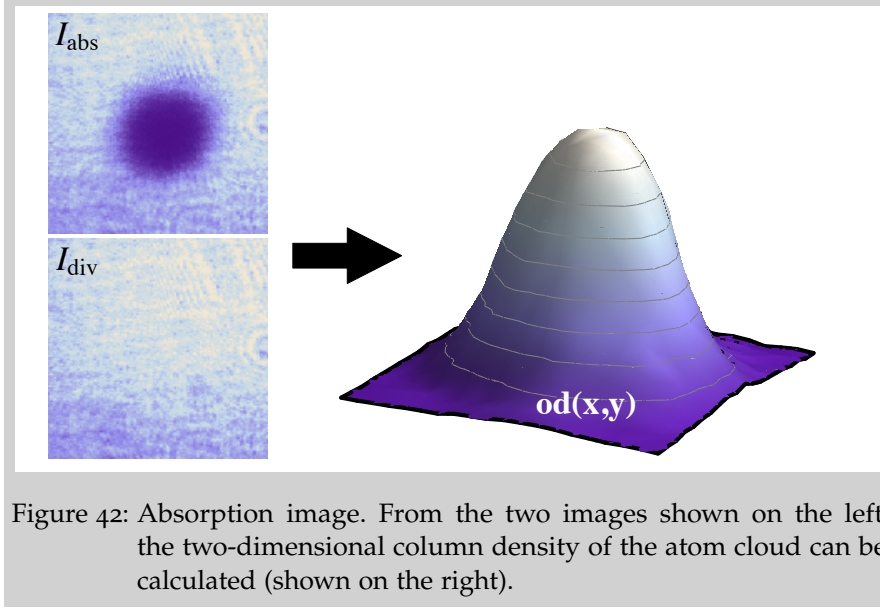
3.2.5.2 State preparation

In order to prepare the system in a well known state, different steps have to be taken [4]. Ideally all atoms are pumped into the same m_F level and are probed with a well known polarization. To reach this goal, a well defined quantization axis is required which is defined by the direction of the magnetic field. Otherwise, it is not even possible to define meaningful m_F states or to label the polarization of the light fields with σ^\pm or π .

Therefore, at the beginning of every imaging sequence all trapping lasers and the magnetic quadrupole field are turned off. Afterwards, a homogeneous magnetic field aligned with the propagation direction of the probe laser is turned on. With these measures we have created a quantization axis along the z-direction and the probe laser has a well defined σ^+ polarization. At this point the atoms are still distributed over all m_F levels of the $5^2S_{1/2}(F = 3)$ as well as the $5^2S_{1/2}(F = 2)$ state. In order to optically pump all atoms into the same magnetic sub-level, the probe laser and the so called "fill-in" beam introduced previously are turned on for a short time. The duration of this pumping pulse should be chosen short enough that the atom cloud is not strongly influenced by the resulting light forces, but long enough to ensure all atoms to reach the outermost m_F level, $|F = 3, m_F = 3\rangle$. We will see in the following that exactly this condition cannot be met for all systems, including ours. The outer m_F state is commonly referred to as the "stretched state" and is a cycling transition for the σ^+ probe beam.

It should also be clear now why we introduced two separate beam pairs on the repumping transition, namely the "3D RP" and the "fill-in" beams. As the first one is prepared as a beam with hollow core (cf. Fig. 41) it cannot be used to pump all the atoms into the stretched state. This is where the "fill-in" beam comes in, which illuminates the whole atom cloud.

After the pumping pulse is complete, the system is in a well defined state and can now be used to perform density measurements with either fluorescence or absorption imaging. Unfortunately, for some systems it is impossible to pump all atoms into the stretched state. This problem occurs as soon as the cloud becomes optically thick. Optically thick means that a probe beam illuminating the cloud, is fully absorbed over the volume of the cloud. As a result, atoms located on the side of the cloud facing the laser, scatter far more photons than the ones located on the rare side. For the pumping pulse this poses a serious problem as it can take many orders of magnitude longer to pump the atoms on the rare side into the stretched state than the ones on the front side. Consequently, the above mentioned condition that the pumping pulse should be short enough for the cloud not to be influenced by the light forces of the probe beam can no longer be fulfilled. Basically, trying to pump an optically thick cloud, the atoms in the front are blown out of the cloud before any light ever



reaches atoms in the rare part. In section 3.2.5.4 we will discuss how this problem can be overcome by saturated absorption imaging.

3.2.5.3 Standard absorption imaging

From Eq. (51) we know that a light field on resonance propagating through an atom cloud exhibits an intensity change of

$$\frac{dI(x, y, z)}{dz} = -n(x, y, z) \left(\frac{\Gamma}{2} \right) \frac{\hbar\omega_\gamma I(x, y, z)/I_{\text{sat}}}{1 + I(x, y, z)/I_{\text{sat}}}, \quad (55)$$

with $I(x, y, z) \rightarrow$ intensity distribution of light field,
 $n(x, y, z) \rightarrow$ density distribution of atom cloud.

For standard absorption imaging the intensity of the probe laser is chosen far below the saturation intensity in which case Eq. (55) results in an exponential absorption, also known as the Lambert Beer's law,

$$I(x, y, z) = I_0(x, y) \exp \left[- \left(\frac{\Gamma}{2} \right) \frac{\hbar\omega_\gamma}{I_{\text{sat}}} \int_{-\infty}^z n(x, y, z') dz' \right] \quad (I \ll I_{\text{sat}}), \quad (56)$$

with $I_0(x, y) \rightarrow$ initial intensity distribution of laser.

In an absorption imaging measurement the column density of the atom cloud $\int n(x, y, z) dz$ is determined by comparing the intensity distribution with the cloud present $I_{\text{abs}}(x, y) = I(x, y, \infty)$ to the initial intensity distribution without the cloud $I_{\text{div}}(x, y) = I_0(x, y)$. These

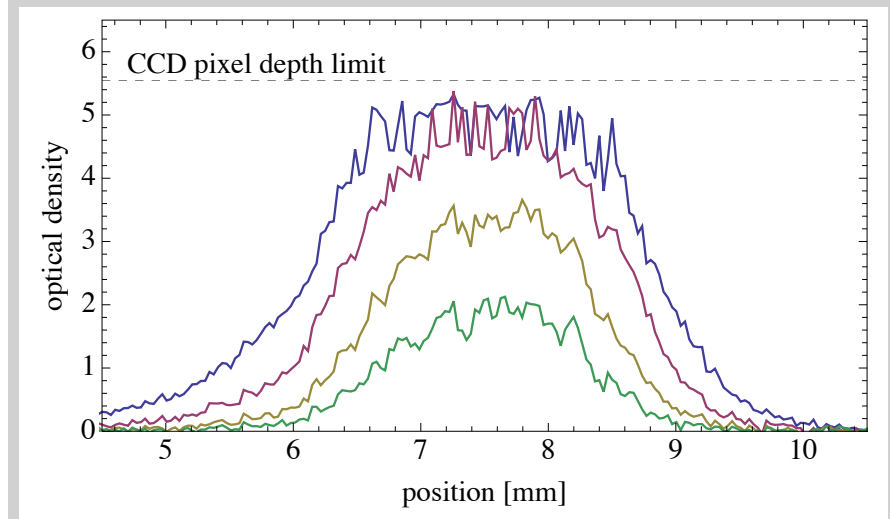


Figure 43: Measured optical density distributions for different peak densities. The detection limit set by the pixel depth of the camera leads to flat top distributions.

two distributions are commonly called the absorption image and the division image. In this terminology, Eq. (56) can be written as

$$\ln \left[\frac{I_{\text{abs}}(x, y)}{I_{\text{div}}(x, y)} \right] = \left(\frac{\Gamma}{2} \right) \frac{\hbar\omega_\gamma}{I_{\text{sat}}} \int_{-\infty}^z n(x, y, z') dz' = \text{od}(x, y), \quad (57)$$

with $\text{od}(x, y) \rightarrow$ optical density.

Fig. 42 shows a typical absorption image as it is recorded in the experiment. The optical density is a direct measure of how strongly the beam is attenuated by the cloud. For an optical density of 5.5 the light intensity is reduced by a factor of $\exp[5.5] \approx 250$ which is already the maximum detection efficiency of an 8-bit camera ($2^8 = 256$) as used in our experiment (see Fig. 43). The optical density at the center of our Dark SPOT is on the order of one-hundred which corresponds to a beam attenuation on the order of 10^{43} . Obviously, even with the best available cameras this cannot be measured. Moreover this is also the reason, why the atom cloud cannot be optically pumped into the stretched state as mentioned previously.

In order to solve this problem we implemented a technique known as saturation absorption imaging.

3.2.5.4 Saturated absorption imaging

The idea behind saturation absorption imaging is to scan the intensity of the probe laser over a wide range to obtain information about the sub-level population of the atom cloud [132, 133]. As discussed above, pumping optically thick cloud into the stretched state is impossible, which means that we are left with an arbitrary distribution over all

magnetic sub-levels. In this case the photon scattering rate is given by Eq. (53) resulting in an attenuation of the probe beam of

$$\frac{dI(x, y, z)}{dz} = -n(x, y, z) \left(\frac{\Gamma}{2} \right) \sum_{m_F} p_{m_F} \frac{\hbar\omega_\gamma I(x, y, z)/I_{\text{sat}}^{m_F}}{1 + I(x, y, z)/I_{\text{sat}}^{m_F}}, \quad (58)$$

with $I_{\text{sat}}^{m_F} \rightarrow$ saturation intensities of the different m_F levels,
 $p_{m_F} \rightarrow$ population of the different m_F levels.

In order to calculate the total absorption it is therefore necessary to know the exact sub-level population. This can be circumvented by assuming that the sum can be approximated by

$$\sum_{m_F} p_{m_F} \frac{I/I_{\text{sat}}^{m_F}}{1 + I/I_{\text{sat}}^{m_F}} = \frac{I/(\alpha I_{\text{sat},0})}{1 + I/(\alpha I_{\text{sat},0})}, \quad (59)$$

with $I_{\text{sat},0} \rightarrow$ saturation intensities of the stretched state,
 $\alpha \rightarrow$ dimensionless scaling parameter.

In this case Eq. (58) becomes formally equivalent to Eq. (55) with an effective absorption intensity of $\alpha I_{\text{sat},0}$. We have verified numerically using arbitrary sub-level population that using the effective absorption intensity typically agrees within a 10% error-margin with the result obtained by using the full sum over all states [99]. Solving Eq. (58) for arbitrary laser intensities leads to an optical density distribution of

$$\text{od}(x, y) = \alpha \ln \left[\frac{I_{\text{abs}}(x, y)}{I_{\text{div}}(x, y)} \right] + \frac{I_{\text{div}}(x, y) - I_{\text{abs}}(x, y)}{I_{\text{sat}}}. \quad (60)$$

This equation differs fundamentally from the low intensity case (Eq. (57)). A useful feature of low intensity absorption imaging is that the absolute intensity of the probe beam drops out of the equation, as only the relative change of the intensity distribution matters. The second term in Eq. (60) however, directly depends on the absolute probe beam intensity. At small intensities the optical density is dominated by the first term but as soon as the intensities is comparable to I_{sat} the second term becomes relevant. For $I \gg I_{\text{sat}}$ the second term which is independent of the parameter α becomes dominant. Consequently, without any knowledge about the sub-level population of the atom cloud and thus α , the actual optical density and thus the atom density can be measured by using sufficiently large probe intensities.

This requires a careful calibration of the intensity distribution of the probe beam at the position of the atom cloud, including the quantum efficiency of the camera, possible losses on all optical elements between the atom cloud and the camera and the magnification of the imaging system. Fig. 44 (a) shows the intensity dependence of the measured optical density \overline{od} . The density \overline{od} is calculated under the assumption that $\alpha = 1$, namely that all atoms are in the stretched state. It therefore differs from the real optical density $od(x, y)$ which is directly

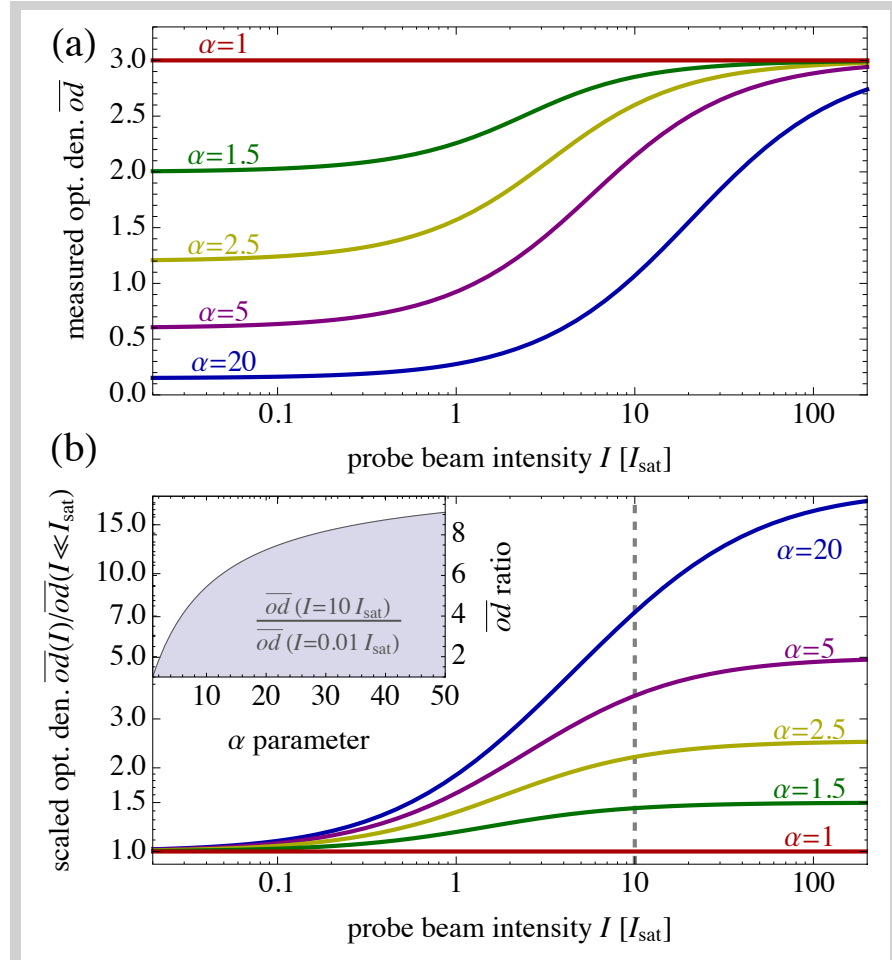


Figure 44: Intensity dependence of the measured optical density \overline{od} for various α s. \overline{od} is calculated from Eq. (60) assuming $\alpha = 1$. (a) The resulting optical density underestimates the real od at small probe beam intensities and converges towards the real value for $I \gg I_{\text{sat}}$. (b) By scaling the distribution to the value of \overline{od} at small intensities, the parameter α can be determined. The inset shows the ratio between two \overline{od} values at different intensities which is characteristic for a given α .

proportional to the column density of the atom cloud and is therefore constant. Only if the real α parameter of the cloud is unity do the two optical densities equal resulting in a constant $\overline{od}(I)$ distribution (cf. Fig. 44). For all other values $\alpha > 1$, the density is under-estimated at small probe intensities and only approaches its real value at large intensities.

Fig. 44 (b) illustrates how this measurement can be used to determine the parameter α . Shown is again the intensity dependence of \overline{od} but this time normalized to the measured optical density at small probe intensities $\overline{od}(I \ll I_{\text{sat}})$. In this case the only free parameter is α which can be estimated from a fit* to $\overline{od}(I)$ or by comparing the measured optical density at any two points (see inset).

* This differs from the method used in [132] where they randomly tried different values of α , choosing the one which led to the smallest variation of the measured optical density.

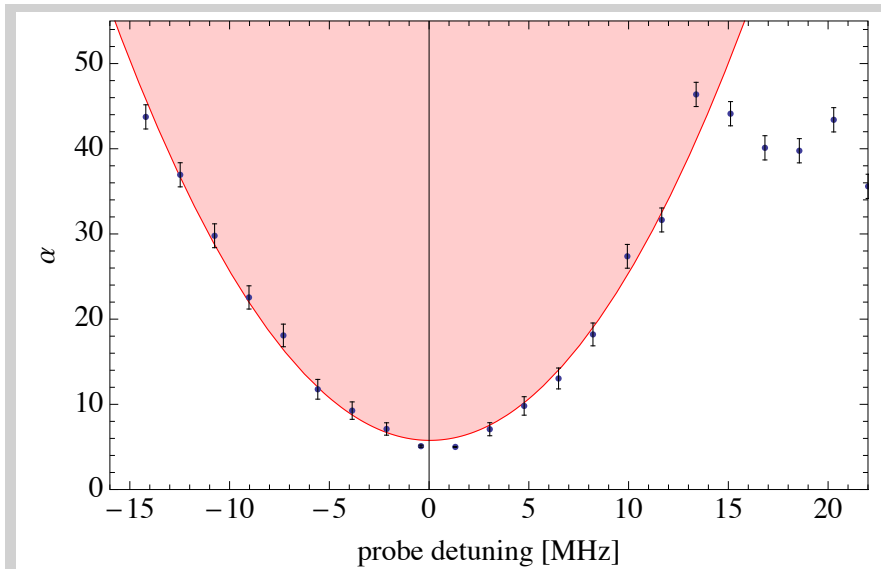


Figure 45: Measured values of α for different probe beam intensities. The solid curve corresponds to a Lorentzian shaped absorption cross section $\sigma(\delta)$ leading to a dependence of $\alpha \propto 1/\sigma(\delta)$.

3.2.5.5 Density distributions of dense clouds

By performing intensity dependent measurements of the optical density it is no longer necessary to prepare the atom cloud in a well defined state but it is sufficient to characterize the absorption cross section by determining α . This can be used to probe atomic clouds with very large optical densities. The idea is to artificially increase α leading to a reduced measured optical density. This way even optically thick clouds can be made transparent again.

One possibility to modify α is to use different polarizations of the light field (see Table 3). But α not only depends on the light polarization and atomic sub-level population but also on everything else modifying the atoms absorption cross section. In most cases this can be done by simply detuning the probe beam from resonance. Fig. 45 shows measured values of α as a function of the probe beam detuning. The solid curve corresponds to the expected distribution assuming a Lorentzian line-shape of the absorption cross section. Only at large detunings there is a significant deviation of the measured points from the expected curve. At this point our fitting algorithm seems to fail as the signal-to-noise ratio becomes too small.

Fig. 46 illustrates a second approach to reconstruct the density distribution of a dense cloud. In this case, the measured distributions at different probe detunings were scaled to match around the outer flank where the optical density is still low. The resulting scaling factors again agree well with a Lorentzian shaped absorption cross section. This technique fails however to predict the absolute peak density of the cloud as it does not give any information about the sub-level

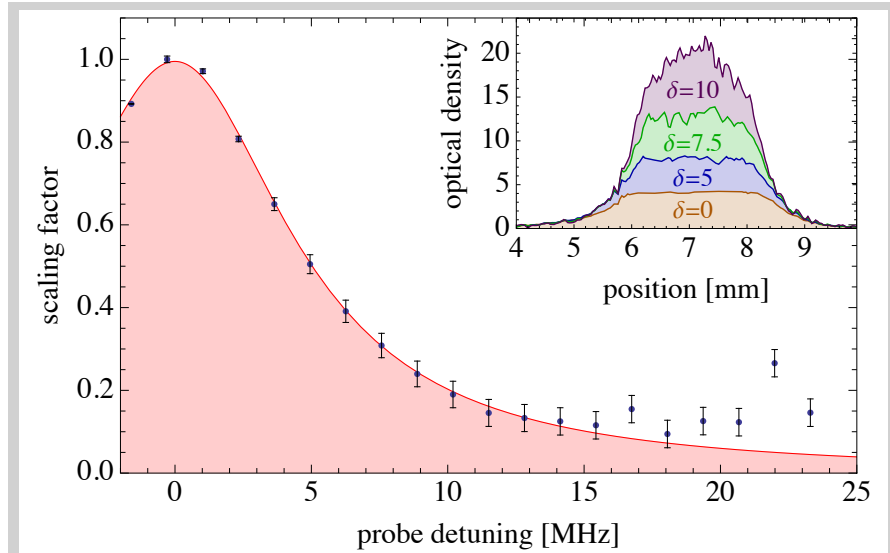


Figure 46: Scaled density distribution. In order to reconstruct the ions density distribution they are scaled to match on the outer flanks of low optical density

distribution. For clouds that can be optically pumped it can be a useful tool.

3.2.6 Optimization of the atom density

A detailed characterization of the Dark SPOT used in the HAITrap experiment can be found elsewhere [99]. The maximum achievable atom number and density of our setup is on the order of 1.5×10^9 atoms at a density of 3×10^{11} atoms/cm³. The loading time using the 2D MOT is approximately 350ms and the diameter of the fully loaded trap is $d \approx 1$ mm ($1/e$).

* Due to the 2:1 imaging used for the spot, the size of the hollow core at the position of the atom cloud exceeds the physical spot size by a factor of two.

We found that the spot-size of the small circular metal plate creating the hollow core of the repumping beam, does not strongly influence the achievable peak density. Varying the spot-size between 2mm and 5mm diameter* resulted in the same peak density, only the loading rate of the trap was slightly reduced for very large spot sizes. The other settings which led to the highest density are as follows.

- Cooling beam. A detuning of $\delta = 3.2\Gamma$ with a relatively low total power of $P = 20$ mW. The power was distributed over the three cooling beams with twice as much power in z-direction.
- Repump beams. The beams are on resonance with a total power of $P = 1.2$ mW equally distributed between the two beams. We found that it is also sufficient to use a single repumping beam, which results in a light distribution best described as a "Dark Sausage".

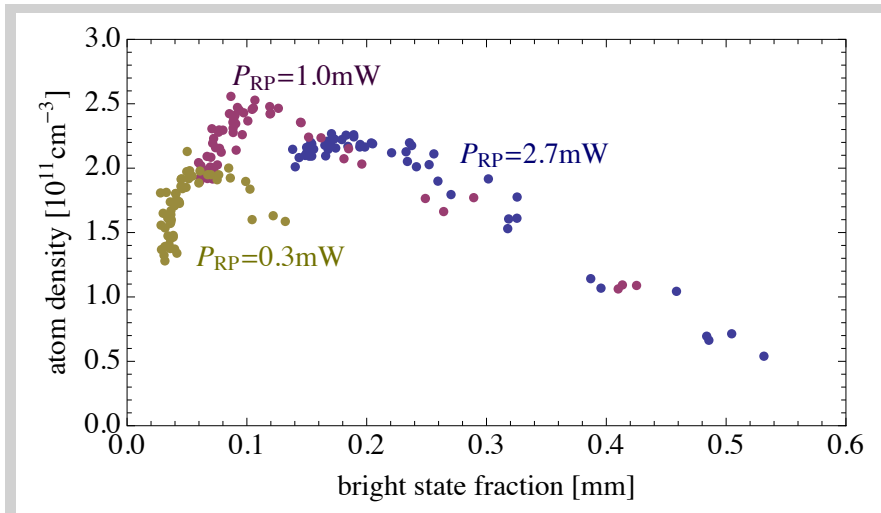


Figure 47: Peak atom density as a function of the bright state fraction. The bright state fraction was varied by changing the detuning of the cooling beam and the power of the repumping beam (as indicated by the different colors).

- Magnetic field gradient. The best result was obtained using the highest available field gradient of 30G/cm*.

Fig. 47 shows the achieved densities as a function of the bright state fraction. The bright state fraction denotes the fraction of the atoms is the cooling transition. For a normal magneto optical trap this fraction will be almost unity as all atoms falling into the dark state are constantly pumped back into the bright state by the repumper. As explained above, in a Dark SPOT a reduced bright state fraction results in a density increase by reducing trap losses. Experimentally the bright state fraction is determined by comparing the atom number with and without pumping all atoms into the bright state (see explanation of "fill-in" beam). The maximum density occurs at a bright state fraction of about 10% which agrees well with the theoretical prediction [130].

Fig. 47 also tells us that the bright state fraction can be efficiently reduced without strongly effecting the peak density of the cloud. This can be of particular interest for sympathetic cooling experiments where inelastic collisions should be reduced to a minimum.

* With our coils field gradients of up to 60G/cm can be created but the switch turning off the magnetic field prior to the imaging sequence cannot handle the required currents.

PHOTODETACHMENT OF OH⁻

This chapter is based on calculations performed in collaboration with A. Wolf from the Max-Planck Institute for nuclear physics. Some aspects of the setup for the photodetachment tomography have also been published in form of a master thesis [134].

Photodetachment describes the detachment process of the additional electron from an anion by absorption of a photon with energy E_γ [135]. The electron is excited into continuum and takes away the excess energy $E_\gamma - E_{ea}$ with E_{ea} being the electron affinity of the anion. Consequently, photodetachment is only possible for $E_\gamma > E_{ea}$. The resulting wavelength dependence of the photodetachment rate for an atomic anion is characterized by a single step at E_{ea} , the photodetachment threshold. Photodetachment spectroscopy on atomic anions has been used to measure their electron affinity.

For molecular anions, the situation becomes more complicated as the internal degrees of freedom influence the electron affinity. Internally excited molecules exhibit a lower photodetachment threshold as molecules in the ro-vibrational ground state. Therefore, the photodetachment spectrum of molecular anions is characterized by multiple thresholds which contain detailed information about the internal level-structure of the molecule.

Photodetachment of OH⁻ has been studied extensively in different experiments as well as theoretically. In this chapter we will first discuss the different theoretical challenges in describing photodetachment of OH⁻ which will lead to a theoretical model for the photodetachment spectrum. This model is then compared to the experimental results of different experiments and will be used to interpret the first photodetachment measurements performed in our HAITrap which enables us to estimate the ro-vibrational temperature of our ion cloud.

The last part of this chapter focuses on the determination of the ions motional temperature via photodetachment tomography. This technique is used to measure the density profile of the ions in the rf-trap [136, 137, 138]. Extracting the density profile of negative ions is a special challenge, as all direct optical methods fail due to the lack of any electronic transitions.

4.1 MOLECULAR STATES

In atomic systems the electronic state of the system is typically described by the quantum numbers S, L, J, M_J . These quantum numbers depend on the electron configuration of the atom. Every quantum number is based on a fundamental symmetry of the system. In linear molecules, the angular momentum quantum number L which is based on the spherical symmetry of the system, is no longer a good quantum number. In molecules there exist two different kinds of angular momentum, the electronic angular momentum L and the angular momentum from the rotation of the nuclei R . These two couple to the total angular momentum J which is then conserved.

In the special case of a molecule with closed shells (as in the case of OH⁻), the quantum numbers S and L are zero and the total angular momentum is given by $J = R$. For all other cases (like OH) one can make use of the fact that R only has a component perpendicular to the bond axis, e.g. the axis connecting the two nuclei which we choose to be the z -axis. Consequently, R does not have a z component which means that M_L is still a good quantum number (L_z is conserved). The fact that the energy of the system is independent of the direction of L_z is expressed in the quantum number

$$\Lambda = |M_L|. \quad (61)$$

Other quantum numbers which are commonly used for molecules are

$$\begin{aligned} \Sigma &= |M_S|, \\ \Omega &= \Sigma + \Lambda, \\ J_a &= L + S, \\ N &= J - S. \end{aligned} \quad (62)$$

4.1.1 Hund's coupling cases

The way, the coupling between the total angular momenta L, S and R is treated differs as their coupling strengths are different for different molecules. For diatomic molecules the different cases are called the five Hund's coupling cases [139, 140, 141].

- Hund's case (a). The strongest couplings are spin orbit coupling and the coupling of L to the bond axis through electrostatic forces. Consequently, the z -components of all angular momenta are good quantum numbers. The total angular momentum is given by $J = \Omega + R$. It is presumed that the precession of L and S around the bond axis is much faster than the nutation of R and Ω around J . In this case, the rotational energy operator is given by

$$H_{\text{rot}} = BR^2 = B(J - L - S)^2, \quad (63)$$

with $B \rightarrow$ rotational constant.

Good quantum numbers are: $\Lambda, \Sigma, \Omega, S, J$.

- Hund's case (b). If $\Lambda = 0$, the spin-orbit coupling vanishes and S is no longer coupled to the bond axis. The same is true for some very light molecules where Λ is non-zero, but spin-orbit coupling is very weak and L quickly precesses around the bond axis. In this case, Λ couples to R to form N and the total angular momentum arises from the coupling of N with S . The rotational energy operator is given by

$$H_{\text{rot}} = BR^2 = B(N - L)^2, \quad (64)$$

Good quantum numbers are: Λ, N, S, J .

- Hund's case (c). In this case, L and S are strongly coupled but they only show a weak coupling to the bond axis, which mainly occurs in heavy molecules. As a result, the z components of L and S are no longer conserved and the angular momentum $J_a = L + S$ is introduced which rapidly precesses around the bond axis. The z component of this combined angular momentum is Ω which then couples with R to the total angular momentum J . An example of this case is HeAr^+ [142] or I_2 [143].

Good quantum numbers are: J_a, Ω, J .

- Hund's case (d). The dominant coupling is between L and R which is much stronger than the coupling of L to the bond axis. In this case L and R couple to N which in turn couples with S to the total angular momentum J . Typical examples of this case are molecules excited to high Rydberg states [144, 145].

Good quantum numbers are: L, R, N, S, J .

- Hund's case (e). In this case L and S again couple to J_a which then couples with R to form J . This case is relatively rare, but it has been observed in some molecules such as HeKr^+ [146] or in certain Rydberg states [147].

Good quantum numbers are: J_a, R, J .

A stringent separation into a specific case is not always possible. Hund's cases (a) and (b) are by far the most common and most molecules exhibit an intermediate coupling between these two cases. This is also the case for OH which is why we will focus our discussion on this intermediate state.

4.1.2 Nomenclature of electronic states

In the following we will discuss transitions between different states of the OH anion and neutral. These states will be labeled using the quantum numbers of Hund's case (a) as

$$|\Lambda, \Sigma, \Omega, S, J\rangle = {}^{2S+1}\Lambda_{\Omega}. \quad (65)$$

Here, the sub- and superscripts are simply written out as numbers, whereas the quantum number $\Lambda = 0, 1, 2, 3, \dots$ is indicated by the capital greek letters $\Sigma, \Pi, \Delta, \Phi, \dots$. Sometimes an additional X can be found in front of this term symbol to indicate the electronic configuration of the ground state. For OH⁻ and OH this results in the following expressions.

- The ground state of OH⁻ has completely filled electron shells. Consequently, all electronic quantum numbers are zero. This is written as $X {}^1\Sigma^+$. In this case the quantum number Ω is not written out as it follows directly from $S = 0$ and $\Lambda = 0$. Instead the $+$ indicates that the state is symmetric under reflection through a plane containing the bond axis. This symmetry is only meaningful for Σ states, as for all states with $\Lambda > 0$ these two states are degenerate.
- The ground state of OH has one electron missing in its valence shell. The corresponding quantum numbers are $S = 1/2$, $\Sigma = 1/2$ and $\Lambda = 1$. The combined angular momentum Ω can therefore have the values $1/2$ or $3/2$. Consequently there are two possible states, namely $X {}^2\Pi_{1/2}$ and $X {}^2\Pi_{3/2}$, with the latter one being the energetically lower state due to the spin orbit coupling.

4.1.3 Ro-vibrational levels

Besides the electronic states, molecules have additional internal degrees of freedom. For diatomic molecules such as OH there are two additional degrees of freedom, namely one rotational and one vibrational.

4.1.3.1 Rigid rotator

The rotational levels of a molecule are commonly described by the rigid rotator. This means that the nuclei are treated as point masses and that the bond length between the cores does not vary due to the rotation. In this case, the energy of the rotation is simply given by $E_{\text{rot}} = \frac{1}{2}\mu r^2 \omega_{\text{vib}}^2$, with μ being the reduced mass of the nuclei and r being the bond length. In the quantum mechanical treatment this

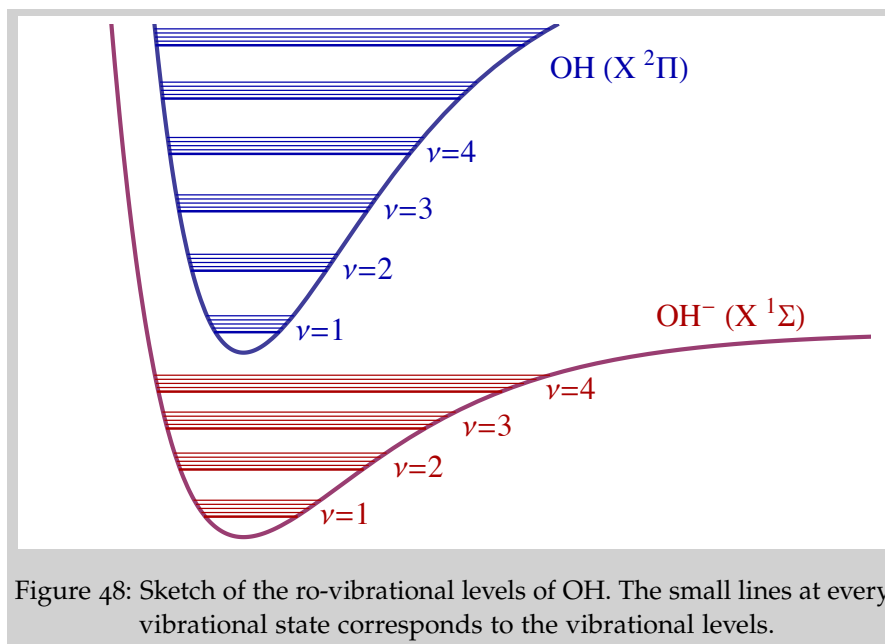


Figure 48: Sketch of the ro-vibrational levels of OH. The small lines at every vibrational state corresponds to the vibrational levels.

corresponds to the energy levels

$$E_{\text{rot}}(J) = \frac{h^2}{8\pi^2\mu r^2} J(J+1), \quad (66)$$

with h → Planck constant,
 with $J = 1, 2, 3, \dots$ → rotational quantum number.

4.1.3.2 Vibrational levels

For the derivation of the rotational levels we assumed a constant internuclear distance, which is not the nuclei as the cores can vibrate along the bond axis. Assuming that the vibration can be described by a harmonic potential $V = k(r - r_e)^2$, the energy levels are given by

$$E_{\text{vib}}(v) = h\nu_{\text{vib}}(v + 1/2), \quad (67)$$

with $\nu_{\text{vib}} = \frac{1}{2\pi} \sqrt{\frac{k}{\mu}}$ → vibration frequency,
 k → harmonic force constant,
 r_e → equilibrium distance of cores,
 $v = 0, 1, 2, \dots$ → vibrational quantum number.

The assumption of a harmonic potential means that on the one hand the nuclei can move infinitely close together and fails to describe bond breaking if the internuclear distance becomes very large. It is therefore only a good description for small displacements near

the equilibrium distance. For larger displacements, different non-harmonic potentials can be used. One of the most common choices is the potential introduced by Morse [148]

$$V_{\text{Morse}}(r) = D_e (1 - \exp[-\beta(r - r_e)])^2, \quad (68)$$

with $D_e \rightarrow$ dissociation energy.

The Morse potential fixes both of the aforementioned problems. At very small internuclear distances, the energy diverges and at large distances the potential levels resulting in the dissociation energy D_e beyond which the bond between the nuclei breaks.

4.1.4 *Ro-vibrational spectrum of OH⁻ and OH*

In homonuclear molecules the center of the positive and negative charges coincide resulting in a vanishing permanent dipole moment. For heteronuclear molecules such as OH however, this is not the case resulting in a non-zero permanent electric dipole. This dipole moves with the rotation and vibration frequencies which are given by the so called rotational and vibrational terms

$$F(J) = \frac{E_{\text{rot}}}{hc} = B_0 J(J+1) - D_0 J^2(J+1)^2 + \dots, \quad (69)$$

$$G(v) = \frac{E_{\text{vib}}}{hc} = \omega_{\text{vib}}(v + 1/2) - \chi_{\text{vib}} \omega_{\text{vib}}(v + 1/2)^2 + \dots, \quad (70)$$

with $c \rightarrow$ speed of light,
 $D_0 \rightarrow$ centrifugal distortion correction,
 $\omega_{\text{vib}} = \frac{1}{2\pi c} \sqrt{\frac{k}{\mu}} \rightarrow$ vibrational constant,
 $\chi_e \omega_{\text{vib}} \rightarrow$ 2nd order vibrational constant.

Here we included second order corrections for the rotational as well as the vibrational energy. In case of the vibrational energy the correction term arises from the anharmonicity of the internuclear potential, as discussed above. The correction of the rotational energy is based on the so called centrifugal distortion. This accounts for the fact that the bond distance increases for large rotational quantum numbers due to the centrifugal force. There exist also higher order correction terms which we will neglect as they only become relevant for highly excited ro-vibrational states.

For OH⁻ the ro-vibrational level structure is given by the sum of equations (69) and (70). In the electronic ground state, the vibrational constants are $\omega_{\text{vib}} = 3809\text{cm}^{-1}$ and $\chi_{\text{vib}} \omega_{\text{vib}} = 94\text{cm}^{-1}$ [159]. The rotational constants are summarized in Table 4. In case of OH the vibrational terms are calculated in the same fashion with $\omega_{\text{vib}} = 3735.2\text{cm}^{-1}$ and $\chi_{\text{vib}} \omega_{\text{vib}} = 82.8\text{cm}^{-1}$ [150]. The rotational level structure is a

ref	A_{ea}	B_0	$10^3 \times D_0$
OH			
[149]	14723(15)	—	—
[150]	—	18.871	1.865
[151]	14740.9824(91)	18.7354(16)	1.982(79)
[152]	14741.03(17)	18.7409(45)	2.052(45)
[153]	—	18.73503(36)	1.9791(56)
[154]	14741.02(3)	18.732(3)	—
[155]	—	18.75(15)	—
OH ⁻			
[156]	—	18.87(7)	—
[157]	—	16.9274	2.0497
[158]	—	18.5310	1.908

Table 4: Rotational constants and electron affinity of OH and OH⁻.

bit more complicated however. In contrast to OH⁻, the neutral OH molecule has an orbital angular momentum and a spin which couple to the rotational angular momentum. As we have explained before, the set of quantum numbers best describing the state of the molecule differs for different molecules or even for different states of the same molecule. In case of OH, the lowest rotational states exhibit intermediate spin-orbit coupling and are best described by Hund's case (a). For large rotational angular momentum however, the spin orbit coupling becomes less relevant and the states are best characterized by the quantum number N of Hund's case (b). Consequently, the vibrational energy is either given by Eq. (63) for Hund's case (a) or Eq. (64) for Hund's case (b). It is also possible to derive an expression for the rotational spectrum of the intermediate state [160, 161]

$$F_{OH}(J) = B_0 [(J + 1/2)^2 - \Lambda^2 + X] - D_0(J + 1)^4 \pm \Delta\nu_{fe} \quad (71)$$

with $\lambda = A/B_0$
 $X = \sqrt{(J + 1/2)^2 + \lambda(\lambda/4 - 1)\Lambda^2}$
 $A \rightarrow$ spin orbit coupling constant,
 $\Delta\nu_{fe} \rightarrow$ Λ -doubling.

The last term, known as lambda doubling, lifts the degeneracy of the Λ states. We have claimed at the beginning of this chapter, that the energy of the system does not depend on the orientation of L_z which is why the quantum number Λ only takes into account the absolute value of L_z . However, this is only perfectly true if the molecule has no rotational angular momentum ($R = 0$). For $R \neq 0$ the degeneracy is lifted by the coupling of the electronic and nuclear motion and it has to be differentiated between two different cases which correspond to precessions of L around the bond axis with opposite sense. We will

denote these two states with $\pm\Lambda$. The splitting of the $\pm\Lambda$ states can be calculated by [162]

$$\Delta v_{\text{fe}} = \left[\frac{p+2q}{2} \left(\pm 1 + \frac{2-Y}{X} \right) + \frac{2q}{X} (J-1/2)(J+3/2) \right] (J+1/2) \quad (72)$$

with $p, q \rightarrow$ lambda doubling parameters.

For the vibrational ground state of OH ($X^2\Pi_{\Omega}$) the lambda doubling parameters are given by $p = 0.23521$ and $q = -0.038678$ [163]. Fig. 49 shows the resulting level scheme of OH and OH⁻ including the splitting of the $\pm\Lambda$ states which has been exaggerated by a factor of one hundred as it would not be visible otherwise. Also indicated are the total angular momentum J and the parity of each state. The two states of a Λ doublet always have opposite parity. It should also be noted, that for the higher rotational states, the shown quantum numbers lose their meaning and the states would be better sorted by their quantum number N instead. This is indicated by the fact that the states with equal N approach each other with growing angular momentum.

4.2 PHOTODETACHMENT OF OH⁻

Transitions from one molecular state to another obey selection rules which limit the possible changes of the relevant quantum numbers. In diatomic molecules described by Hund's case (a), electric dipole transitions obey the following rules

- $\Delta\Lambda = 0, \pm 1,$
- $\Delta S = 0,$
- $\Delta J = 0, \pm 1$ (except $\Sigma \rightarrow \Sigma, \Delta J = \pm 1$),
- parity inverts.

In the following we will derive the wavelengths and relative transition strengths of all possible photodetachment transitions of OH⁻. Based on this we will derive the wavelength dependence of the total photodetachment cross section which we will compare to previous measurements.

4.2.1 Possible transitions

The entire discussion will focus on electric dipole transitions close to the photodetachment threshold. We also assume that the OH⁻ molecule is in the electronic and vibrational ground state with total angular momentum J'' . In the following we will denote this state with

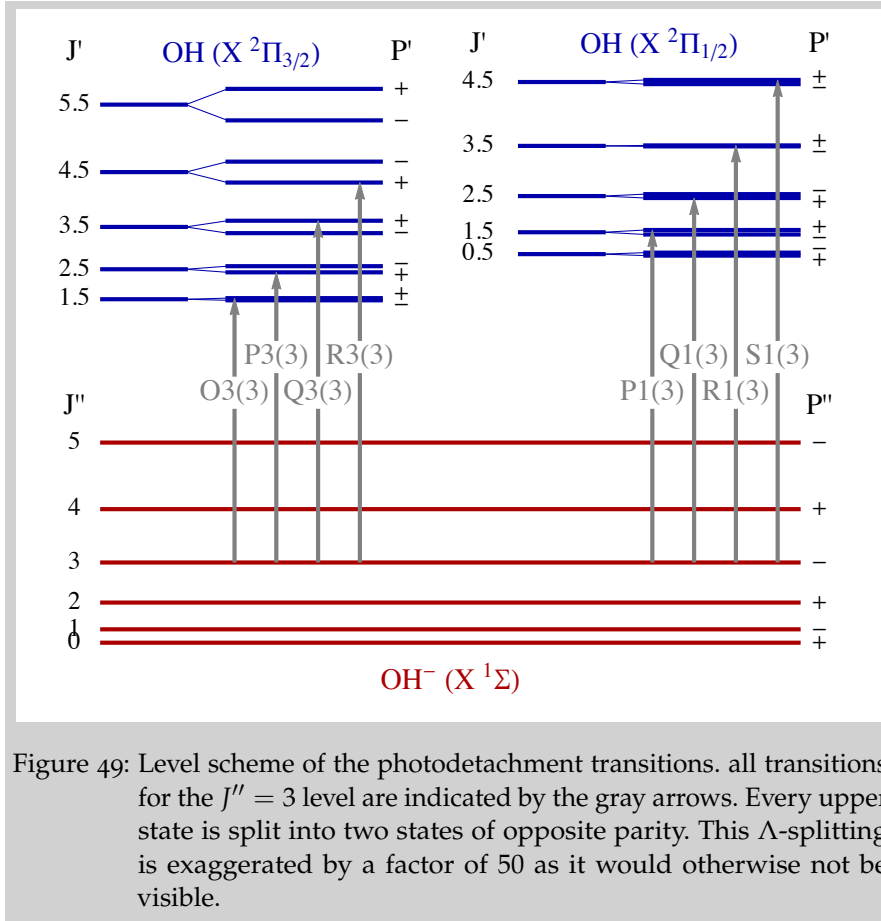


Figure 49: Level scheme of the photodetachment transitions. all transitions for the $J'' = 3$ level are indicated by the gray arrows. Every upper state is split into two states of opposite parity. This Λ -splitting is exaggerated by a factor of 50 as it would otherwise not be visible.

$|^1\Sigma, J''\rangle$. The photodetachment process is best described as a two step process [144].

- First, by absorption of a photon, the molecule is excited into an intermediate $^1\Pi$ state of opposite parity with angular momentum $J_i = J'' + \Delta J_i$. According to the selection rules introduced earlier only transitions with $\Delta J = 0, \pm 1$ are allowed. The resulting state will denote this state with $|^1\Pi, J_i\rangle$.
- Second, the electron detaches from the molecule resulting in the final state $\text{OH}(X \ ^2\Pi_\Omega) + e^-$. We will denote this state with $|^2\Pi_\Omega, J'; l, s\rangle$, with l and $s = 1/2$ denoting the angular momentum and spin of the detached electron. The angular momentum of the final state is given by $J' = J'' + \Delta J_i \pm l \pm s$.

Close to the photodetachment threshold, the departing electron has a very small kinetic energy. This limits the electrons angular momentum, as a large l corresponds to a large centrifugal barrier, hindering the electron to depart from the molecule. It is therefore save to assume that in the energy range discussed here, only s-wave ($l = 0$) contributions has to be considered. This was also shown experimentally [152]. Only far above threshold, additional d-wave contributions have been observed [164, 155].

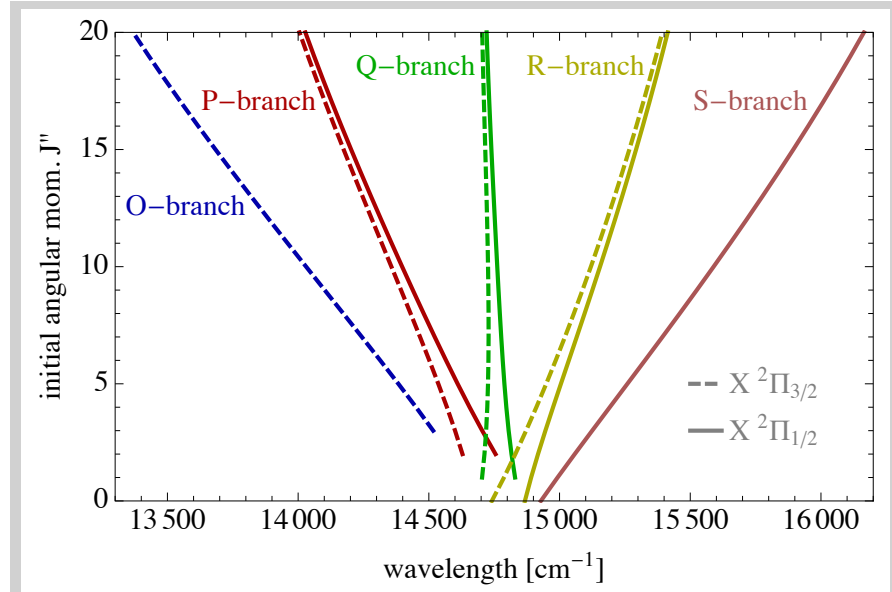


Figure 50: Wavelength dependence of the transition branches. The transitions to the ${}^2\Pi_{1/2}/{}^2\Pi_{3/2}$ states correspond to the solid/dashed lines.

The possible angular momenta of the final state are therefore given by $J'' - J' = \pm 3/2, \pm 1/2$.

Fig. 49 shows all possible transitions starting from $|{}^1\Sigma, J'' = 3\rangle$. The transitions are grouped into different branches as indicated by the labels in the figure. Every branch corresponds to a specific change of the quantum number N with the symbols O, P, Q, R, S corresponding $\Delta N = -2, -1, 0, 1, 2$. Moreover the transitions are labeled with two numbers. The first number encodes the final state of the transition with 1 corresponding to OH($X {}^2\Pi_{1/2}$) and 3 corresponding to OH($X {}^2\Pi_{3/2}$). The number in parenthesis indicates the angular momentum of the initial state.

This means that the transitions are labeled using the quantum numbers of Hund's case (b) whereas the term symbols of the OH states refer to Hund's case (a). Consequently, for transitions with small initial angular momentum J'' the term value of the upper state determines the transition frequency whereas for large J'' the transition frequency mainly depends on the branch. This is illustrated in Fig. 50 which shows the wavelength dependence of the different branches.

We now want to investigate the full photodetachment spectrum of OH⁻. The transition frequencies are given by the energy difference of the final and initial states

$$\nu_{\text{PD}}(J'' \rightarrow J') = A_e + F(J'') - F_{\text{im}}(J') \quad (73)$$

with	$F(J'')$	\rightarrow	rotational term of OH ⁻ (Eq. (69)),
	$F_{\text{OH}}(J')$	\rightarrow	rotational term of OH (Eq. (71)),
	A_e	\rightarrow	electron affinity of OH (Table 4),

The angular momenta J' and J'' have to obey the selection rules discussed above. In total there are three transitions from $J'' = 0$, five from $J'' = 1$, seven from $J'' = 2$ and eight from all initial states $J'' \geq 3$. The wavelengths of the lowest transitions are summarized in Table 5. In order to verify our calculations, we have compared the calculated energy levels of OH with the ones listed in the HITRAN database [165, 166], which shows very good agreement.

4.2.2 Transition intensities

In order to calculate the wavelength dependence of the photodetachment cross section, all transitions have to be weighted with their relative transition intensities. Based on the energy spectrum calculated by Van Fleck [161], Dousmanis *et al.* [167] was the first one to theoretically describe the photodetachment spectrum of OH⁻. The frame-transformation method we are using in the following was first applied to describe photodetachment of negative ions by Rau and Fano [168]. Since then it has been used to interpret many experimental results [169, 149, 170, 152, 171, 151] and was specifically adapted to describe group-VI-hydroxide anions such as OH⁻ [172, 173]. The amplitude of a transition is expressed by the matrix element of the two step process explained previously. The intensity can be written as

$$I \propto \left| \sum_{J_i} \langle {}^2\Pi_{\Omega}, J'; l, s | {}^1\Pi, J_i \rangle \langle {}^1\Pi, J_i | z | {}^1\Sigma, J'' \rangle \right|^2 \quad (74)$$

The second factor describes the excitation of the molecule into the intermediate state which is equivalent to the Hönl-London factor. The first factor describes the subsequent decay into a jj-coupled electron-neutral system. The sum is performed over all intermediate states that can link the initial to the final state of the molecule. It was shown by Schulz *et al.* [173] that as a consequence of the Wigner-Eckhard theorem it is also correct to take the sum of the squared values rather than squaring the sum itself. Using this simplification it is possible to derive a simple analytic expression for the transition intensities.

In Eq. (74) we have expressed the final state in terms of Hund's case (a). As pointed out before, the OH molecule is only properly described by the intermediate state between the cases (a) and (b). Using the wave functions of the intermediate state $|u_{\alpha} J'\rangle$, the transition intensity can

#	branch	J''	J'	wavenumber [cm ⁻¹]	intensity
1	R1(0)	0	0.5	14867.5	0.67
2	R3(0)	0	1.5	14741.	0.78
3	S1(0)	0	1.5	14928.5	0.55
4	Q1(1)	1	0.5	14829.8	1.
5	Q3(1)	1	1.5	14703.7	1.67
6	R1(1)	1	1.5	14891.3	1.53
7	R3(1)	1	2.5	14787.4	0.72
8	S1(1)	1	2.5	14992.4	1.08
9	P1(2)	2	0.5	14755.1	0.33
10	P3(2)	2	1.5	14628.7	1.22
11	Q1(2)	2	1.5	14816.2	1.45
12	Q3(2)	2	2.5	14712.8	2.23
13	R1(2)	2	2.5	14917.7	2.48
14	R3(2)	2	3.5	14830.8	0.67
15	S1(2)	2	3.5	15058.	1.62
16	O3(3)	3	1.5	14516.5	0.57
17	P1(3)	3	1.5	14704.2	0.43
18	P3(3)	3	2.5	14600.3	2.28
19	Q1(3)	3	2.5	14805.3	1.92
20	Q3(3)	3	3.5	14719.2	2.74
21	R1(3)	3	3.5	14945.9	3.48
22	R3(3)	3	4.5	14872.	0.61
23	S1(3)	3	4.5	15124.8	2.17
24	O3(4)	4	2.5	14451.2	1.04
25	P1(4)	4	2.5	14656.	0.46
26	P3(4)	4	3.5	14569.2	3.33
27	Q1(4)	4	3.5	14796.4	2.38
28	Q3(4)	4	4.5	14723.6	3.22
29	R1(4)	4	4.5	14975.2	4.5
30	R3(4)	4	5.5	14911.3	0.55
31	S1(4)	4	5.5	15192.1	2.72
32	O3(5)	5	3.5	14383.4	1.54
33	P1(5)	5	3.5	14610.1	0.46
34	P3(5)	5	4.5	14536.2	4.39
35	Q1(5)	5	4.5	14789.	2.83
36	Q3(5)	5	5.5	14726.4	3.7
37	R1(5)	5	5.5	15005.2	5.54
38	R3(5)	5	6.5	14949.	0.5
39	S1(5)	5	6.5	15259.6	3.27

Table 5: Transition wavenumbers and intensities.

be rewritten by projecting the intermediate states onto the case (a) state

$$I \propto \left| \sum_{J_i} \sum_{\Omega} \langle u_{\alpha} J' | {}^2\Pi_{\Omega}, J'; l, s \rangle \langle {}^2\Pi_{\Omega}, J'; l, s | {}^1\Pi, J_i \rangle \langle {}^1\Pi, J_i | z | {}^1\Sigma, J'' \rangle \right|^2. \quad (75)$$

As we are interested in the transition intensities from the ¹Σ states to the ²Π_Ω states, we have to express the wave functions in terms of the cases (a) wavefunction [167]

$$\begin{aligned} |u_{\alpha} J'\rangle &= C_1 |{}^2\Pi_{1/2}, J'; l, s\rangle + C_2 |{}^2\Pi_{3/2}, J'; l, s\rangle \\ \text{with } C_1 &= \sqrt{\frac{X-2+\lambda}{2X}}, \quad C_2 = \sqrt{\frac{X+2-\lambda}{2X}} \quad (\text{for } {}^2\Pi_{3/2}) \\ C_1 &= \sqrt{\frac{X+2-\lambda}{2X}}, \quad C_2 = -\sqrt{\frac{X-2+\lambda}{2X}} \quad (\text{for } {}^2\Pi_{1/2}) \end{aligned} \quad (76)$$

Plugging this expression into Eq. (75) the final transition intensities are obtained. For the ¹Σ → ²Π_Ω transition these can be expressed as [172, 173, 151]

$$\begin{aligned} I &\propto \frac{J''+2}{4J''+6} \left[-C_1 \sqrt{J''+1} + C_2 \sqrt{J''+3} \right]^2 \quad (\Delta J = -3/2) \\ I &\propto \frac{J''+2}{4J''+6} \left[C_1 \sqrt{J''+2} + C_2 \sqrt{J''} \right]^2 + \\ &\quad + \frac{1}{2} \left[-C_1 \sqrt{J''} + C_2 \sqrt{J''+2} \right]^2 \quad (\Delta J = -1/2) \\ I &\propto \frac{J''-1}{4J''-2} \left[-C_1 \sqrt{J''-1} + C_2 \sqrt{J''+1} \right]^2 + \\ &\quad + \frac{1}{2} \left[C_1 \sqrt{J''+1} + C_2 \sqrt{J''-1} \right]^2 \quad (\Delta J = 1/2) \\ I &\propto \frac{J''-1}{4J''-2} \left[C_1 \sqrt{J''} + C_2 \sqrt{J''-2} \right]^2 \quad (\Delta J = 3/2) \end{aligned} \quad (77)$$

The calculated transition intensities for the lowest transitions are shown in Table 5.

4.2.3 Threshold behavior

So far we have derived the positions and intensities of all possible photodetachment transitions. The last remaining question is how the detachment cross section scales with the photon energy.

Wigner [174] showed that the cross section dependence of a process resulting in two product particles only depends on the long-range forces between the two particles. In case of photodetachment of an

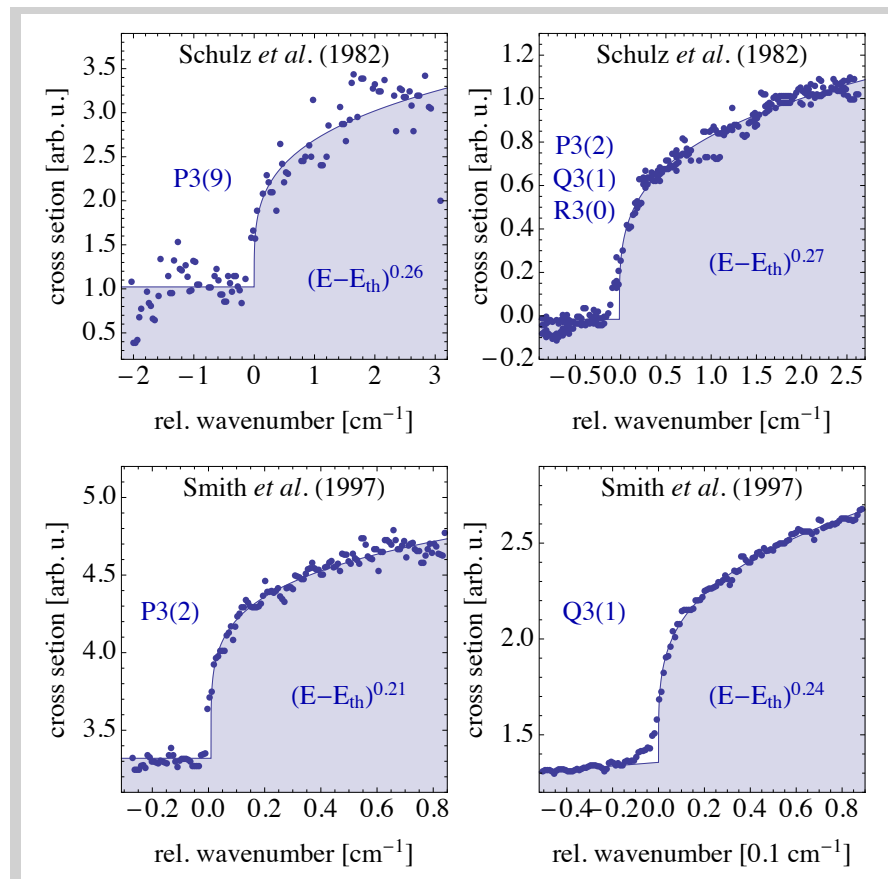


Figure 51: Threshold behavior of different OH^- photodetachment transitions. The presented data was numerically extracted from the figures of the corresponding publications [152, 154]. The solid curves are fitted threshold laws.

anion, the potential between the electron and the neutral falls off faster than r^{-2} at least as long as electron-dipole interactions can be neglected. For this case the Wigner-law predicts a scaling of the cross section near threshold of $\sigma_{\text{pd}} \propto E^{l+1/2}$, with l being the lowest possible angular momentum of the electron, as the centrifugal barrier suppresses contributions of higher partial waves close to threshold. Consequently, from the Wigner-law we would expect a $E^{1/2}$ scaling for the threshold behavior of OH^- .

The Wigner-law was later extended by Malley [175] to include an additional $V(r) = \text{const}/r^2$ potential accounting for the electron-dipole interaction. In this case the threshold behavior is given by $E^{1/2-(l-1/2)^2-\text{const}}$. Even though most heteronuclear molecules have a non-negligible internal electric dipole moment, it usually does not affect the departing electron, as it is rapidly rotating. However, it has been pointed out [176, 152] that as the departing electron affects the energy levels of the molecule, it can lead to a mixing of neighboring molecular states. Close to the threshold, the energy of the electron

is too low to lead to a mixing of different rotational states. At larger energies however, the near-degenerate $\pm\Lambda$ are perfect candidates for such kind of mixing. When the electron energy exceeds the lambda splitting energy, first order mixing can occur [152]. As the two lambda states have opposite parity this induces an dipole which dominates the long-range interaction between the electron and the neutral molecule. This effect was studied by Engelking [176] in more detail, who found that the threshold scaling E^x also depends on the final state of the molecule. For the lowest rotational states of OH a simple model was used predicting exponents of $x = 0.4, 0.48, 0.49, 0.495$ for the ${}^2\Pi_{1/2}$ states with $J' = 0.5, 1.5, 2.5, 3.5$ and $x = 0.28, 0.425, 0.46$ for the ${}^2\Pi_{3/2}$ states with $J' = 1.5, 2.5, 3.5$. It seems that these exponent approach the exponent $x = 1/2$ predicted by the Wigner-law for higher rotational states. Unfortunately these exponents should only be valid very close to threshold. Similar methods have also been applied to larger molecules with more complicated orbitals [177] predicting scaling laws with energy dependent exponents.

Experimentally the threshold behavior has been investigated by fitting measured cross sections with different scaling functions. In the first experimental measurement of the OH^- photodetachment cross section, the threshold behavior was considered to be a simple step function [156]. In subsequent investigations which were able to resolve single thresholds, the thresholds were fitted using different scaling laws. For atomic anions like S^- [169], which should exhibit a simple Wigner-law at threshold, the expected scaling of $E^{-1/2}$ was confirmed. In molecular anions, which are subject to the previously discussed effects, many different scaling behaviors have been found. Steiner *et al.* [178] found first deviations from the Wigner-law in SH^- and used a $(E^{1/2} + aE)$ scaling law to fit the measured data. Hotop *et al.* [149] were the first ones to resolve single thresholds for OH^- and concluded that their data was best described by a $E^{1/4}$ scaling. Later, also the theoretically predicted dependence of the threshold behavior on the final state of the molecule was observed [154].

Unfortunately, both the theoretical and experimental results still do not allow a satisfying description of all threshold scaling laws. Fig. 51 shows a selection of published threshold scalings. From the fitted scaling laws we can conclude that an exponent of $x \approx 1/4$ agrees well with all experimental data. In the following we will therefore use this scaling in our model.

4.3 PHOTODETACHMENT SPECTROSCOPY

We now have all the required information to calculate the energy dependence of the photodetachment cross section. The total cross section at a given photon energy E_γ is composed of the cross sections of all transitions with a threshold $E_n < E_\gamma$, with E_n denoting the

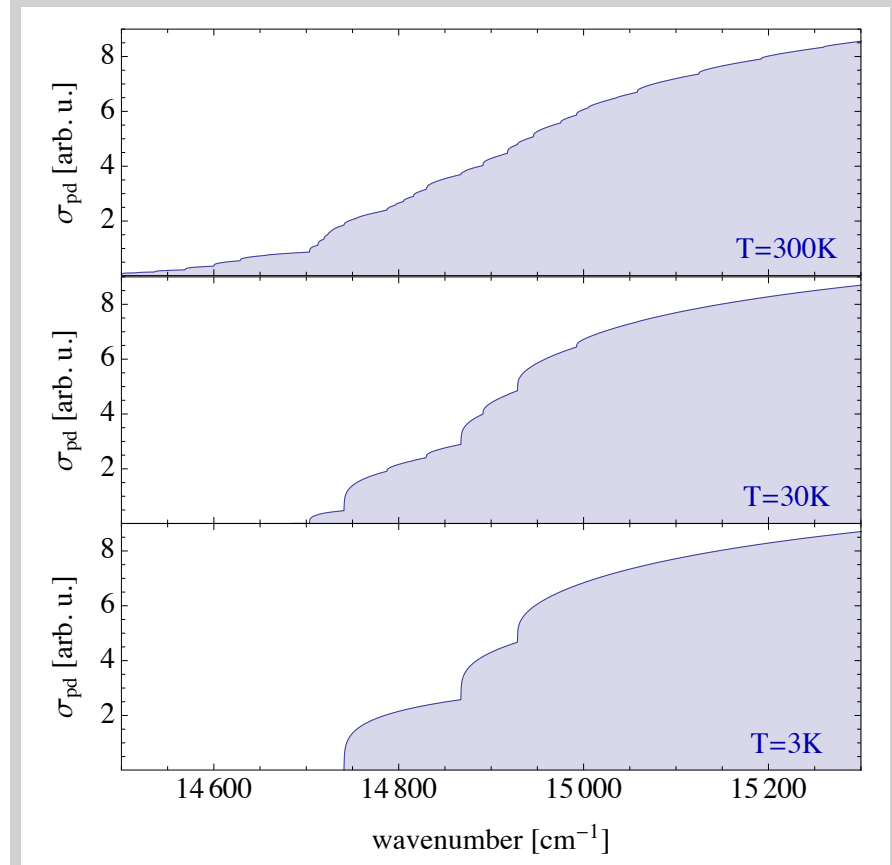


Figure 52: Calculated Photodetachment spectrum of OH⁻ for three different temperatures. The relatively flat part of the 300K-spectrum below 14700cm⁻¹ corresponds to the O- and P-branches. The steep rise that follows marks the onset of the Q-branch where all the transitions have similar wavenumbers.

threshold energy of the n 'th transition. The labeling n of the transitions is completely arbitrary and in the following we will number the transitions starting with the lowest J'' states (see Table 5). The total cross section can be written as

$$\sigma_{\text{pd}}(E_\gamma) \propto \sum_{n, E_n > E_\gamma} p_n(J'') \frac{I_n}{2J'' + 1} (E_\gamma - E_n)^{x_n} \left(\frac{E_\gamma}{E_n} \right)^{-2} \quad (78)$$

with I_n → rel. intensity of n 'th transition,
 x_n → threshold exponent of n 'th transition,
 $p_n(J'')$ → relative population of the J'' -state.

The first factor accounts for the initial rotational state population of the OH⁻ molecules. If the measurement is performed on a thermal gas with temperature T , the state population is simply given by a Maxwell-Boltzmann distribution. The second factor is the relative intensity of the transition. The third factor is the threshold law discussed above and the last factor accounts for the fact, that the cross section

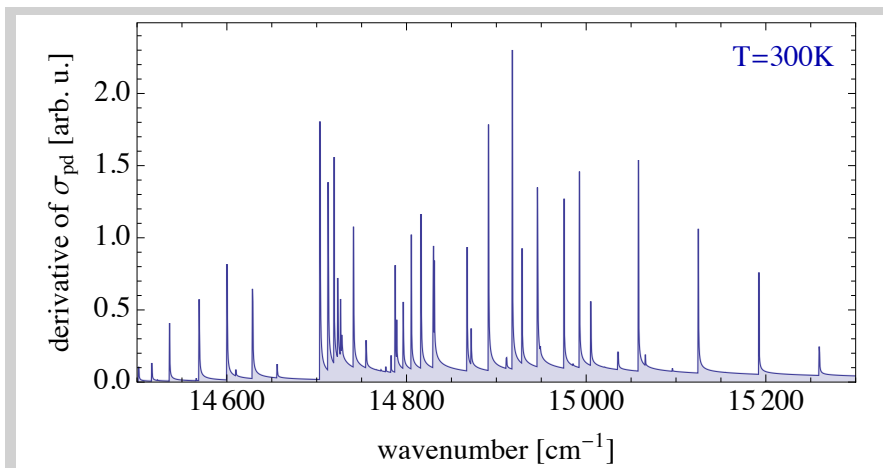


Figure 53: Derivative of the photodetachment spectrum. For every threshold there is a sharp peak in the spectrum, as the new channel opens up.

again decreases for energies far beyond the threshold. Fig. 52 shows the resulting wavelength dependence of the total photodetachment cross section for three different temperatures. From the cross section dependence, the different thresholds are clearly distinguishable. For the lowest temperature only the $J'' = 0$ level has a non-negligible population resulting in three steps for the three possible transitions. In case of $T = 30K$, the $J'' = 1$ is populated resulting in a total of eight steps. Finally at room temperature, a lot of J'' levels contribute to the total cross section and at this resolution it becomes difficult to tell the single steps apart. In this case it is preferable to examine the derivative of the cross section which features a sharp peak at the position of every transition threshold. Fig. 53 shows the derivative of the cross section for $T = 300K$.

4.3.1 Comparison with previous experimental data

There have been different experimental studies measuring the wavelength dependence of the OH^- photodetachment cross section. We will now compare the calculated cross sections to experimental data of some of these studies. Fig 54 shows different curves which were calculated with our theoretical model and fitted to the experimental data. The theoretical curves show an overall good agreement with the data, nicely reproducing the main features. In case of the measurements by Hotop *et al.* [149] and Schulz *et al.* [152] there is a significant discrepancy with the theory close to the onset of the Q-branch. A possible explanation might be a non-thermal energy distribution of the ion cloud. In our model we assumed a rotational state distribution matching a Maxwell-Boltzmann distribution with the only remaining free parameter being the rotational temperature of the ions. The mea-

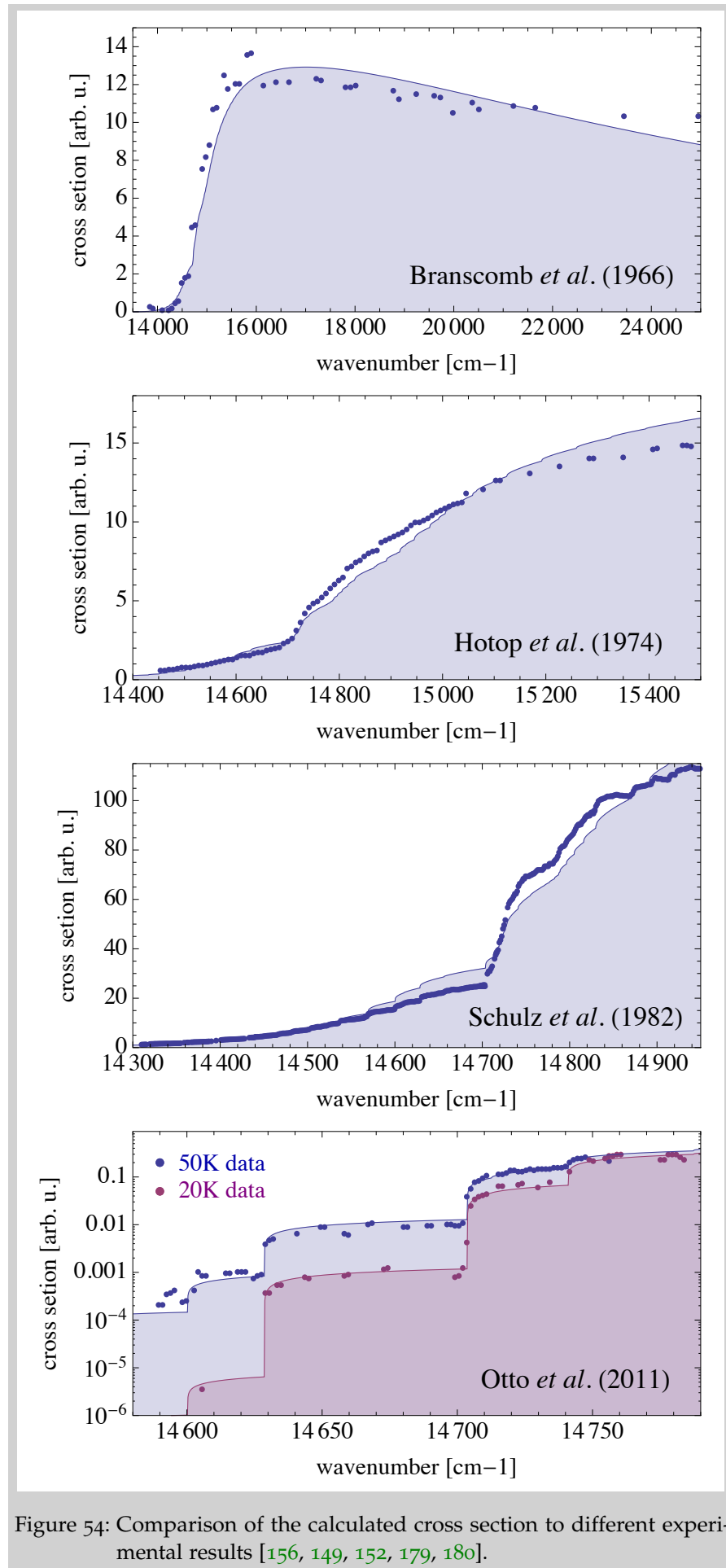


Figure 54: Comparison of the calculated cross section to different experimental results [156, 149, 152, 179, 180].

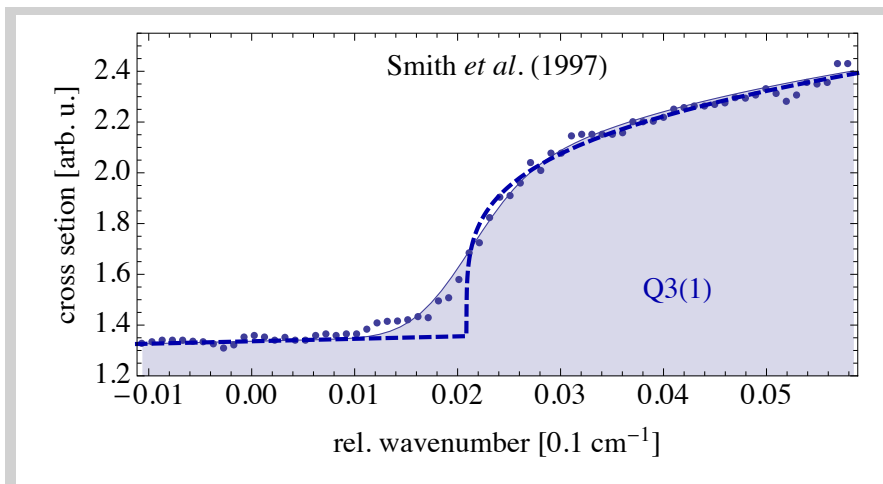


Figure 55: Doppler broadening of the photodetachment threshold. The shown data is the same as the one in Fig. 51. The dashed line corresponds to the threshold behavior at $T = 0$.

measurements of Hotop *et al.* and Schulz *et al.* were performed with ion beams which are not expected to exhibit a thermal energy distribution.

In the experiment by Otto *et al.* [179, 180] the measurement was performed with ions in a cryogenic ion trap. In this case, the theoretical curve shows much better agreement with experimental data which indicates a thermal ion sample. By fitting the data with our model, we obtain rotational temperatures of $T = 50\text{K}$ and $T = 28\text{K}$ for the two data sets which agrees reasonably with the temperature of the cryogenic trap ($T = 50\text{K}$ and 20K). The temperatures calculated by Otto *et al.* slightly differ from these values. This can be explained by the fact that they did not take into account the $P_3(3)$ transition close to 14600cm^{-1} which slightly influences the fit result.

4.3.2 Determination of the translational energy

Photodetachment spectroscopy can also be used as a tool to measure the translational temperature of an ion cloud. Fig. 55 shows a high resolution measurement of the $Q_3(1)$ transition [154]. The dashed line corresponds to the scaling law as introduced in Fig. 51, whereas the solid line shows the same curve assuming an ions' motional temperature of $T \approx 18\text{K}$. This temperature leads to a Doppler-broadening of the threshold. It should be noted that only the velocity component aligned with the propagation direction of the laser contributes to this broadening. For the data shown in Fig. 55 this corresponds to the velocity spread of the used ion beam. Performing similar measurements on the ion cloud in the HAITrap can be used to determine the ions motional as well as rotational temperature.

4.4 PHOTODETACHMENT IN THE HAITRAP

In the HAITrap we have performed first photodetachment measurements, characterizing the motional as well as rotational temperature of the ion cloud.

4.4.1 Detachment laser

In order to measure the photodetachment spectrum of the OH⁻ ions in the HAITrap, a tunable dye-laser [181] is used. This laser uses a high-pressure jet of iso-propanol which serves as a solvent for the dye, in our case pyridine I. By optically pumping the pyridine I molecules using a 10W Ti:Sapphire laser they emit light in the range from 630 up to 670nm.

The point at which the dye molecules are pumped is placed at the center of a laser cavity and serves as the gain medium of the laser. In order to control the frequency of the laser, four additional frequency selective elements are placed inside the laser cavity. Sorted by their free spectral range in ascending order, all frequency selective elements are

- the main laser cavity. With a total length of $L \approx 2\text{m}$, the free spectral range is $\Delta\nu_0 = c/(2L) \approx 150\text{MHz}$, with c being the speed of light.
- A thick etalon consisting of a 10mm prism with a free spectral range of $\Delta\nu_1 \approx 10\text{GHz}$.
- A thin etalon. It consists of a 0.5mm plate ($\Delta\nu_2 \approx 200\text{GHz}$) mounted on a galvanometer allowing to rotate the plate. This allows to scan the laser over a range of 40GHz.
- A birefringent filter. The filter consists of three birefringent plates which have relative thicknesses of 1:2:4 and are mounted in series at the Brewster angle. With this setup, the free spectral range of $\Delta\nu_3 \approx 1\text{THz}$ is set by the thickness of the thinnest plate, whereas the width of the transmission peaks is defined by the thickest plate.

The product of the transmission curves of all these elements together with the gain curve of the dye, defines the wavelength of the laser which corresponds to the single mode with the largest gain. A tuning of the output wavelength is achieved by shifting the transmission curve of single elements. For the birefringent filter and the thin etalon, this can be done manually. The thick etalon and the laser cavity however are too sensitive for manual adjustment and are controlled electronically. Both elements are locked to a high-stable reference cavity with a free spectral range of 1GHz. By dividing the transmission

signal of the cavity by the signal of a reference beam, an power independent transmission signal is obtained which is used to lock the laser to one side of a cavity fringe. Therefor, the signal is split into a high- and low-frequency part, with the high frequency part controlling a piezo controlled mirror which is part of the laser cavity and the low-frequency part is used to rotate the thick etalon.

The maximum output power of the laser is on the order of 1W at a wavelength of 340nm. Behind the laser the beam passes a double-pass AOM setup which is used to turn the light on and off. A small fraction of the light is coupled into a fiber connected to a high precision spectrometer (accuracy of 50MHz), whereas the main fraction of the light is coupled into a fiber going to the HAITrap experiment. There, the beam is focused to the center of the ion trap using the lens inside the fiber collimator. Between the vacuum chamber and the collimator a small fraction of the light is reflected onto a photodiode using a 1:100 beam splitter. The signals of the photodiode as well as the spectrometer are recorded to monitor the laser power and wavelength.

Additionally the entire setup in front of the chamber is placed on two translation stages which allow to scan the beam position over the entire ion trap. This can be used to determine the ions density distribution inside the trap by photodetachment tomography which will be explained in the following.

4.4.2 Photodetachment cross section

In the previous section the wavelength dependence of the detachment cross section was discussed in terms of a relative photodetachment cross section. In order to measure absolute cross sections, the power of the detachment laser as well as the relative overlap between the laser beam and the atom cloud has to be well known. The loss of ions dN over a time interval dt can be expressed as [179]

$$\frac{dN}{dt} = -N \left[R_0 + \sigma_{pd} \iiint E_\gamma(x, y) p_i(x, y, z) dx dy dz \right], \quad (79)$$

with	R_0	\rightarrow	loss rate due to limited trap time of ions,
	σ_{pd}	\rightarrow	photodetachment cross section,
	E_γ	\rightarrow	photon flux (laser propagating in z-direction),
	p_i	\rightarrow	ions normalized column density.

Consequently, the number of ions remaining in the trap exhibits an exponential decay. In Eq. (79) the intensity profile in propagation direction of the laser is assumed to be constant. Additionally assuming that the size of the laser beam is small compared to the size of the ion cloud, the spatial dependence of the photon flux can be expressed as

$$F_\gamma(x, y) = \frac{P_\gamma}{h\nu} \delta(x - x_\gamma) \delta(y - y_\gamma), \quad (80)$$

with	P_γ	→	power of the laser beam,
	$h\nu$	→	photon energy,
	$\delta(\dots)$	→	Dirac delta function,
	x_γ, y_γ	→	position of the laser beam.

In this case the integral in Eq. (79) reduces to the product of the laser intensity and the normalized column density of the ion cloud $p_{i,z}$ at the position of the laser. The number of ions remaining in the trap is given by

$$N(t) = N_0 \exp \left[-R_0 t_{\text{trap}} - \left(\sigma_{\text{pd}} \frac{P_\gamma}{h\nu} p_{i,z}(x_\gamma, y_\gamma) \right) t_\gamma \right] \quad (81)$$

with	t_{trap}	→	total trapping time,
	t_γ	→	time of exposure with detachment laser.

Assuming that the background loss rate from the trap R_0 is well characterized, the exponential decay rate of the ions in the trap is directly proportional to the absolute cross section and the ions column density at the position of the detachment laser. Consequently, measuring the decay rate as a function of the laser position for the entire ion trap yields the ions density profile and the absolute cross section.

4.4.3 Photodetachment spectroscopy

As explained previously, photodetachment spectroscopy can be used to gain information about the ions rotational as well as motional temperature. Assuming that the ions energy distribution is well described by a thermal Maxwell-Boltzmann distribution the relative step height of a single photodetachment cross section is sufficient to estimate the rotational temperature of the ion cloud. Fig. 56 shows the relative step heights of different thresholds as well as the relative cross section at the threshold. The numbering of the transitions is the same as in Table 5. First, it is favorable for the relative step height (blue bars) to be as large as possible as this increases the signal to noise ratio. Second, the absolute cross section (shown in red) should not be too small as thresholds with very small cross sections require very large laser powers in order to eliminate a sufficient fraction of ions from the trap.

At 300K the relative step heights of the Q₃ and the P₃ branches (1st and 3rd threshold for every J'' value) are by far the largest. As a good compromise between relative step height and total cross section we chose the P₃(3) transition to estimate the rotational temperature of our ion cloud. Fig. 57 shows the resulting spectrum for OH⁻ ions in the HAITrap. From the numerical fit with our model we can determine a rotational temperature of $T_{\text{rot}} = (420 \pm 40)\text{K}$. The error corresponds to the uncertainty of the fit. An additional systematic error arises from

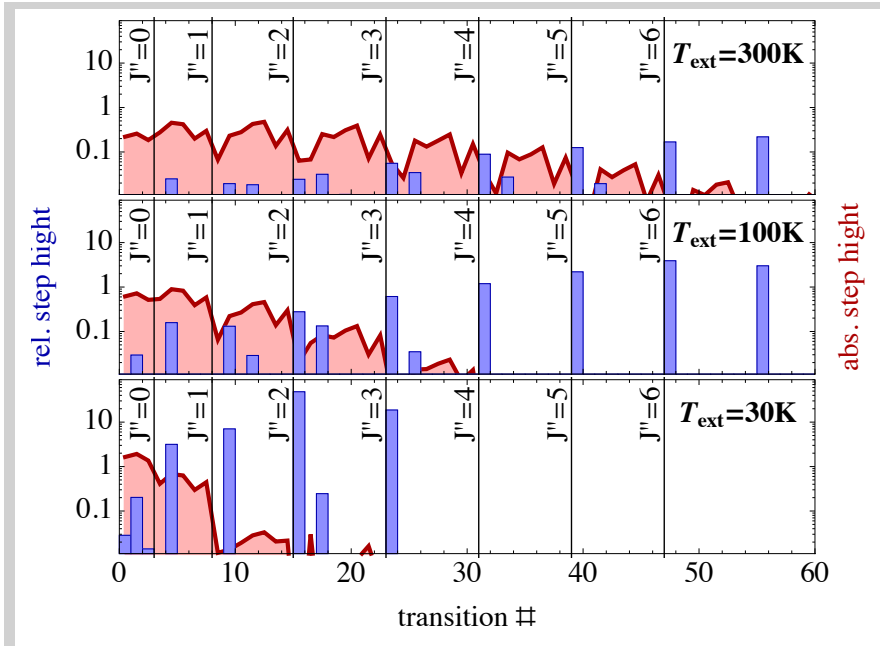


Figure 56: Relative and absolute change of the cross section for different photodetachment thresholds. The three graphs correspond to different translational temperatures. The numbering of the states corresponds to the one found in Table 5.

the model which assumes a thermal distribution. In order to estimate the impact of this systematic error a wider photodetachment spectrum with multiple thresholds would be required.

Another interesting aspect of the photodetachment spectrum is the shape of the spectrum close to threshold. As shown in section 4.3.2, the doppler broadening of the threshold can be used to estimate the motional temperature of the cloud. Unfortunately, with our current setup the wavelength stability of the dye-laser is not sufficient to measure this effect. With the high-precision spectrometer a long-term drift on the order of 100MHz/h has been measured which also corresponds to the stability of the spectrometer itself. Therefore we can only determine the laser wavelength to an accuracy on the order of 100MHz which is on the same scale as the Doppler broadening at room temperature. In order to perform more precise measurements, the laser needs to be stabilized to a frequency reference which might be implemented in the future.

4.4.4 Photodetachment tomography

A different approach to measure the ions motional temperature is photodetachment tomography. This technique allows to measure the ions density distribution by measuring the ions loss rate as a function

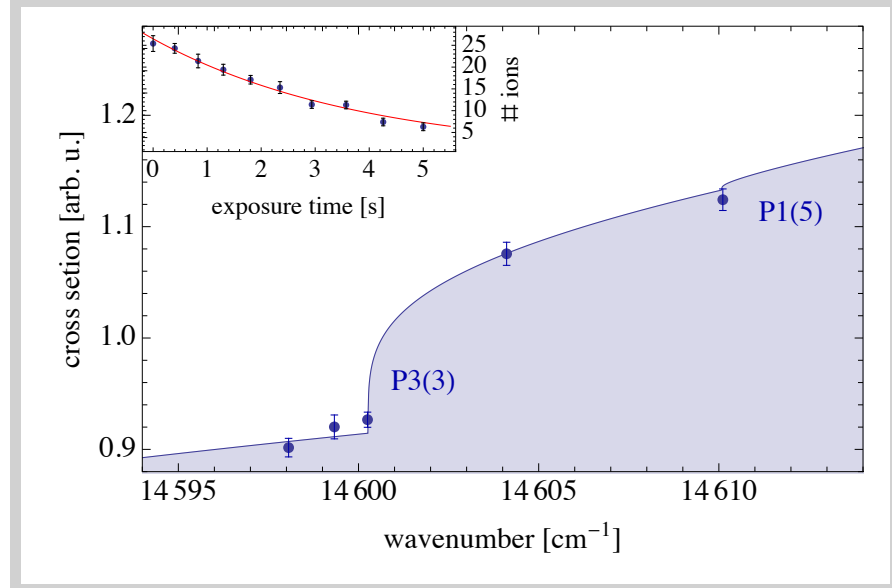


Figure 57: Photodetachment spectrum of OH⁻ ions in the HAITrap. The data was fitted with the theoretical model resulting in a rovibrational temperature of $T_{\text{rot}} = (420 \pm 40)\text{K}$.

of the detachment laser position. From the exponential decay rate k ($N = N_0 \exp[-kt]$), the ions column density can be extracted as [136]

$$\rho_{i,z}(x_\gamma, y_\gamma) = \frac{k(x_\gamma, y_\gamma) - R_0}{\sigma_{\text{pd}} P_\gamma / (h\nu)} \quad (82)$$

Fig. 58 shows a measured density distribution inside the HAITrap. The wires are excluded from the measurement because as soon as the laser hits a wire, light is randomly scattered into the trap illuminating ions over a large volume. The distribution shown on the left was calculated by using the potentials from the numeric simulations performed with SIMION (cf. Fig. 34). In order to better match the experimental results an additional linear field gradient of 14mV/mm in radial direction was added to the potential. From this potential the ion distribution was calculated assuming a temperature of $400 \pm 50\text{K}$ which gave the best match with the experimental data. As a result, the ion distribution is shifted to the top of the ion trap.

The effect of the linear gradient can best be seen in one dimensional cuts through the density distribution as shown in Fig. 59. Just in case of the radial pockets discussed in section 3.1.6.4, the maximum of the ion distribution lies behind the rf-wires. Without the gradient an ion distribution as shown in Fig. 35 (bottom) would be expected.

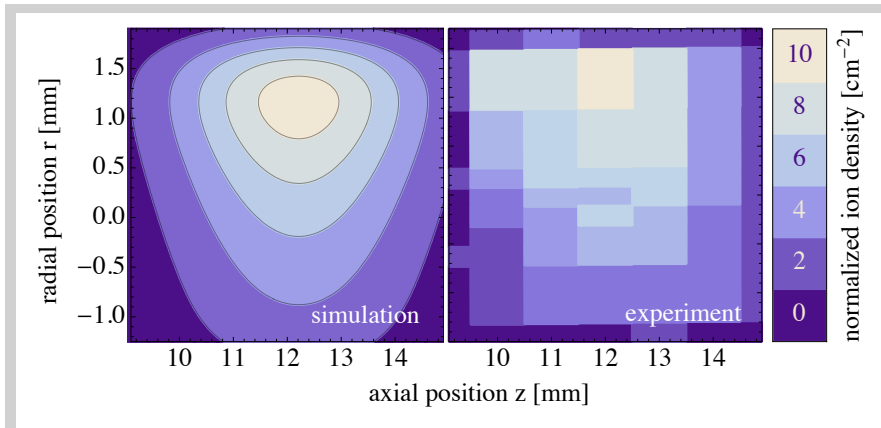


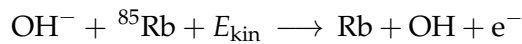
Figure 58: Two-dimensional density distribution of the ions in the HAITrap. The shown density corresponds to the normalized single particle density. The left density distribution has been calculated with the potentials obtained from SIMION simulations. A linear field gradient in radial direction was added to get a better match with the data. This field gradient would correspond to a voltage difference of 1.4 between the shieldings above and below the trap.

4.5 RUBIDIUM - OH⁻ COLLISIONS

There are different inelastic reaction channels for collisions between OH⁻ and rubidium. Energetically possible are associative detachment



where atom and ion form a molecule and the electron is ejected. Another possible reaction in high energy collision with the atom is dissociative detachment



where the accessible kinetic energy is used to detach the atom. At room temperature this reaction channel should be entirely frozen and the associative detachment channel should by far dominate the loss rate.

4.5.1 Associative detachment of OH⁻

In a first theoretical investigation of the associative detachment channel it was concluded that it can only occur in vibrationally excited OH⁻ [182]. This result was recently challenged by an experiment showing hints of associative detachment [101] and a second theoretical study which suggests that associative detachment should also be possible in the vibrational ground state [183]. It seems that in the

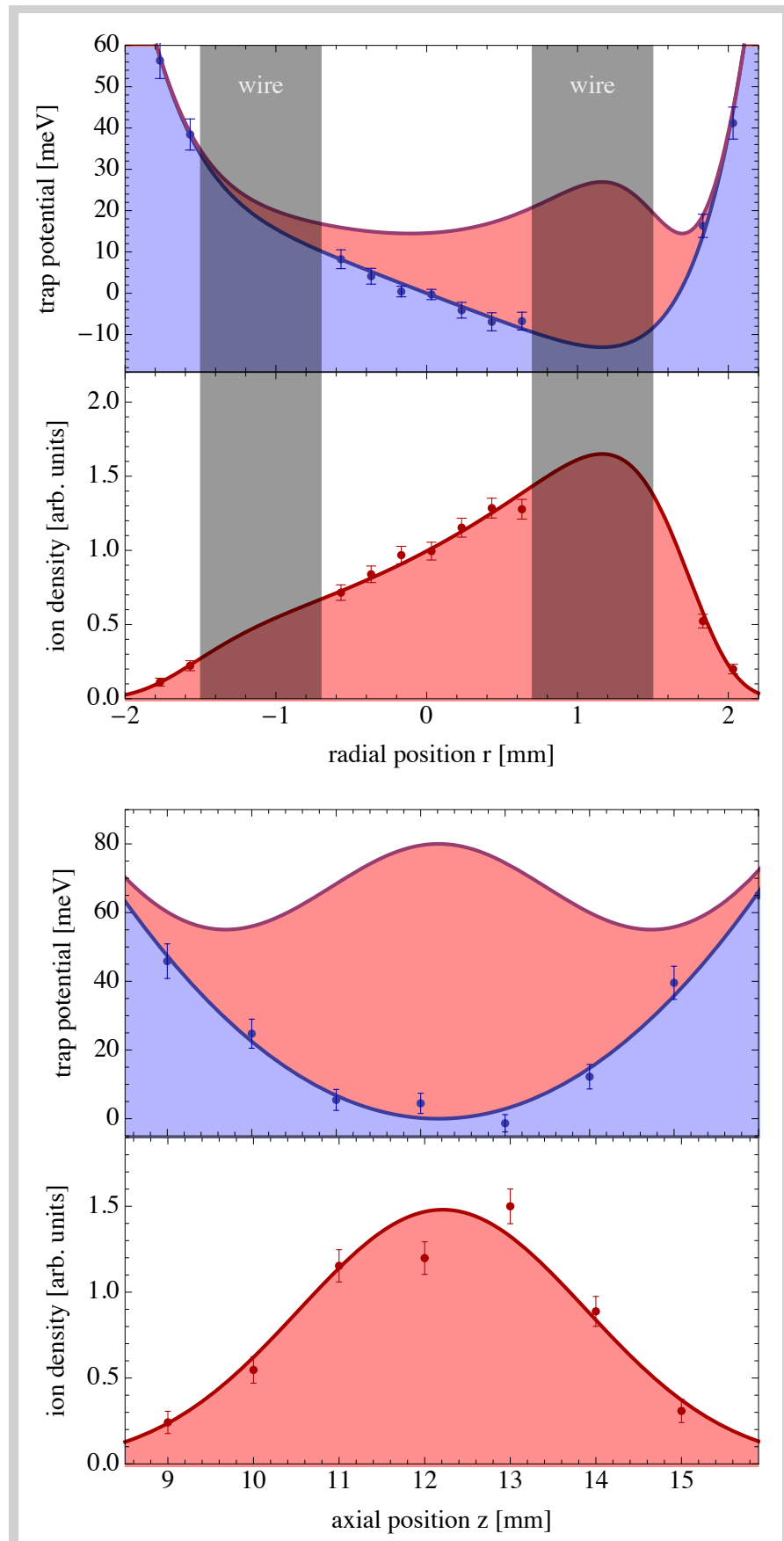


Figure 59: Density distributions of the OH^- ions in the HAITrap. The blue curves indicate the potentials calculated with SIMION, the red curves are the corresponding density distributions for a temperature of $T = 400\text{K}$.

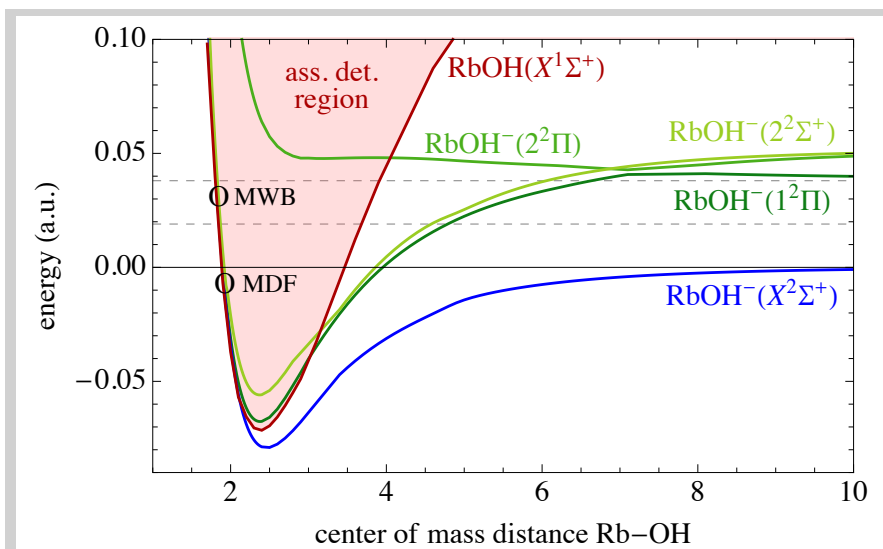


Figure 60: RbOH⁻ potential curves. The entrance channel for ground state rubidium is shown in blue, collisions with excited rubidium atoms correspond to one of the three green curves. The associative detachment channel corresponds to the red curve and whenever the system enters the red shaded area the associative detachment channel opens up. The two circles mark the crossings calculated with different core potentials. The dashed lines indicate the first vibrationally excited levels. The circles mark the crossings from the ground state to the associative detachment channel. Details are explained in the text. With special thanks to Milaim Kas for providing the potential curves.

first study by Byrd *et al.* [182] the rubidium hydroxide energy surface was calculated using the wrong effective core potentials for rubidium. These potentials model the potential of the core electrons so that the actual calculation of the reactive collision only has to treat the valence electrons of the rubidium atom. There is different libraries of such core potentials and it seems that the one used by Byrd *et al.* (ECP28MWB) fails for rubidium [184] which leads to a crossing of the molecular states at higher energies. A better result is obtained by using the ECP28MDF potential for rubidium which shifts the crossing to an energy below the dissociation energy of the Rb-OH⁻ system.

A sketch of the different Rb-OH⁻ potentials is shown in Fig. 60. The ground state is indicated by the blue line from where the collision can lead to the associative detachment curve shown in red. Both crossings for the two different types of core potentials are marked by the circles. The cross section for this reaction was calculated as $\sigma_{ad} \approx 0.42 \times 10^{-9} \text{cm}^3/\text{s}$ (at 300K) and is supposed to slightly decrease at lower temperatures [183]. This is about one order of magnitude smaller than the Langevin cross section of $\sigma_{Lan} = 4.2 \times 10^{-9} \text{cm}^3/\text{s}$ which is a good estimate for the total collision rate. This means that we can expect an average of ten elastic collisions before an associative

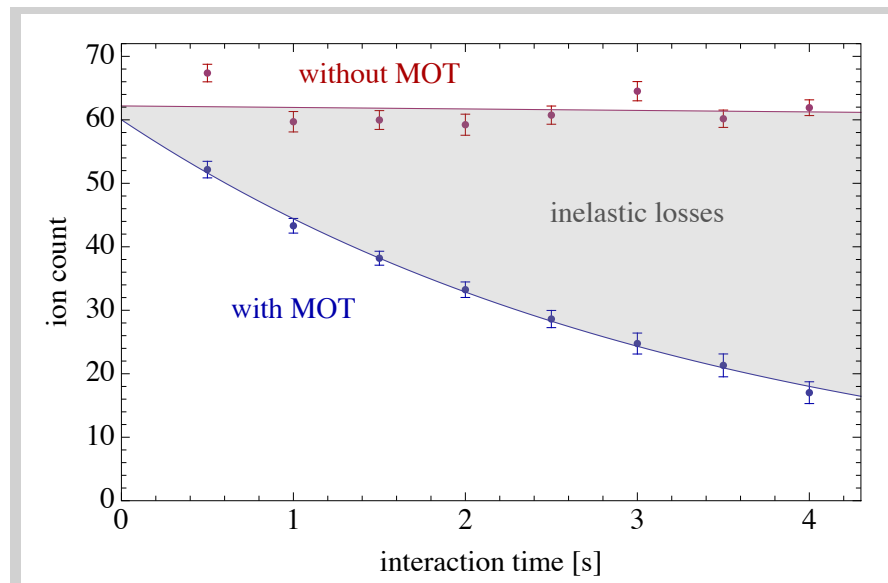
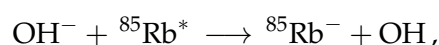


Figure 61: Inelastic losses of OH⁻ in collisions with rubidium. Shown is the number of detected ions as a function of the atom-ion interaction time. The laser cooled cloud of rubidium atoms was placed at the center of the HAITrap. The difference between the two curves depends to the sum of all loss channels which are discussed in the text.

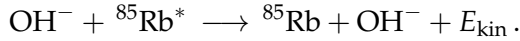
detachment reaction leads to the loss of the ion from the trap which is still be sufficient for sympathetic cooling.

All the theoretical work has so far entirely focused on collisions with rubidium in the ground state. It would be interesting to also estimate the strength of the different loss channels for collisions with excited rubidium atoms as these are always present in a magneto optical trap. That there is a change in the collision rates can already be seen from the Langevin cross section ($\sigma_{\text{Lan}} = 7.12 \times 10^{-9} \text{cm}^3/\text{s}$) which is about twice as large as the one of ground state rubidium [183]. It was also shown that for rubidium in a P-state, the actual cross sections can be even larger [185] as the Langevin model does not take into account the induced quadrupole of this state. Unfortunately, the cross sections for collisions between OH⁻ and excited Rb is not known as multiple level crossings and avoided crossings make this system much harder to describe theoretically.

This is shown in Fig. 60 where the three green curves correspond to possible excited states assuming a linear geometry of the molecule. There are two more reaction channels opening for the excited system. First, the additional electron can be transferred from the OH molecule to the rubidium atom



thus neutralizing the ion. Second, there is a crossing between the excited and the ground state at small interatomic distances



which allows to transfer part of the excitation energy to the OH⁻ ion expelling it from the trap. The third and possibly strongest loss channel is again the associative detachment channel



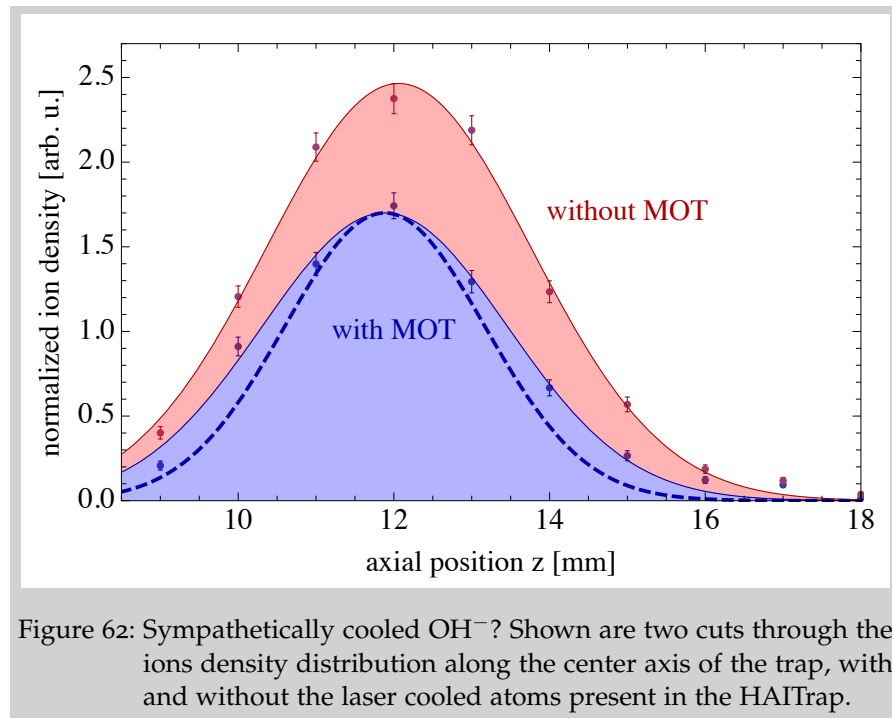
discussed above.

In a first experiment the total loss rate of OH⁻ was found to be similar for collisions with excited and ground state rubidium [101]. This measurement was performed by changing the excited state fraction (see Fig. 47). In our current HAITrap setup more precise measurements can be performed in the future as the Dark SPOT allows us to vary the bright state fraction from less than five percent all the way to nearly half the atoms in the excited state. First measurements of the OH⁻ loss rate are shown in Fig. 61. Based on this single experiment we cannot distinguish between the different loss channels discussed above and the measured loss rate is therefore the sum of all reaction channels. We have extract a preliminary total cross section of $\sigma = 3_{-1.5}^{+3} \times 10^{-10} \text{cm}^3/\text{s}$ with the relative overlap between the atom and ion cloud being by far the largest source of error. This result agrees with previous measurements [101] and with the theoretical results [183] discussed above. In the future this error can be reduced by precisely measuring the relative placement of atom and ion cloud.

4.5.2 Sympathetic cooling of OH⁻

In recent experiments performed with our setup we have focused our attention on sympathetic cooling of the OH⁻ ions. The prospects of cooling OH⁻ sympathetically using laser cooled atoms has already been investigated theoretically. It was shown that the ro-vibrational degrees of freedom can be efficiently cooled through elastic collisions with rubidium [186, 187]. As we have shown in the second chapter, also the motional degrees of freedom should be efficiently cooled.

Our efforts have so far been hindered by the limitations caused by the radial pockets at high offset voltages (see Fig. 35) and the linear field gradient at low offset voltages (see Fig. 59). In both of these trap potentials the potential minimum and thus the maximum of the ion distribution cannot be probed by the detachment laser as is hidden behind the rf-wires. For high offset potentials this cannot be avoided but at low voltages the potentials the linear gradient can be compensated by the shielding electrodes placed above and below the ion trap. Unfortunately, the voltage supplies currently used in the setup do not allow to modify the voltages after the offset voltage have



been ramped to the lower setting. This can be fixed in the future by extending the experimental control software.

Nevertheless, first hints of sympathetic cooling could be observed indirectly. Fig. 62 shows the ions density distribution along the center of the trap with and without atoms present inside the trap. This corresponds to a line along the $r = 0$ axis in Fig. 58. There is a clear difference between the two distributions as the ion density becomes smaller if the atoms are present. It should be pointed out that the measured densities are always normalized densities and are independent of the total number of ions inside the trap. Lower densities do therefore not indicate a smaller absolute density but a redistribution of the ions inside the trap. As the density decreases over the entire volume that can be probed with the detachment laser, the only possible explanation is that the ion density at the potential minimum behind the wires has been increased. Using the simulated potentials inside the rf-trap the measured distributions can be used to estimate the temperature of the ions after they have been brought into contact with the laser cooled atoms. The dashed line in Fig. 62 shows a thermal ion distribution inside the trap potential for $T = 125\text{K}$. It is clear that the measured width of the ion distribution does not match the one of this thermal distribution. It can therefore be concluded that the ions exhibit a non-thermal distribution which makes it very difficult to put a number on the ions final temperature. But that fact that the ions density has decreased over the entire observable volume and therefore must have been increased around the potential minimum is a strong indication that sympathetic cooling has been achieved. In

order to properly characterize the ions final temperature in the future the potential minimum has to be shifted to the trap center so that it can be directly probed by the detachment laser. Up to date this could not be realized but it should be possible in the near future.

CONCLUSION

It has been common wisdom, starting from early work of Dehmelt and others, that one cannot cool ions in a radio-frequency (rf) trap with a buffer gas if the mass ratio $\zeta = m_a/m_i$ between the buffer gas atom and ion exceeds a critical value ζ_{crit} of approximately unity. In this thesis, we showed that one can overcome this dogma by using a spatially localized buffer gas and/or a higher multipole order n for the radial trapping potential. These approaches make use of the fact, that the principle hindrance of sympathetic cooling inside an RF trap arises from a collisionally induced energy transfer between the rf-driven micromotion and the macromotion. Thus, spatially restricting collisions to the volume of minimal micromotion and/or reducing the average micromotion altogether, leads to an increased critical mass ratio which allows the use heavier buffer gases.

In order to obtain a quantitative understanding how these approaches change the equilibrium state of the system, we developed a comprehensive model providing an intuitive picture of collisions in an rf trap. Our model is based on a favorable frame transformation, where the micromotion is assigned to the neutral buffer gas instead of the ion. In this frame the atoms exhibit a spatially dependent velocity which is composed of the atoms thermal distribution at the trap center with a growing contribution of the micromotion for larger radii. Due to the assignment of the micromotion to the buffer gas this second contribution reaches its maximum value at the ions turning point in the ponderomotive potential where it can become even twice as large as then the ions maximum macromotion velocity. For a heavy ion emerged into a buffer gas consisting of light particles this does not influence the system much, as the maximum velocity of the ion is small and assigning it to the far lighter neutral does not have a large impact. In the reversed scenario however, the large maximum velocity of a light ion can be transferred to a heavy buffer gas particle creating a system where the ion can gain up to eight times its initial velocity during a single collision. As this process is independent of the ions absolute energy this leads to run-away heating resulting in the ions loss from the trap. Using this model we could derive analytic expressions for the pole-order dependence of the critical mass ratio which scales as $\zeta_{\text{crit}} \approx 1.5(n - 1)$.

In contrast to previous investigations, our model allows the description of an ion inside a trap of arbitrary multipole order colliding with buffer gas atoms of an arbitrary spatial distribution. Based on this we have numerically determined the ion's steady-state energy and

spatial distributions. Depending on the atom-to-ion mass ratio, we found three distinct dynamical regimes, characterized by analytical expressions for the ion's equilibrium energy distribution. For low mass ratios the ion thermalizes with the buffer gas, with small deviations being caused by the confining effective potential. With growing mass ratio, the energy as well as spatial distribution exhibits a power law towards larger energies/radii. We found heuristic expressions for this mass ratio dependence of the power law exponent. As expected from the discussion above, an ion immersed into a homogeneous buffer gas cannot stably be trapped for mass ratios much larger than the critical mass ratio. Using a localized buffer gas however, we found the emergence of a novel regime of stable cooling for ions far beyond the critical mass ratio. In this regime one can actively tune the ions temperature by controlling the buffer gas' extension and/or the rf-trap fields (forced sympathetic cooling).

These findings are directly applicable to cooling of ions with laser cooled atoms or He buffer gas in Paul traps (as used in the quantum information and quantum simulation communities) or multipole traps (as used in the chemical reaction and astrochemistry communities). Especially for experiments investigating interactions of ions with an ensemble of ultracold atoms, the prospect of using heavier atom species, makes a whole new range of possible systems available that have not been studied yet. Especially the use of forced sympathetic cooling might offer an interesting tool to perform temperature dependent measurement as it allows to precisely tune the ions equilibrium energy distribution.

A new experiment along these lines was presented in the second part of this thesis. We developed a hybrid atom ion trap (HAITrap) for OH^- ions trapped together with laser cooled rubidium atoms. With a mass ratio of $\zeta = 5$ our system is far beyond the standard critical mass ratio around unity and even the pole order dependent critical mass ratio introduced earlier is slightly smaller. This means that in this system cooling should only be possible due to the localization of the laser cooled atoms and forced sympathetic cooling is feasible.

In order to properly characterize all parameters of the system, specifically the temperature and density distribution of the ions as well as the atoms different techniques have been implemented. The main challenge in characterizing the atom cloud is the very high optical density of the cloud which is on the order of one-hundred. At this density most standard imaging techniques fail as the cloud is optically thick and can no longer be probed by a resonant laser beam. We therefore implemented saturation absorption imaging scheme with the probe laser being detuned from the resonance frequency. Using this technique we found the total number of atoms in the trap to be as large as 1.5×10^9 at a peak density of 3×10^{11} atoms/cm³.

The ion cloud was characterized by performing photodetachment measurements on the OH^- ions. Photodetachment spectroscopy was used to obtain information about the ions ro-vibrational temperature. In order to analyze the measured data a simple theoretical model was developed with the ro-vibrational temperature being the only free parameter. This way the internal temperature of the molecular anions was determined to be $T \approx (420 \pm 40)\text{K}$. The translational temperature was analyzed using photodetachment tomography. In combination with trap potentials obtained from SIMION calculations the translational temperature is estimated to be $(400 \pm 50)\text{K}$.

Finally the ions and atoms were brought together inside the hybrid trap. On the one hand this could be used to obtain a first estimate of the inelastic cross section of rubidium - OH^- collisions. On the other hand we found first indications for sympathetic cooling in our HAITrap. Unfortunately, due to certain experimental limitations a satisfying estimate of the ions final temperature could not be achieved. Nevertheless, this result is the first realization of sympathetic cooling of a negative ion using laser cooled atoms. Our experiment is also one of the very few which has an atom-to-ion mass ratio larger than unity. We hope that our theoretical work might motivate more groups to pursue the same path.

5.0.3 Outlook

The theoretical model could be extended to also model axial confinement which has so far been neglected. As there is no analytical model for the final energy distributions it might be helpful for the HAITrap community to provide a tool which calculates the ions equilibrium energy and spatial distributions depending on the different experimental parameters. The required algorithm is already fully developed but it would still be required to provide an intuitive user interface.

In the experiment there is a number of improvements which will be implemented in the future. First and most importantly, a better control over all electrode voltages with the possibility to separately ramp down all voltages of the trap will be required. Second, a more efficient ion detection would be beneficial. So far the detection is limited by the maximum count rate of the ion detector which could be fixed by using a micro-channel plate detector instead. In combination with a phosphor screen or a delay line this could also be used to spatially image the cloud by transversally extracting the ions onto a position sensitive detector. Such a detection scheme would also be beneficial as it would greatly decrease the time of the measurements as the density distribution could be measured in a single shot. With the current setup, a full two-dimensional scan of the ion cloud takes several hours.

For future experiments, there is a whole set of interesting questions that can be addressed with our setup. In the near future, our interest

will be focused on improving our sympathetic cooling scheme. The key here should be the improved control over the trapping potentials discussed above. It will be very interesting to see if forced sympathetic cooling will work as predicted by our theoretical model. Using photodetachment spectroscopy also any change of the ions ro-vibrational temperature can be detected. The photodetachment spectrum in its own is also an interesting field for further studies. Especially the threshold behaviors of different transitions should be investigated in greater detail.

In the more distant future different kinds of ions can be studied. The first candidate that comes to mind are water clusters which consist of a single O^- or OH^- ion with N water molecules clustered around it. These clusters have already been observed in time-of-flight spectra taken with our current ion source and by changing the seed gas it will also be possible to create a large number of other ions.

BIBLIOGRAPHY

- [1] H.E. Hall, P.J. Ford, and K. Thompson. A helium-3 dilution refrigerator. *Cryogenics*, 6(2):80 – 88, 1966. ISSN 0011-2275. doi: [http://dx.doi.org/10.1016/0011-2275\(66\)90034-8](http://dx.doi.org/10.1016/0011-2275(66)90034-8). URL <http://www.sciencedirect.com/science/article/pii/S0011227566900348>.
- [2] E. L. Raab, M. Prentiss, Alex Cable, Steven Chu, and D. E. Pritchard. Trapping of neutral sodium atoms with radiation pressure. *Phys. Rev. Lett.*, 59:2631–2634, Dec 1987. doi: 10.1103/PhysRevLett.59.2631. URL <http://link.aps.org/doi/10.1103/PhysRevLett.59.2631>.
- [3] A. M. Steane and C. J. Foot. Laser cooling below the doppler limit in a magneto-optical trap. *EPL (Europhysics Letters)*, 14(3): 231, 1991. URL <http://stacks.iop.org/0295-5075/14/i=3/a=008>.
- [4] W. Ketterle, D. S. Durfee, and D. M. Stamper-Kurn. Making, probing and understanding bose-einstein condensates. *ArXiv e-prints*, 1999. URL <https://arxiv.org/abs/cond-mat/9904034>.
- [5] Iain D Couzin and Nigel R Franks. Self-organized lane formation and optimized traffic flow in army ants. *Proceedings of the Royal Society of London B: Biological Sciences*, 270(1511):139–146, 2003.
- [6] C. W. Chou, D. B. Hume, T. Rosenband, and D. J. Wineland. Optical clocks and relativity. *Science*, 329(5999):1630–1633, 2010. ISSN 0036-8075. doi: 10.1126/science.1192720. URL <http://science.sciencemag.org/content/329/5999/1630>.
- [7] Immanuel Bloch, Jean Dalibard, and Sylvain Nascimbene. Quantum simulations with ultracold quantum gases. *Nature Physics*, 8(4):267–276, 2012.
- [8] Juan I Cirac and Peter Zoller. Quantum computations with cold trapped ions. *Physical review letters*, 74(20):4091, 1995.
- [9] Rainer Blatt and CF Roos. Quantum simulations with trapped ions. *Nature Physics*, 8(4):277–284, 2012.
- [10] Peter W. Shor. Polynomial-time algorithms for prime factorization and discrete logarithms on a quantum computer. *SIAM Review*, 41(2):303–332, 1999. doi: 10.1137/S0036144598347011. URL <http://dx.doi.org/10.1137/S0036144598347011>.

- [11] E. A. Cornell and C. E. Wieman. Nobel lecture: Bose-einstein condensation in a dilute gas, the first 70 years and some recent experiments. *Rev. Mod. Phys.*, 74:875–893, Aug 2002. doi: 10.1103/RevModPhys.74.875. URL <http://link.aps.org/doi/10.1103/RevModPhys.74.875>.
- [12] Jit Kee Chin, DE Miller, Y Liu, C Stan, W Setiawan, C Sanner, K Xu, and W Ketterle. Evidence for superfluidity of ultracold fermions in an optical lattice. *Nature*, 443(7114):961–964, 2006.
- [13] David Bailin and Alexander Love. Superfluidity and superconductivity in relativistic fermion systems. *Physics Reports*, 107(6): 325–385, 1984.
- [14] Hidetoshi Katori, Tetsuya Ido, Yoshitomo Isoya, and Makoto Kuwata-Gonokami. Magneto-optical trapping and cooling of strontium atoms down to the photon recoil temperature. *Phys. Rev. Lett.*, 82:1116–1119, Feb 1999. doi: 10.1103/PhysRevLett.82.1116. URL <http://link.aps.org/doi/10.1103/PhysRevLett.82.1116>.
- [15] E. A. Curtis, C. W. Oates, and L. Hollberg. Quenched narrow-line laser cooling of ^{40}Ca to near the photon recoil limit. *Phys. Rev. A*, 64:031403, Aug 2001. doi: 10.1103/PhysRevA.64.031403. URL <http://link.aps.org/doi/10.1103/PhysRevA.64.031403>.
- [16] T. Kuwamoto, K. Honda, Y. Takahashi, and T. Yabuzaki. Magneto-optical trapping of yb atoms using an intercombination transition. *Phys. Rev. A*, 60:R745–R748, Aug 1999. doi: 10.1103/PhysRevA.60.R745. URL <http://link.aps.org/doi/10.1103/PhysRevA.60.R745>.
- [17] J. J. McClelland and J. L. Hanssen. Laser cooling without repumping: A magneto-optical trap for erbium atoms. *Phys. Rev. Lett.*, 96:143005, Apr 2006. doi: 10.1103/PhysRevLett.96.143005. URL <http://link.aps.org/doi/10.1103/PhysRevLett.96.143005>.
- [18] D. Sukachev, A. Sokolov, K. Chebakov, A. Akimov, S. Kanorsky, N. Kolachevsky, and V. Sorokin. Magneto-optical trap for thulium atoms. *Phys. Rev. A*, 82:011405, Jul 2010. doi: 10.1103/PhysRevA.82.011405. URL <http://link.aps.org/doi/10.1103/PhysRevA.82.011405>.
- [19] Mingwu Lu, Nathaniel Q. Burdick, Seo Ho Youn, and Benjamin L. Lev. Strongly dipolar bose-einstein condensate of dysprosium. *Phys. Rev. Lett.*, 107:190401, Oct 2011. doi: 10.1103/PhysRevLett.107.190401. URL <http://link.aps.org/doi/10.1103/PhysRevLett.107.190401>.

- [20] Boerge Hemmerling, Garrett K Drayna, Eunmi Chae, Aakash Ravi, and John M Doyle. Buffer gas loaded magneto-optical traps for yb, tm, er and ho. *New Journal of Physics*, 16(6):063070, 2014. URL <http://stacks.iop.org/1367-2630/16/i=6/a=063070>.
- [21] C. C. Bradley, J. J. McClelland, W. R. Anderson, and R. J. Celotta. Magneto-optical trapping of chromium atoms. *Phys. Rev. A*, 61:053407, Apr 2000. doi: 10.1103/PhysRevA.61.053407. URL <http://link.aps.org/doi/10.1103/PhysRevA.61.053407>.
- [22] F. Diedrich, E. Peik, J. M. Chen, W. Quint, and H. Walther. Observation of a phase transition of stored laser-cooled ions. *Phys. Rev. Lett.*, 59:2931–2934, Dec 1987. doi: 10.1103/PhysRevLett.59.2931. URL <http://link.aps.org/doi/10.1103/PhysRevLett.59.2931>.
- [23] Niels Kjærgaard and Michael Drewsen. Observation of a structural transition for coulomb crystals in a linear paul trap. *Phys. Rev. Lett.*, 91:095002, Aug 2003. doi: 10.1103/PhysRevLett.91.095002. URL <http://link.aps.org/doi/10.1103/PhysRevLett.91.095002>.
- [24] Bretislav Friedrich and John M Doyle. Why are cold molecules so hot? *ChemPhysChem*, 10(4):604–623, 2009.
- [25] M. D. Di Rosa. Laser-cooling molecules. *The European Physical Journal D - Atomic, Molecular, Optical and Plasma Physics*, 31(2):395–402, 2004. ISSN 1434-6079. doi: 10.1140/epjd/e2004-00167-2. URL <http://dx.doi.org/10.1140/epjd/e2004-00167-2>.
- [26] Benjamin K. Stuhl, Brian C. Sawyer, Dajun Wang, and Jun Ye. Magneto-optical trap for polar molecules. *Phys. Rev. Lett.*, 101:243002, Dec 2008. doi: 10.1103/PhysRevLett.101.243002. URL <http://link.aps.org/doi/10.1103/PhysRevLett.101.243002>.
- [27] Tobias Schneider, B Roth, H Duncker, I Ernsting, and S Schiller. All-optical preparation of molecular ions in the rovibrational ground state. *Nature Physics*, 6(4):275–278, 2010.
- [28] E. S. Shuman, J. F. Barry, and D. DeMille. Laser cooling of a diatomic molecule. *Nature*, 467(7317):820–823, 10 2010. URL <http://dx.doi.org/10.1038/nature09443>.
- [29] J. F. Barry, E. S. Shuman, E. B. Norrgard, and D. DeMille. Laser radiation pressure slowing of a molecular beam. *Phys. Rev. Lett.*, 108:103002, Mar 2012. doi: 10.1103/PhysRevLett.108.103002. URL <http://link.aps.org/doi/10.1103/PhysRevLett.108.103002>.

- [30] Matthew T. Hummon, Mark Yeo, Benjamin K. Stuhl, Alejandra L. Collopy, Yong Xia, and Jun Ye. 2d magneto-optical trapping of diatomic molecules. *Phys. Rev. Lett.*, 110:143001, Apr 2013. doi: 10.1103/PhysRevLett.110.143001. URL <http://link.aps.org/doi/10.1103/PhysRevLett.110.143001>.
- [31] V. Zhelyazkova, A. Cournol, T. E. Wall, A. Matsushima, J. J. Hudson, E. A. Hinds, M. R. Tarbutt, and B. E. Sauer. Laser cooling and slowing of ca f molecules. *Phys. Rev. A*, 89:053416, May 2014. doi: 10.1103/PhysRevA.89.053416. URL <http://link.aps.org/doi/10.1103/PhysRevA.89.053416>.
- [32] Pierre Pillet, Cyril Drag, Bruno Laburthe Tolra, Daniel Comparat, Andrea Fioretti, Samuel Guibal, Claude Amiot, Anne Crubellier, Olivier Dulieu, and Franoise Masnou-Seeuws. Photoassociative spectroscopy and formation of cold molecules. *Physica Scripta*, 2000(T86):38, 2000. URL <http://stacks.iop.org/1402-4896/2000/i=T86/a=006>.
- [33] Tim Rom, Thorsten Best, Olaf Mandel, Artur Widera, Markus Greiner, Theodor W. Hänsch, and Immanuel Bloch. State selective production of molecules in optical lattices. *Phys. Rev. Lett.*, 93:073002, Aug 2004. doi: 10.1103/PhysRevLett.93.073002. URL <http://link.aps.org/doi/10.1103/PhysRevLett.93.073002>.
- [34] G. Thalhammer, K. Winkler, F. Lang, S. Schmid, R. Grimm, and J. Hecker Denschlag. Long-lived feshbach molecules in a three-dimensional optical lattice. *Phys. Rev. Lett.*, 96:050402, Feb 2006. doi: 10.1103/PhysRevLett.96.050402. URL <http://link.aps.org/doi/10.1103/PhysRevLett.96.050402>.
- [35] Cheng Chin, Rudolf Grimm, Paul Julienne, and Eite Tiesinga. Feshbach resonances in ultracold gases. *Rev. Mod. Phys.*, 82:1225–1286, Apr 2010. doi: 10.1103/RevModPhys.82.1225. URL <http://link.aps.org/doi/10.1103/RevModPhys.82.1225>.
- [36] P. Bowe, L. Hornekær, C. Brodersen, M. Drewsen, J. S. Hangst, and J. P. Schiffer. Sympathetic crystallization of trapped ions. *Phys. Rev. Lett.*, 82:2071–2074, Mar 1999. doi: 10.1103/PhysRevLett.82.2071. URL <http://link.aps.org/doi/10.1103/PhysRevLett.82.2071>.
- [37] D. S. Goodman, I. Sivarajah, J. E. Wells, F. A. Narducci, and W. W. Smith. Ion-neutral-atom sympathetic cooling in a hybrid linear rf paul and magneto-optical trap. *Phys. Rev. A*, 86:033408, Sep 2012. doi: 10.1103/PhysRevA.86.033408. URL <http://link.aps.org/doi/10.1103/PhysRevA.86.033408>.
- [38] K. Ravi, Seunghyun Lee, Arijit Sharma, G. Werth, and S.A. Rangwala. Cooling and stabilization by collisions in a mixed

- ion-atom system. *Nat Commun*, 3:1126–, October 2012. doi: 10.1038/ncomms2131.
- [39] Peter F Staunum, Klaus Højbjerg, Peter S Skyt, Anders K Hansen, and Michael Drewsen. Rotational laser cooling of vibrationally and translationally cold molecular ions. *Nature Physics*, 6(4):271–274, 2010.
- [40] Xin Tong, Alexander H Winney, and Stefan Willitsch. Sympathetic cooling of molecular ions in selected rotational and vibrational states produced by threshold photoionization. *Physical review letters*, 105(14):143001, 2010.
- [41] Samar K. Guharay. Negative ions for emerging interdisciplinary applications. *AIP Conference Proceedings*, 1390(1):661–667, 2011. doi: <http://dx.doi.org/10.1063/1.3637438>. URL <http://scitation.aip.org/content/aip/proceeding/aipcp/10.1063/1.3637438>.
- [42] B. Song, N. D’Angelo, and R. L. Merlino. Ion-acoustic waves in a plasma with negative ions. *Physics of Fluids B*, 3(2):284–287, 1991. doi: <http://dx.doi.org/10.1063/1.859736>. URL <http://scitation.aip.org/content/aip/journal/pofb/3/2/10.1063/1.859736>.
- [43] N L Aleksandrov. Negative-ion processes and modern technologies. *Plasma Sources Science and Technology*, 3(2):226, 1994. URL <http://stacks.iop.org/0963-0252/3/i=2/a=013>.
- [44] Theodore P. Snow and Veronica M. Bierbaum. Ion chemistry in the interstellar medium. *Annual Review of Analytical Chemistry*, 1(1):229–259, 2008. doi: 10.1146/annurev.anchem.1.031207.112907. URL <http://dx.doi.org/10.1146/annurev.anchem.1.031207.112907>. PMID: 20636080.
- [45] Alban Kellerbauer and Jochen Walz. A novel cooling scheme for antiprotons. *New Journal of Physics*, 8(3):45, 2006. URL <http://stacks.iop.org/1367-2630/8/i=3/a=045>.
- [46] Nick E Mavromatos. Theoretical and phenomenological aspects of cpt violation. *Nuclear Instruments and Methods in Physics Research Section B: Beam Interactions with Materials and Atoms*, 214: 1–6, 2004.
- [47] Graham M Shore. Strong equivalence, lorentz and cpt violation, anti-hydrogen spectroscopy and gamma-ray burst polarimetry. *Nuclear Physics B*, 717(1):86–118, 2005.
- [48] René C Bilodeau and Harold K Haugen. Experimental studies of os-: observation of a bound-bound electric dipole transition in an atomic negative ion. *Physical review letters*, 85(3):534, 2000.

- [49] Alban Kellerbauer, A Fischer, and U Warring. Measurement of the zeeman effect in an atomic anion: Prospects for laser cooling of os-. *Physical Review A*, 89(4):043430, 2014.
- [50] C. W. Walter, N. D. Gibson, D. J. Matyas, C. Crocker, K. A. Dungan, B. R. Matola, and J. Rohlén. Candidate for laser cooling of a negative ion: Observations of bound-bound transitions in la-. *Phys. Rev. Lett.*, 113:063001, Aug 2014. doi: 10.1103/PhysRevLett.113.063001. URL <http://link.aps.org/doi/10.1103/PhysRevLett.113.063001>.
- [51] Alban Kellerbauer, Giovanni Cerchiarì, Elena Jordan, and C Wesley Walter. High-resolution laser spectroscopy on bound transitions in la-. *Physica Scripta*, 90(5):054014, 2015. URL <http://stacks.iop.org/1402-4896/90/i=5/a=054014>.
- [52] Oleg P. Makarov, R. Côté, H. Michels, and W. W. Smith. Radiative charge-transfer lifetime of the excited state of (NaCa)⁺. *Phys. Rev. A*, 67:042705, Apr 2003. doi: 10.1103/PhysRevA.67.042705. URL <http://link.aps.org/doi/10.1103/PhysRevA.67.042705>.
- [53] Winthrop W. Smith, Oleg P. Makarov, and Jian Lin. Cold ion-neutral collisions in a hybrid trap. *Journal of Modern Optics*, 52(16):2253–2260, 2005. doi: 10.1080/09500340500275850. URL <http://dx.doi.org/10.1080/09500340500275850>.
- [54] Eric R. Hudson. Method for producing ultracold molecular ions. *Phys. Rev. A*, 79:032716, Mar 2009. doi: 10.1103/PhysRevA.79.032716.
- [55] Andrew T. Grier, Marko Cetina, Fedja Oručević, and Vladan Vuletić. Observation of cold collisions between trapped ions and trapped atoms. *Phys. Rev. Lett.*, 102:223201, Jun 2009. doi: 10.1103/PhysRevLett.102.223201. URL <http://link.aps.org/doi/10.1103/PhysRevLett.102.223201>.
- [56] Christoph Zipkes, Stefan Palzer, Carlo Sias, and Michael Kohl. A trapped single ion inside a bose-einstein condensate. *Nature*, 464(7287):388–391, March 2010. doi: 10.1038/nature08865. URL <http://dx.doi.org/10.1038/nature08865>.
- [57] Stefan Schmid, Arne Harter, Albert Frisch, Sascha Hoinka, and Johannes Hecker Denschlag. An apparatus for immersing trapped ions into an ultracold gas of neutral atoms. *Review of Scientific Instruments*, 83(5):053108, 2012. doi: 10.1063/1.4718356. URL <http://link.aip.org/link/?RSI/83/053108/1>.
- [58] Wade G. Rellergert, Scott T. Sullivan, Steven J. Schowalter, Svetlana Kotochigova, Kuang Chen, and Eric R. Hudson. Evidence for sympathetic vibrational cooling of translationally cold

- molecules. *Nature*, 495(7442):490–494, March 2013. ISSN 0028-0836. doi: 10.1038/nature11937. URL <http://dx.doi.org/10.1038/nature11937>.
- [59] A. Härter and J. Hecker Denschlag. Cold atom-ion experiments in hybrid traps. *ArXiv e-prints*, 2013. URL <http://arxiv.org/abs/1309.5799>.
- [60] Stefan Willitsch. Ion-atom hybrid systems. *ArXiv e-prints*, 2014. URL <http://arxiv.org/abs/1401.1699>.
- [61] S. Dutta, R. Sawant, and S. A. Rangwala. Collisional cooling of light ions by co-trapped heavy atoms. *ArXiv e-prints*, December 2015.
- [62] F. G. Major and H. G. Dehmelt. Exchange-collision technique for the rf spectroscopy of stored ions. *Phys. Rev.*, 170:91–107, Jun 1968. doi: 10.1103/PhysRev.170.91.
- [63] Bastian Höltkemeier, Pascal Weckesser, Henry López-Carrera, and Matthias Weidemüller. Buffer-gas cooling of a single ion in a multipole radio frequency trap beyond the critical mass ratio. *Phys. Rev. Lett.*, 116:233003, Jun 2016. doi: 10.1103/PhysRevLett.116.233003. URL <http://link.aps.org/doi/10.1103/PhysRevLett.116.233003>.
- [64] Bastian Höltkemeier, Pascal Weckesser, Henry López-Carrera, and Matthias Weidemüller. Dynamics of a single trapped ion immersed in a buffer gas. *ArXiv e-prints*, 2016. URL <http://arxiv.org/abs/1608.07120>.
- [65] Pascal M. Weckesser. Sympathetic cooling of ions in radio frequency traps. *Master thesis, Ruprecht Karls Universität Heidelberg*, 2015.
- [66] H López, B Höltkemeier, J Glässel, P Weckesser, M Weidemüller, T Best, E Endres, and R Wester. Sympathetic cooling of oh- ions using ultracold rb atoms in a dark spot. *Ion Traps for Tomorrows Applications*, 189:279, 2015.
- [67] H. G. Dehmelt. Radiofrequency spectroscopy of stored ions. *Adv. in Atomic and Molecular Physics, Volume 3*, pages 53–72, 1967. doi: [http://dx.doi.org/10.1016/S0065-2199\(08\)60170-0](http://dx.doi.org/10.1016/S0065-2199(08)60170-0).
- [68] Pradip K. Ghosh. *Ion Traps*. International Series of Monographs on Physics. Oxford University Press, 1996.
- [69] J. C. Pearson, L. C. Oesterling, Eric Herbst, and F. C. De Lucia. Pressure broadening of gas phase molecular ions at very low temperature. *Phys. Rev. Lett.*, 75:2940–2943, Oct 1995. doi: 10.1103/PhysRevLett.75.2940. URL <http://link.aps.org/doi/10.1103/PhysRevLett.75.2940>.

- [70] S Schlemmer, T Kuhn, E Lescop, and D Gerlich. Laser excited $n = 2+$ in a 22-pole ion trap:: Experimental studies of rotational relaxation processes dedicated to professor michael t. bowers on the occasion of his 60th birthday. *International journal of mass spectrometry*, 185:589–602, 1999.
- [71] Juraj Glosík, P Hlavenka, R Plašil, F Windisch, D Gerlich, A Wolf, and H Kreckel. Action spectroscopy of d_2h^+ using overtone excitation. *Philosophical Transactions of the Royal Society of London A: Mathematical, Physical and Engineering Sciences*, 364(1848): 2931–2942, 2006.
- [72] Oskar Asvany, Padma Kumar P, Britta Redlich, Ilka Hegemann, Stephan Schlemmer, and Dominik Marx. Understanding the infrared spectrum of bare ch_5^+ . *Science*, 309(5738):1219–1222, 2005. ISSN 0036-8075. doi: 10.1126/science.1113729. URL <http://science.sciencemag.org/content/309/5738/1219>.
- [73] Donald J. Douglas, Aaron J. Frank, and Dunmin Mao. Linear ion traps in mass spectrometry. *Mass Spectrometry Reviews*, 24(1):1–29, 2005. ISSN 1098-2787. doi: 10.1002/mas.20004. URL <http://dx.doi.org/10.1002/mas.20004>.
- [74] Klaus Blaum. High-accuracy mass spectrometry with stored ions. *Physics Reports*, 425(1):1 – 78, 2006. ISSN 0370-1573. doi: <http://dx.doi.org/10.1016/j.physrep.2005.10.011>. URL <http://www.sciencedirect.com/science/article/pii/S0370157305004643>.
- [75] D. Leibfried, R. Blatt, C. Monroe, and D. Wineland. Quantum dynamics of single trapped ions. *Rev. Mod. Phys.*, 75:281–324, Mar 2003. doi: 10.1103/RevModPhys.75.281. URL <http://link.aps.org/doi/10.1103/RevModPhys.75.281>.
- [76] Jochen Mikosch, Matthias Weidemüller, and Roland Wester. On the dynamics of chemical reactions of negative ions. *International Reviews in Physical Chemistry*, 29(4):589–617, 2010. doi: 10.1080/0144235X.2010.519504. URL <http://dx.doi.org/10.1080/0144235X.2010.519504>.
- [77] D. Gerlich and G. Kaefer. Ion trap studies of association processes in collisions of ch_3^+ and cd_3^+ with $n-h_2$, $p-h_2$, d_2 , and he at 80 k. *Astrophys. J.*, 347:849–854, 1989. doi: 10.1086/168174.
- [78] D Gerlich and M Smith. Laboratory astrochemistry: studying molecules under inter- and circumstellar conditions. *Physica Scripta*, 73(1):C25, 2006. URL <http://stacks.iop.org/1402-4896/73/i=1/a=N05>.

- [79] Oskar Asvany and Stephan Schlemmer. Numerical simulations of kinetic ion temperature in a cryogenic linear multipole trap. *International Journal of Mass Spectrometry*, 279:147 – 155, 2009. ISSN 1387-3806. doi: <http://dx.doi.org/10.1016/j.ijms.2008.10.022>. URL <http://www.sciencedirect.com/science/article/pii/S1387380608004338>.
- [80] Ralph G. DeVoe. Power-law distributions for a trapped ion interacting with a classical buffer gas. *Phys. Rev. Lett.*, 102:063001, Feb 2009. doi: 10.1103/PhysRevLett.102.063001. URL <http://link.aps.org/doi/10.1103/PhysRevLett.102.063001>.
- [81] Christoph Zipkes, Lothar Ratschbacher, Carlo Sias, and Michael Köhl. Kinetics of a single trapped ion in an ultracold buffer gas. *New Journal of Physics*, 13(5):053020, 2011. URL <http://stacks.iop.org/1367-2630/13/i=5/a=053020>.
- [82] Marko Cetina, Andrew T. Grier, and Vladan Vuletić. Micromotion-induced limit to atom-ion sympathetic cooling in paul traps. *Phys. Rev. Lett.*, 109:253201, Dec 2012. doi: 10.1103/PhysRevLett.109.253201. URL <http://link.aps.org/doi/10.1103/PhysRevLett.109.253201>.
- [83] Kuang Chen, Scott T. Sullivan, and Eric R. Hudson. Neutral gas sympathetic cooling of an ion in a paul trap. *Phys. Rev. Lett.*, 112:143009, Apr 2014. doi: 10.1103/PhysRevLett.112.143009. URL <http://link.aps.org/doi/10.1103/PhysRevLett.112.143009>.
- [84] Oskar Asvany, Oliver Ricken, Holger S. P. Müller, Martina C. Wiedner, Thomas F. Giesen, and Stephan Schlemmer. High-resolution rotational spectroscopy in a cold ion trap: h_2d^+ and d_2h^+ . *Phys. Rev. Lett.*, 100:233004, Jun 2008. doi: 10.1103/PhysRevLett.100.233004. URL <http://link.aps.org/doi/10.1103/PhysRevLett.100.233004>.
- [85] Stefan Schmid, Arne Härter, and Johannes Hecker Denschlag. Dynamics of a cold trapped ion in a bose-einstein condensate. *Phys. Rev. Lett.*, 105:133202, Sep 2010. doi: 10.1103/PhysRevLett.105.133202. URL <http://link.aps.org/doi/10.1103/PhysRevLett.105.133202>.
- [86] R. Otto, J. Xie, J. Brox, S. Trippel, M. Stei, T. Best, M. R. Siebert, W. L. Hase, and R. Wester. Reaction dynamics of temperature-variable anion water clusters studied with crossed beams and by direct dynamics. *Faraday Discuss.*, 157:41–57, 2012. doi: 10.1039/C2FD20013A. URL <http://dx.doi.org/10.1039/C2FD20013A>.

- [87] D. Gerlich. *Inhomogeneous rf fields: a versatile tool for the study of processes with slow ions*, volume LXXXI of *Advances in Chemical Physics*, chapter 1. John Wiley & Sons, Inc., 1992.
- [88] Roland Wester. Radiofrequency multipole traps: tools for spectroscopy and dynamics of cold molecular ions. *Journal of Physics B: Atomic, Molecular and Optical Physics*, 42(15):154001, 2009. URL <http://arxiv.org/abs/0902.0475>.
- [89] M H Friedman, A L Yergey, and J E Campana. Fundamentals of ion motion in electric radio-frequency multipole fields. *Journal of Physics E: Scientific Instruments*, 15(1):53, 1982. URL <http://stacks.iop.org/0022-3735/15/i=1/a=010>.
- [90] Norman W McLachlan. *Theory and application of mathieu functions*. 1951.
- [91] Josef Meixner and Friedrich Wilhelm Schäfke. *Mathieusche Funktionen und Sphäroidfunktionen: mit Anwendungen auf physikalische und technische Probleme*, volume 71. Springer-Verlag, 2013.
- [92] E. Teloy and D. Gerlich. Integral cross sections for ion-molecule reactions. i. the guided beam technique. *Chemical Physics*, 4(3): 417 – 427, 1974. ISSN 0301-0104. doi: [http://dx.doi.org/10.1016/0301-0104\(74\)85008-1](http://dx.doi.org/10.1016/0301-0104(74)85008-1). URL <http://www.sciencedirect.com/science/article/pii/0301010474850081>.
- [93] R. Côté and A. Dalgarno. Ultracold atom-ion collisions. *Phys. Rev. A*, 62:012709, Jun 2000. doi: [10.1103/PhysRevA.62.012709](https://doi.org/10.1103/PhysRevA.62.012709). URL <http://link.aps.org/doi/10.1103/PhysRevA.62.012709>.
- [94] Langevin. *Annales de chimie et de physique. Ann. Chim. Phys*, 5:245, 1905.
- [95] George Gioumouisis and D. P. Stevenson. Reactions of gaseous molecule ions with gaseous molecules. v. theory. *The Journal of Chemical Physics*, 29(2):294–299, 1958. doi: <http://dx.doi.org/10.1063/1.1744477>. URL <http://scitation.aip.org/content/aip/journal/jcp/29/2/10.1063/1.1744477>.
- [96] Hidetsugu Sakaguchi. Fluctuation dissipation relation for a langevin model with multiplicative noise. *Journal of the Physical Society of Japan*, 70(11):3247–3250, 2001.
- [97] Claudio Juan Tessone, Massimo Cencini, and Alessandro Torcini. Synchronization of extended chaotic systems with long-range interactions: An analogy to lévy-flight spreading of epidemics. *Phys. Rev. Lett.*, 97:224101, Nov 2006. doi: [10.1103/PhysRevLett.97.224101](https://doi.org/10.1103/PhysRevLett.97.224101). URL <http://link.aps.org/doi/10.1103/PhysRevLett.97.224101>.

- [98] Ziv Meir, Tomas Sikorsky, Ruti Ben-shlomi, Nitzan Akerman, Yehonatan Dallal, and Roei Ozeri. Dynamics of a ground-state cooled ion colliding with ultra-cold atoms. *ArXiv e-prints*, 2016. URL <https://arxiv.org/abs/1603.01810>.
- [99] Julian Glässel. Saturation absorption imaging of a high-density rubidium dark spot. *Master thesis, Ruprecht Karls Universität Heidelberg*, 2014.
- [100] Stefan F. Paul. Optimization of the ion storage in a hybrid atom-ion-trap. *Master thesis, Ruprecht Karls Universität Heidelberg*, 2015.
- [101] J. Deiglmayr, A. Göritz, T. Best, M. Weidemüller, and R. Wester. Reactive collisions of trapped anions with ultracold atoms. *Phys. Rev. A*, 86:043438, Oct 2012. doi: 10.1103/PhysRevA.86.043438. URL <http://link.aps.org/doi/10.1103/PhysRevA.86.043438>.
- [102] Anna T. Göritz. Wechselwirkung zwischen Ionen und kalten Atomen. Master's thesis, Albert Ludwigs Universität Freiburg, 2011.
- [103] Simone Götz. *A high density target of ultracold atoms and momentum resolved measurements of ion-atom collisions*. PhD thesis, Universität Heidelberg, 2012.
- [104] Bernhard Wolf. *Handbook of ion sources*. CRC press, 1995.
- [105] Ian G Brown. *The physics and technology of ion sources*. John Wiley & Sons, 2004.
- [106] M. Bacal. Physics aspects of negative ion sources. *Nuclear Fusion*, 46(6):p.250, 2006. URL <http://stacks.iop.org/0029-5515/46/i=6/a=S05>.
- [107] David L. Osborn, David J. Leahy, Douglas R. Cyr, and Daniel M. Neumark. Photodissociation spectroscopy and dynamics of the $N_2O_2^-$ anion. *The Journal of Chemical Physics*, 104(13): 5026–5039, 1995. doi: <http://dx.doi.org/10.1063/1.471132>. URL <http://scitation.aip.org/content/aip/journal/jcp/104/13/10.1063/1.471132>.
- [108] Michael D. Morse. Supersonic beam sources. In F.B. Dunning and Randall G. Hulet, editors, *Atomic, Molecular, and Optical Physics: Atoms and Molecules*, volume 29, Part B of *Experimental Methods in the Physical Sciences*, pages 21 – 47. Academic Press, 1996. doi: [http://dx.doi.org/10.1016/S0076-695X\(08\)60784-X](http://dx.doi.org/10.1016/S0076-695X(08)60784-X). URL <http://www.sciencedirect.com/science/article/pii/S0076695X0860784X>.

- [109] A.B. El-Kareh and J.C.J. El-Kareh. Chapter iv - general properties of electrostatic lenses. In *Electron Beams, Lenses, and Optics*, pages 54 – 80. Academic Press, 1970. ISBN 978-0-12-238001-3. doi: <http://dx.doi.org/10.1016/B978-0-12-238001-3.50008-5>. URL <http://www.sciencedirect.com/science/article/pii/B9780122380013500085>.
- [110] WC Wiley and Li H McLaren. Time-of-flight mass spectrometer with improved resolution. *Review of Scientific Instruments*, 26(12): 1150–1157, 1955.
- [111] Ronald M. Jones, Dieter Gerlich, and Scott L. Anderson. Simple radio-frequency power source for ion guides and ion traps. *Review of Scientific Instruments*, 68(9):3357–3362, 1997. doi: <http://dx.doi.org/10.1063/1.1148297>. URL <http://scitation.aip.org/content/aip/journal/rsi/68/9/10.1063/1.1148297>.
- [112] Ronald M. Jones and Scott L. Anderson. Simplified radio-frequency generator for driving ion guides, traps, and other capacitive loads. *Review of Scientific Instruments*, 71(11): 4335–4337, 2000. doi: <http://dx.doi.org/10.1063/1.1318914>. URL <http://scitation.aip.org/content/aip/journal/rsi/71/11/10.1063/1.1318914>.
- [113] George V Buxton, Clive L Greenstock, W Phillips Helman, and Alberta B Ross. Critical review of rate constants for reactions of hydrated electrons, hydrogen atoms and hydroxyl radicals oh/o- in aqueous solution. *Journal of physical and chemical reference data*, 17(2):513–886, 1988.
- [114] AW Castleman Jr and RG Keesee. Ionic clusters. *Chemical Reviews*, 86(3):589–618, 1986.
- [115] Stephen J Smith and Lewis M Branscomb. Atomic negative-ion-photodetachment cross-section and affinity measurements. *Journal of Research of the National Bureau of Standards*, 55(3), 1955.
- [116] Harold J Metcalf and Peter Straten. *Laser cooling and trapping of neutral atoms*. Wiley Online Library, 2007.
- [117] G. C. Bjorklund, M. D. Levenson, W. Lenth, and C. Ortiz. Frequency modulation (fm) spectroscopy. *Applied Physics B*, 32(3): 145–152, 1983. ISSN 1432-0649. doi: 10.1007/BF00688820. URL <http://dx.doi.org/10.1007/BF00688820>.
- [118] EA Donley, TP Heavner, F Levi, MO Tataw, and SR Jefferts. Double-pass acousto-optic modulator system. *Review of Scientific Instruments*, 76(6):063112, 2005.

- [119] KMF Magalhaes, SR Muniz, GD Telles, P.W. Courteille, VS Bagnato, and LG Marcassa. The Escape Velocity in a Magneto-Optical Trap and Its Importance to Trap Loss Investigation. *Laser Physics*, 12(1):145–151, 2002.
- [120] Bastian Höltkemeier. 2d mot as a source of a cold atom target. *Diploma thesis, Ruprecht Karls Universität Heidelberg*, 2011.
- [121] J. Schoser, A. Batär, R. Löw, V. Schweikhard, A. Grabowski, Y.B. Ovchinnikov, and T. Pfau. Intense source of cold Rb atoms from a pure two-dimensional magneto-optical trap. *Physical Review A*, 66(2):23410, 2002. ISSN 1094-1622.
- [122] J. Ramirez-Serrano, N. Yu, J.M. Kohel, J.R. Kellogg, and L. Maleki. Multistage two-dimensional magneto-optical trap as a compact cold atom beam source. *Optics letters*, 31(6):682–684, 2006. ISSN 1539-4794.
- [123] K. Dieckmann, RJC Spreeuw, M. Weidemüller, and JTM Walraven. Two-dimensional magneto-optical trap as a source of slow atoms. *Physical Review A*, 58(5):3891–3895, 1998. ISSN 1094-1622.
- [124] J. Catani, P. Maioli, L. De Sarlo, F. Minardi, and M. Inguscio. Intense slow beams of bosonic potassium isotopes. *Phys. Rev. A*, 73(3):033415, Mar 2006. doi: 10.1103/PhysRevA.73.033415.
- [125] S. Weyers, E. Aucouturier, C. Valentin, and N. Dimarcq. A continuous beam of cold cesium atoms extracted from a two-dimensional magneto-optical trap. *Optics Communications*, 143(1-3):30–34, 1997. ISSN 0030-4018.
- [126] P. Berthoud, A. Joyet, G. Duddle, N. Sagna, and P. Thomann. A continuous beam of slow, cold cesium atoms magnetically extracted from a 2D magneto-optical trap. *EPL (Europhysics Letters)*, 41:141, 1998.
- [127] T. G. Tiecke, S. D. Gensemer, A. Ludewig, and J. T. M. Walraven. High-flux two-dimensional magneto-optical-trap source for cold lithium atoms. *Phys. Rev. A*, 80(1):013409, Jul 2009. doi: 10.1103/PhysRevA.80.013409.
- [128] Wolfgang Ketterle, Kendall B. Davis, Michael A. Joffe, Alex Martin, and David E. Pritchard. High densities of cold atoms in a dark spontaneous-force optical trap. *Phys. Rev. Lett.*, 70:2253–2256, Apr 1993. doi: 10.1103/PhysRevLett.70.2253. URL <http://link.aps.org/doi/10.1103/PhysRevLett.70.2253>.
- [129] David W Sesko, TG Walker, and Carl E Wieman. Behavior of neutral atoms in a spontaneous force trap. *JOSA B*, 8(5):946–958, 1991.

- [130] C. G. Townsend, N. H. Edwards, C. J. Cooper, K. P. Zetie, C. J. Foot, A. M. Steane, P. Szriftgiser, H. Perrin, and J. Dalibard. Phase-space density in the magneto-optical trap. *Phys. Rev. A*, 52:1423–1440, Aug 1995. doi: 10.1103/PhysRevA.52.1423. URL <http://link.aps.org/doi/10.1103/PhysRevA.52.1423>.
- [131] Rodney Loudon. *The quantum theory of light*. OUP Oxford, 2000.
- [132] G. Reinaudi, T. Lahaye, Z. Wang, and D. Guéry-Odelin. Strong saturation absorption imaging of dense clouds of ultracold atoms. *Opt. Lett.*, 32(21):3143–3145, Nov 2007. doi: 10.1364/OL.32.003143. URL <http://ol.osa.org/abstract.cfm?URI=ol-32-21-3143>.
- [133] WooJin Kwon, Jae-yoon Choi, and Yong-il Shin. Calibration of saturation absorption imaging of ultracold atom clouds. *Journal of the Korean Physical Society*, 61(12):1970–1974, December 2012. ISSN 0374-4884. doi: 10.3938/jkps.61.1970. URL <http://dx.doi.org/10.3938/jkps.61.1970>.
- [134] Ji Luo. Rotational temperature of ions via photodetachment. *Master thesis, Karlsruhe Institute of Technology*, 2016.
- [135] RR Corderman and WC Lineberger. Negative ion spectroscopy. *Annual Review of Physical Chemistry*, 30(1):347–378, 1979.
- [136] P. Hlavenka, R. Otto, S. Trippel, J. Mikosch, M. Weidemüller, and R. Wester. Absolute photodetachment cross section measurements of the o^- and oh^- anion. *The Journal of Chemical Physics*, 130(6):061105, 2009. doi: <http://dx.doi.org/10.1063/1.3080809>. URL <http://scitation.aip.org/content/aip/journal/jcp/130/6/10.1063/1.3080809>.
- [137] R Otto, P Hlavenka, S Trippel, J Mikosch, K Singer, M Weidemüller, and R Wester. How can a 22-pole ion trap exhibit ten local minima in the effective potential? *Journal of Physics B: Atomic, Molecular and Optical Physics*, 42(15):154007, 2009. URL <http://stacks.iop.org/0953-4075/42/i=15/a=154007>.
- [138] T. Best, R. Otto, S. Trippel, P. Hlavenka, A. von Zastrow, S. Eisenbach, S. Jezouin, R. Wester, E. Vigrén, M. Hamberg, and W. D. Geppert. Absolute photodetachment cross-section measurements for hydrocarbon chain anions. *The Astrophysical Journal*, 742(2):63, 2011. URL <http://stacks.iop.org/0004-637X/742/i=2/a=63>.
- [139] Friedrich Hund. Allgemeine quantenmechanik des atom-und molekelbaues. In *Quantentheorie (Handbuch der Physik)*, pages 561–694. Springer, 1933.

- [140] John M Brown and Alan Carrington. *Rotational spectroscopy of diatomic molecules*. Cambridge University Press, 2003.
- [141] E.E. Nikitin and R.N. Zare. Correlation diagrams for hund's coupling cases in diatomic molecules with high rotational angular momentum. *Molecular Physics*, 82(1):85–100, 1994. doi: 10.1080/00268979400100074. URL <http://dx.doi.org/10.1080/00268979400100074>.
- [142] Alan Carrington, Christine A Leach, Andrew J Marr, Andrew M Shaw, Mark R Viant, Jeremy M Hutson, and Mark M Law. Microwave spectroscopy and interaction potential of the long-range he... ar+ ion. *The Journal of chemical physics*, 102(6):2379–2403, 1995.
- [143] Robert S Mulliken. Iodine revisited. *The Journal of Chemical Physics*, 55(1):288–309, 1971.
- [144] Jinchun Xie and Richard N. Zare. Selection rules for the photoionization of diatomic molecules. *The Journal of Chemical Physics*, 93(5):3033–3038, 1990. doi: <http://dx.doi.org/10.1063/1.458837>. URL <http://scitation.aip.org/content/aip/journal/jcp/93/5/10.1063/1.458837>.
- [145] I Dabrowski, DW Tokaryk, RH Lipson, and JKG Watson. New rydberg–rydberg transitions of the arh and ard molecules: Iii. emission from the 4fcomplexes. *Journal of molecular spectroscopy*, 189(1):110–123, 1998.
- [146] Alan Carrington, Christopher H. Pyne, Andrew M. Shaw, Susie M. Taylor, Jeremy M. Hutson, and Mark M. Law. Microwave spectroscopy and interaction potential of the long-range he—kr+ ion: An example of hund's case (e). *The Journal of Chemical Physics*, 105(19):8602–8614, 1996. doi: <http://dx.doi.org/10.1063/1.472999>. URL <http://scitation.aip.org/content/aip/journal/jcp/105/19/10.1063/1.472999>.
- [147] H Lefebvre-Brion. Hund's case (e): Application to rydberg states with a 2π ionic core. *The Journal of Chemical Physics*, 93(8):5898–5901, 1990.
- [148] Philip M Morse. Diatomic molecules according to the wave mechanics. ii. vibrational levels. *Physical Review*, 34(1):57, 1929.
- [149] H. Hotop, T. A. Patterson, and W. C. Lineberger. High resolution photodetachment study of oh- and od- in the threshold region 7000–6450 Å. *The Journal of Chemical Physics*, 60(5):1806–1812, 1974. doi: <http://dx.doi.org/10.1063/1.1681279>. URL <http://scitation.aip.org/content/aip/journal/jcp/60/5/10.1063/1.1681279>.

- [150] Gerhard Herzberg. Molecular spectra and molecular structure. vol. 1: Spectra of diatomic molecules. *New York: Van Nostrand Reinhold, 1950, 2nd ed., 1, 1950.*
- [151] Fabienne Goldfarb, Cyril Drag, Walid Chaibi, Sophie Krüger, Christophe Blondel, and Christian Delsart. Photodetachment microscopy of the p, q, and r branches of the oh(-)(v=0) to oh(v=0) detachment threshold. *The Journal of chemical physics*, 122(1):14308, January 2005. ISSN 0021-9606. doi: 10.1063/1.1824904. URL <http://dx.doi.org/10.1063/1.1824904>.
- [152] PA Schulz, Roy D Mead, PL Jones, and WC Lineberger. Oh- and od- threshold photodetachment. *The Journal of Chemical Physics*, 77(3):1153–1165, 1982.
- [153] Neil H. Rosenbaum, Jeffrey C. Owrutsky, Leslie M. Tack, and Richard J. Saykally. Velocity modulation laser spectroscopy of negative ions: The infrared spectrum of hydroxide (oh-). *The Journal of Chemical Physics*, 84(10):5308–5313, 1986. doi: <http://dx.doi.org/10.1063/1.449941>. URL <http://scitation.aip.org/content/aip/journal/jcp/84/10/10.1063/1.449941>.
- [154] Jim R. Smith, Joseph B. Kim, and W. C. Lineberger. High-resolution threshold photodetachment spectroscopy of oh⁻. *Phys. Rev. A*, 55:2036–2043, Mar 1997. doi: 10.1103/PhysRevA.55.2036. URL <http://link.aps.org/doi/10.1103/PhysRevA.55.2036>.
- [155] F. Breyer, P. Frey, and H. Hotop. High resolution photoelectron spectrometry of negative ions: Rotational transitions in laser-photodetachment of oh-, sh-, sd-. *Zeitschrift für Physik A Atoms and Nuclei*, 300(1):7–24, 1981. ISSN 0939-7922. doi: 10.1007/BF01412609. URL <http://dx.doi.org/10.1007/BF01412609>.
- [156] Lewis M. Branscomb. Photodetachment cross section, electron affinity, and structure of the negative hydroxyl ion. *Phys. Rev.*, 148:11–18, Aug 1966. doi: 10.1103/PhysRev.148.11. URL <http://link.aps.org/doi/10.1103/PhysRev.148.11>.
- [157] Robert A. Beaudet and Robert L. Poynter. Microwave spectra of molecules of astrophysical interest xii. hydroxyl radical. *Journal of Physical and Chemical Reference Data*, 7(1):311–362, 1978. doi: <http://dx.doi.org/10.1063/1.555570>. URL <http://scitation.aip.org/content/aip/journal/jpcrd/7/1/10.1063/1.555570>.
- [158] J. A. Coxon. Optimum molecular constants and term values for the x 2π (v ≤ 5) and a 2σ+(v ≤ 3) states of oh. *Canadian Journal of Physics*, 58(7):933–949, 1980. doi: 10.1139/p80-129. URL <http://dx.doi.org/10.1139/p80-129>.

- [159] Pavel Rosmus and Wilfried Meyer. Pno-ci and cepa studies of electron correlation effects. vi. electron affinities of the first-row and second-row diatomic hydrides and the spectroscopic constants of their negative ions. *The Journal of Chemical Physics*, 69(6):2745–2751, 1978. doi: <http://dx.doi.org/10.1063/1.436871>. URL <http://scitation.aip.org/content/aip/journal/jcp/69/6/10.1063/1.436871>.
- [160] E. Hill and J. H. Van Vleck. On the quantum mechanics of the rotational distortion of multiplets in molecular spectra. *Phys. Rev.*, 32:250–272, Aug 1928. doi: 10.1103/PhysRev.32.250. URL <http://link.aps.org/doi/10.1103/PhysRev.32.250>.
- [161] J. H. Van Vleck. On σ -type doubling and electron spin in the spectra of diatomic molecules. *Phys. Rev.*, 33:467–506, Apr 1929. doi: 10.1103/PhysRev.33.467. URL <http://link.aps.org/doi/10.1103/PhysRev.33.467>.
- [162] Robert S Mulliken and Andrew Christy. λ -type doubling and electron configurations in diatomic molecules. *Physical Review*, 38(1):87, 1931.
- [163] J.A. Coxon and S.C. Foster. Radial dependence of spin-orbit and λ -doubling parameters in the $x\ 2\ \pi$ ground state of hydroxyl. *Journal of Molecular Spectroscopy*, 91(1):243 – 254, 1982. ISSN 0022-2852. doi: [http://dx.doi.org/10.1016/0022-2852\(82\)90043-1](http://dx.doi.org/10.1016/0022-2852(82)90043-1). URL <http://www.sciencedirect.com/science/article/pii/0022285282900431>.
- [164] R. J. Celotta, R. A. Bennett, and J. L. Hall. Laser photodetachment determination of the electron affinities of oh, nh₂, nh, so₂, and s₂. *The Journal of Chemical Physics*, 60(5):1740–1745, 1974. doi: <http://dx.doi.org/10.1063/1.1681268>. URL <http://scitation.aip.org/content/aip/journal/jcp/60/5/10.1063/1.1681268>.
- [165] Laurence S Rothman, Iouli E Gordon, Alain Barbe, D Chris Benner, Peter F Bernath, Manfred Birk, Vincent Boudon, Linda R Brown, Alain Campargue, J-P Champion, et al. The {HITRAN} 2008 molecular spectroscopic database. *Journal of Quantitative Spectroscopy and Radiative Transfer*, 110(9):533 – 572, 2009. ISSN 0022-4073. doi: <http://dx.doi.org/10.1016/j.jqsrt.2009.02.013>. URL <http://www.sciencedirect.com/science/article/pii/S0022407309000727>. {HITRAN}.
- [166] Christian Hill, Iouli E. Gordon, Roman V. Kochanov, Lorenzo Barrett, Jonas S. Wilzewski, and Laurence S. Rothman. Hitranonline: An online interface and the flexible representation of spectroscopic data in the {HITRAN} database. *Journal of Quantitative Spectroscopy and Radiative Transfer*, 177:4 – 14, 2016.

- ISSN 0022-4073. doi: <http://dx.doi.org/10.1016/j.jqsrt.2015.12.012>. URL <http://www.sciencedirect.com/science/article/pii/S0022407315302375>. {XVIIIth} Symposium on High Resolution Molecular Spectroscopy (HighRus-2015), Tomsk, Russia.
- [167] G. C. Dousmanis, T. M. Sanders, and C. H. Townes. Microwave spectra of the free radicals oh and od. *Phys. Rev.*, 100:1735–1754, Dec 1955. doi: 10.1103/PhysRev.100.1735. URL <http://link.aps.org/doi/10.1103/PhysRev.100.1735>.
- [168] A. R. P. Rau and U. Fano. Theory of photodetachment near fine-structure thresholds. *Phys. Rev. A*, 4:1751–1759, Nov 1971. doi: 10.1103/PhysRevA.4.1751. URL <http://link.aps.org/doi/10.1103/PhysRevA.4.1751>.
- [169] W. C. Lineberger and Benjamin W. Woodward. High resolution photodetachment of s^- near threshold. *Phys. Rev. Lett.*, 25:424–427, Aug 1970. doi: 10.1103/PhysRevLett.25.424. URL <http://link.aps.org/doi/10.1103/PhysRevLett.25.424>.
- [170] Bruce K. Janousek and John I. Brauman. Electron photodetachment from hs^- . the electron affinity of hs . *Phys. Rev. A*, 23:1673–1678, Apr 1981. doi: 10.1103/PhysRevA.23.1673. URL <http://link.aps.org/doi/10.1103/PhysRevA.23.1673>.
- [171] J D Rudmin, L P Ratliff, J N Yukich, and D J Larson. Structure of the photodetachment cross section in a magnetic field: an experiment with oh-. *Journal of Physics B: Atomic, Molecular and Optical Physics*, 29(24):L881, 1996. URL <http://stacks.iop.org/0953-4075/29/i=24/a=004>.
- [172] T. E. H. Walker, P. M. Dehmer, and J. Berkowitz. Rotational band shapes in photoelectron spectroscopy: Hf and df. *The Journal of Chemical Physics*, 59(8):4292–4298, 1973. doi: <http://dx.doi.org/10.1063/1.1680624>. URL <http://scitation.aip.org/content/aip/journal/jcp/59/8/10.1063/1.1680624>.
- [173] P. A. Schulz, Roy D. Mead, and W. C. Lineberger. Rotational intensities in photodetachment and photoionization. *Phys. Rev. A*, 27:2229–2232, Apr 1983. doi: 10.1103/PhysRevA.27.2229. URL <http://link.aps.org/doi/10.1103/PhysRevA.27.2229>.
- [174] Eugene P. Wigner. On the behavior of cross sections near thresholds. *Phys. Rev.*, 73:1002–1009, May 1948. doi: 10.1103/PhysRev.73.1002. URL <http://link.aps.org/doi/10.1103/PhysRev.73.1002>.
- [175] Thomas F O'Malley. Effect of long-range final-state forces on the negative-ion photodetachment cross section near threshold. *Physical Review*, 137(6A):A1668, 1965.

- [176] Paul C. Engelking. Strong electron-dipole coupling in photodetachment of molecular negative ions: Anomalous rotational thresholds. *Phys. Rev. A*, 26:740–745, Aug 1982. doi: 10.1103/PhysRevA.26.740. URL <http://link.aps.org/doi/10.1103/PhysRevA.26.740>.
- [177] Bruce K Janousek, Albert H Zimmerman, Kenneth J Reed, and John I Brauman. Electron photodetachment from aliphatic molecular anions. gas-phase electron affinities of methoxyl, tert-butoxyl, and neopentoxyl radicals. *Journal of the American Chemical Society*, 100(19):6142–6148, 1978.
- [178] Bruce Steiner. Photodetachment of electrons from sh-. *The Journal of Chemical Physics*, 49(11):5097–5104, 1968. doi: <http://dx.doi.org/10.1063/1.1670004>. URL <http://scitation.aip.org/content/aip/journal/jcp/49/11/10.1063/1.1670004>.
- [179] Rico Otto. *Dynamics of a Microsolvated Ion-Molecule Reaction*. PhD thesis, Albert-Ludwigs-Universität Freiburg, 2011.
- [180] Rico Otto, Alexander von Zastrow, Thorsten Best, and Roland Wester. Internal state thermometry of cold trapped molecular anions. *Physical Chemistry Chemical Physics*, 15(2):612–618, 2013.
- [181] TF Johnston Jr. Tunable dye lasers, encyclopedia of physical science and technology. *Academic, New York*, 14:96–141, 1987.
- [182] Jason N. Byrd, H. Harvey Michels, John A. Montgomery, and Robin Côté. Associative detachment of rubidium hydroxide. *Phys. Rev. A*, 88:032710, Sep 2013. doi: 10.1103/PhysRevA.88.032710. URL <http://link.aps.org/doi/10.1103/PhysRevA.88.032710>.
- [183] Milaim Kas, Jerome Loreau, Jacques Lievin, and Nathalie Vaeck. Ab initio study of reactive collisions between rb(2s) or rb(2p) and oh⁻(¹σ⁺). *The Journal of Chemical Physics*, 144(20):204306, 2016. doi: <http://dx.doi.org/10.1063/1.4950784>. URL <http://scitation.aip.org/content/aip/journal/jcp/144/20/10.1063/1.4950784>.
- [184] Florian Weigend and Alexander Baldes. Segmented contracted basis sets for one- and two-component dirac-fock effective core potentials. *The Journal of Chemical Physics*, 133(17):174102, 2010. doi: <http://dx.doi.org/10.1063/1.3495681>. URL <http://scitation.aip.org/content/aip/journal/jcp/133/17/10.1063/1.3495681>.
- [185] Felix H.J. Hall, Pascal Eberle, Gregor Hegi, Maurice Raoult, Mireille Aymar, Olivier Dulieu, and Stefan Willitsch. Ion-neutral chemistry at ultralow energies: dynamics of reactive collisions

- between laser-cooled Ca^+ ions and Rb atoms in an ion-atom hybrid trap. *Molecular Physics*, 0(0):1–13, 2012. doi: 10.1080/00268976.2013.780107. URL <http://www.tandfonline.com/doi/abs/10.1080/00268976.2013.780107>.
- [186] L. Gonzalez-Sanchez, M. Tacconi, E. Bodo, and F.A. Gianturco. Ionic interactions and collision dynamics in cold traps: rotational quenching of $\text{OH}^- (^1\sigma^+)$ by Rb(2s). *The European Physical Journal D*, 49(1):85–92, 2008. ISSN 1434-6060. doi: 10.1140/epjd/e2008-00148-5. URL <http://dx.doi.org/10.1140/epjd/e2008-00148-5>.
- [187] M. Tacconi and F. A. Gianturco. Translational cooling versus vibrational quenching in ultracold OH^- -Rb collisions: A quantum assessment. *The Journal of Chemical Physics*, 131(9):094301, 2009. doi: 10.1063/1.3192101. URL <http://link.aip.org/link/?JCP/131/094301/1>.

ACKNOWLEDGEMENTS

Zuallererst möchte ich natürlich *Matthias* danken. Ich habe vor ca. 6 Jahren meine Diplomarbeit bei dir angefangen nachdem ihr gerade aus Freiburg in Heidelberg angekommen wart. Die Zeit hat mir unglaublich viel Spaß gemacht und ich hoffe wir werden auch über die kommenden Jahre Kontakt halten! Ich hatte das Gefühl dass ich mich unter deiner Aufsicht frei entfalten konnte und ich habe das sehr genossen. Vielen Dank für Alles!

Natürlich möchte ich mich auch bei meinem Zweitkorrektor *Klaus Blaum* bedanken. Ich bin mir nicht sicher ob du dich noch erinnerst, aber vor ein paar Jahren habe ich dich in Stuttgart überzeugt in die falsche U-Bahn einzusteigen. Wir sind dann zusammen ca. 20min eine große Runde im Kreis gefahren, bis wir wieder am Hauptbahnhof waren. Danach hast du dann doch lieber dem Ausdruck deiner Sekretärin vertraut... Trotzdem hast du dich jetzt bereit erklärt diese Arbeit zu bewerten und ich hoffe es wird nicht allzu langweilig. Vielen Dank dafür!

Fünf guten Appetiten gehen an *Henry*!

Ich kann dir gar nicht sagen wie froh ich bin, dass du dich damals für unsere Gruppe entschieden hast! Die letzten Jahre waren eine absolute Freude ich habe viel mehr als einen Arbeitskollegen kennengelernt. Hemingway hat einmal gesagt "Wahre Freundschaften findet man nur auf der Arbeit" und ich glaube er hätte nicht richtiger liegen können. Natürlich hat er das nicht gesagt, aber ich glaube dennoch dass er völlig Recht hatte! Ich kann nur sagen, dass ich in den letzten Jahren einen wahren Freund in dir gefunden habe. Auch wenn ich natürlich nie mit Pablo mithalten kann... Noch einen letzten Rat: Clebsch?Gordan ist ein super Name für einen Jungen... Falls es doch noch ein Mädchen wird gibt es sonst natürlich auch noch Bethe-Bloch... In diesem Sinne wünsche ich euch alles Gute, wenn ihr bald zu dritt seid und ich hoffe wir schaffen es auch bald mal zusammen in die Bananen-Republik!

Domenikel! Wir haben zusammen viel erlebt. Deine ruhige Art ist einfach super und ich hoffe wir werden noch lange Freunde bleiben! Viele Leute sind über die Jahre gekommen und gegangen und jetzt werden wir bald auch beide zu neuen Herausforderungen aufbrechen! Bleib einfach wie du bist, dann kann eigentlich nicht viel schief gehen! Nach meiner Verteidigung können wir dann ja auch gleich eure Hochzeit feiern... wenn das nicht mal ein Double-Feature ist! Dome, vielen Dank für Alles!

Ein ganz großer Dank geht natürlich auch an *Simone!* Es ist jetzt etwas her, aber ich erinnere mich immer noch mit Freude daran, wie wir vor Jahren jeden Tag am alten PI Tischtennis gespielt haben! Ich sage nur, dass Tischtennis mit Wall-shots einfach olympisch werden sollte... Falls das nicht klappt, dann wenigstens Squash... Ich habe immer noch Hoffnung, dass ich eines Tages mal einen Satz gegen dich gewinnen kann ohne dass du mir die Bälle zuspielst. Wenn das auch nicht klappt, dann müssen wir einfach weiter bei euch im Wohnzimmer auf dem Esstisch Tischtennis spielen... da habe ich dann wenigstens eine realistische Chance. Auch dir und Sherif wünsche ich einen guten Start ins Familienleben, wir kommen dann demnächst vorbei und richten schonmal unser Gästezimmer in Wiesloch ein! Irgendjemand muss dem kleinen Spätzle ja auch zweigen, dass es noch etwas außer Squash gibt!

Pascalito! Wir haben die Haifische besiegt, eine riesige Menge fluffy Chips im Büro verteilt, in Berlin die Kicker-Bar unsicher gemacht, in Amsterdam die Cof... Bars besucht und natürlich viel Spaß in der VIP-Lounge beim Seeeeeeeed Konzert gehabt. Wir konnten Stunden lang über theoretischen Konzepte diskutieren und am Ende haben wir es den Ionen echt gezeigt... zumindest theoretisch... :) Die Zeit mit dir hat mir unendlich viel Spaß gemacht und ich hoffe du wirst weiterhin genauso viel Spaß in Freiburg haben! Jetzt habe ich auch wieder Zeit und ich freue mich schon mit dir den Breisgau unsicher zu machen!

Don Julio! Es war eine geile Zeit! Ich sage nur Tresor und Cave... Die Zeit mit dir hat einfach Spaß gemacht... wo auf immer, ob im Labor beim Saturation Imaging oder in Berlin im Keller vom Kraftwerk, es war immer irgendwas los. Die Pans kommen übrigens mittlerweile nicht mehr in unser Labor gerannt, wenn jemand schreit... ich bin mir jetzt auch nicht ganz sicher ob das gut oder schlecht ist. Ich wünsche dir alles Gute in Dänemark und ich hoffe wir können bald mal ein kleines Reunion mit dem ganzen alten Team organisieren!

Damit sind wir dann auch schon bei *OctoPaul!* Deine Enthusiasmus, sei es bei den unendlichen SIMION Simulationen oder auf dem Auto vom Besitzer des Eckstein, war immer eine große Bereicherung. Shhhiiiiit irgendwie hast du mich immer an Jan Delay erinnert... ich wünsche dir eine großartige Zeit in Kanada! Ich hoffe wir sehen uns bald wieder und können vielleicht mal wieder zusammen mit Pascalito die Frauen in der Bar mit dem Baum unsicher machen! Vielen Dank für eine coole Zeit!

Anikikita. Du hast in deiner Zeit bei uns immer die Ruhe bewahrt, auch wenn der Laser mal wieder nicht so wollte, wie wir uns das vorgestellt hatten... Das Arbeiten mit dir hat immer großen Spaß gemacht und ich wünsche dir alles Gute!

Dann gabs da noch den *Eddi*. Dich hat man meistens mit Andre im Labor gefunden und ich hoffe dir hat die Zeit bei uns genauso viel Spaß wie mir gemacht! Dich konnte man einfach nie aus der Ruhe bringen auch wenn uns niemand vorwerfen kann, dass wir es nicht versucht haben!

Ji -sus -golo. Es war eine coole Zeit mit dir! Egal ob wir mit Lamas gewandert sind oder du uns in die Feinheiten der chinesischen Küche eingeweiht hast... bleib so wie du bist und ich wünsche dir alles Gute für deine neue Herausforderung in Paris/München/...

Dann war da natürlich noch unser südamerikanische Freund *Andre*. Da deine Deutschkenntnisse gegen Ende deines einjährigen Aufenthalts schon echt gut waren, verzichte ich an dieser Stelle auch auf einen Ausflug ins Englische. Die Zeit mit dir hat viel Spaß gemacht und ich hoffe das Lama-Diplom hängt jetzt auch in deinem Büro in Brasilien! Vielleicht sieht man sich ja bald mal wieder in Heidelberg, sonst muss ich einfach mal nach Brasilien kommen!

Damit sind wir jetzt schon beim Rest der QD-Gruppe angekommen... *Juris*, habt ihr schon euere Steusalz-Vorräte aufgestockt? Der Winter kommt schneller als man denkt... *Marc*, du solltest echt mal in Betracht ziehen einen Fahrradhelm aufzusetzen! *Rico*? thats what she said! Bei *Alda* geht das nur in Gesten... stell dir einfach eine Hand vor, die etwas in die andere hineinbröselst... Da ich hier nicht alle namentlich aufzählen kann, vielen Dank auch an den Rest der Rasselbande, die Zeit mit euch hat mir riesigen Spaß gemacht!

Ein ganz riesigen Dankeschön natürlich auch an die Werkstätten vom PI... ohne euch wäre das Ganze einfach nicht möglich geworden. Und da ging es nicht immer nur um technischen Support, bei dem Einen oder Anderen ging es weit über ein reines Arbeitsverhältnis hinaus! Ich kann nur sagen, dass ich selten eine so motivierte und fähige Gruppe Menschen auf einem Fleck erlebt habe... Vielen Dank für Alles!

Ein ganz großes Dankeschön geht natürlich auch nach Innsbruck, insbesondere an *Roland* und *Eric*! Die Kollaboration mit euch hat mir viel Freude bereitet und ich erinnere mich gerne an meine Besuche bei euch in Innsbruck, wie auch die Zeit, die wir zusammen in Heidelberg verbracht haben! *Eric*, das arbeiten mit dir an der HAITrap, wie auch diverse außeruniversitäre Aktivitäten waren eine extrem coole Zeit! Ich wünsche dir noch viel Glück beim fertigstellen deiner eigenen Arbeit und ich hoffe man sieht sich möglichst bald mal wieder!

Vielen Dank auch an die Leute mit denen ich die Freude hatte, in Heidelberg zu studieren. *Christoph*, *Christoph*, *Philipp*, *Philippe*, *Hannes*, *Hannes* und auch alle die es nur in einfacher Ausführung gibt... es war

eine tolle Zeit, die ich niemals vergessen werde. Ich hoffe wir werden lange Freunde bleiben, auch wenn es viele mittlerweile in die weite Welt zerstreut hat

Ein großer Dank auch an meine "Heidelberger Familie", *Lena* und *Vali*. Ich kann euch gar nicht sagen, wie sehr ich die gemeinsamen Jahre mit euch genossen habe! Irgendwann müssen wir dann halt doch alle wieder in die gleiche Stadt ziehen und eine neue WG aufmachen! *Vali* und *Philipp* haben ja eigentlich genug Platz...

Olga! Es war eine verrückte Reise und in dir habe ich eine super Partnerin gefunden! Du hast mir immer Rückhalt gegeben und hast es immer wieder geschafft mich anzustupsen und zu motivieren! Ich sage nur Ahoj Captain... dicker Kuss, ich liebe dich!

Dann sind wir auch schon bei meiner Familie angekommen, die mich immer und in allem voll unterstützt hat! *Oma*, vielen Dank für deine moralische wie natürlich auch finanzielle Unterstützung! Ich hoffe uns sind noch viele gemeinsame Jahre vergönnt und du bleibst so gesund und munter wie eh und je!

Zu guter Letzt möchte ich mich bei meinen Eltern bedanken! Da weiß ich jetzt einfach gar nicht wo ich anfangen soll... Von euch habe ich einfach immer riesige eine Unterstützung erhalten! Ich könnte mir einfach keine besseren Eltern vorstellen! Auch wenn ich vielleicht nicht bei Dr. Oetker arbeiten werde hoffe ich, dass wir noch lange zusammen Karten spielen, Fahrrad fahren, mit Klaus Gassi gehen, Tischtennis spielen, Kreuzworträtsel lösen und vieles mehr machen werden. Ohne euch wäre ich niemals der Mensch geworden, der ich heute bin! Vielen Dank!